University *of*
Leicester

Amplitudes of X-ray Variability in Accreting Black Holes

Lucy Maria Heil

Supervisor:

Simon Vaughan

A thesis submitted for the degree of
Doctor of Philosophy
at the University of Leicester

X-ray & Observational Astronomy Group
Department of Physics & Astronomy
University of Leicester

16th December 2010

Declaration

I hereby declare that no part of this thesis has been previously submitted to this or any other University as part of the requirement for a higher degree. The work described herein was conducted by the undersigned except for contrbutions from colleagues as acknowledged in the text.

Lucy Maria Heil

December 2010

Flux Dependent Variability from Black Holes

Lucy Maria Heil

ABSTRACT

The properties of X-ray variability from accreting black holes reveal much about conditions close to the event horizon. Observing common timing signals in many objects, suggests similarities within their accretion flows.

To further this aim this thesis presents a systematic survey of the short term variability properties in 19 observations of 16 Ultraluminous X-ray Sources (ULXs) taken with *XMM-Newton* using the power spectra. Significant short term variability is detected in 8 observations, but 4 of those remaining have upper limits on levels of variability below those observed in Galactic Black Hole Binaries (BHBs). Suggested causes for this suppression include large scale optically thick outflows destroying correlated variability from the source, or that the variability concentrated over shorter timescales than those studied here.

Tests for a positive linear correlation between the amplitude of variability (rms) and flux within an observation are presented for archival observations of 9 BHBs. Revealing that this relation is ubiquitous in the broad-band noise for all long, bright observations with sufficient variability to measure the rms. Interestingly, comparisons between the properties of the rms-flux relations over the course of many outbursts, reveal that the x-axis offsets become strongly positive as the source moves into the hard intermediate state.

The presence of a linear rms-flux correlation is also found in the light curve from a ULX (NGC 5408 X-1) and in some observations of the type C QPO from the 1998 outburst of XTE J1550-564. In the latter case the rms-flux relation is found to be dependent on the frequency of the QPO, becoming constant or even negative once the QPO moves above ~ 5 Hz. A possible time lag between soft and hard emission is also identified from the ULX.

Acknowledgements

Firstly a huge thank you goes to my supervisor Simon Vaughan, for all the help, guidance, patience and for always being willing to make time for me when I turn up at his office door. Thanks for being a fantastic supervisor, and ensuring that the research I've done over the last four years has been so interesting.

Thanks also goes to all of the friends I've had across the department who've been daft enough to go for a PhD too. From those who were here when I started and made me feel so welcome, to the newbies who've only just joined us, you've all been brilliant and made this whole experience so much fun. There are too many of you to name here, suffice to say that if you've made me laugh at some point in the past 3.5 years this is for you. I think that I owe a large measure of my sanity to the "interesting" conversations we've had at afternoon tea, so again - thanks for all being ever so slightly mad.

Specifically I have to thank the two people who began this journey with me, David and James. Dave, we've laughed, cried, moped and navigated the assorted evils of IDL together. At some points it seemed like we'd never get here but we finally did it, congratulations Dr. Baker! Dukey, your insanity has regularly helped keep me sane (although I'm sure you'd see it the other way around) so thank you. Very best of luck for the future to both of you.

I'd like also to thank all of the people I've been so lucky to share an office with over the last few years - Silvia, Jonny, Angese, Chris, Amy, Vicky and Veronica. Particular thanks goes to Amy for providing lashings of common sense (a rare commodity which cannot be underestimated) along with being a regular partner in crime. You're a great friend and I hope you go on to achieve your destiny by properly organising the world (beginning with Rich O.). My house mates also deserve much thanks, Michelle, Dee, Hannah and Alise thank you for being such lovely people and making life outside the university so pleasant. I also count Charly and Rich H. as surrogate house mates, particularly over the last six months. Thanks for keeping an eye on me both while I was writing up and before the viva, you're great people and I wish you every happiness together.

Finally I would like to thank my family, without whom this thesis would not exist and to whom it is rightfully dedicated. To David my big little brother - you are the funniest person I know, although I'm now officially qualified to say that you definitely didn't come from this planet! I can think of no-one better for you than the fabulous Jenny - be happy and live long. Most importantly of all, this goes out to my Mum and Dad - all of those trips to "Drodrell Bank" were worth it in the end! Thank you for being so completely wonderful, and for everything else.

Publications

A substantial amount of work contained in this thesis has been published in the followng papers:

L.M. Heil, S. Vaughan and T.P. Roberts "A systematic study of variability in a sample of Ultraluminous X-ray sources" *MNRAS*, **397**: pp. 1061-1072, Aug. 2009

L.M. Heil and S. Vaughan. "The linear rms-flux relation in an Ultraluminous X-ray Source" *MNRAS*, **405**: pp. L86-L89, Jun. 2010

L.M. Heil, S. Vaughan, P. Uttley "Quasi-periodic Oscillations in XTE J1550-564: The rms-flux relation" accepted for publication as a letter by *MNRAS*. ArXiv astro-ph:1011.6321

CONTENTS

Chapter 1

Introduction

When William Herschel first discovered the existence of infra-red light beyond the visible spectrum from the Sun he inadvertently opened the doors to a whole new world. The observation of celestial objects in wavelengths beyond the optical has revealed a sky containing sources of radiation infinitely more complex than was imagined only 200 years ago. At high energies we can now probe the formation and behaviour of exotic objects such as black holes and neutron stars. This thesis focusses on observations of emission from black holes at X-ray energies. Although our view of the X-ray sky beyond the Sun is less than 50 years old, observations in this band have widened and deepened our knowledge of some of the most energetic phenomena occurring in the Cosmos.

1.1 Viewing Black Holes

Black holes are one example of the extreme objects which high energy astrophysics, particularly in the the X-ray regime, has allowed us to probe. These objects are defined as regions of space-time where mass is so concentrated that velocity required to escape is greater than

the speed of light (c). For a non-spinning black hole the Schwarzchild radius defines this critical point $R_S = 2R_G = 2(GM/c^2) \approx 30$km M/10 $M_\odot$ after which light cannot escape, a mass entirely enclosed within its Schwarzchild radius is by definition a black hole.

Although light is not directly emitted from black holes themselves, we may observe them through indirect methods. Any matter accreted onto a black hole loses enormous amounts of gravitational potential energy as it travels towards the singularity. The infalling matter often also has significant amounts of angular momentum, which complicates this process as it needs to be lost before accretion can occur. It therefore forms an accretion disc around the black hole, the angular momentum it contains negates the possibility of direct accretion into the compact object. Once the material is in the accretion disc, viscosity will transfer angular momentum outwards and material travels inwards. Gravitational potential energy is then lost both into orbital motion and then through viscous dissipation into the immediate surrounding area, increasing the temperature of the gas. Current work suggests that this viscosity may be the result of the magnetorotational instability Balbus & Hawley (1991). The gravitational potential is higher as material moves closer to the Black Hole, therefore the amount of energy emitted increases inwards and a temperature gradient is created in the disc. This description is typically referred to as the 'thin' disc model originally suggested by Shakura & Sunyaev (1973), so called as the disc is geometrically thin, although it is optically thick. When talking about accretion within this thesis, the matter is assumed to be coming from a companion star within the system. The manner in which this is diverted towards the high mass compact object is discussed in section 1.3.1.

Close to the central black hole a point is reached after which stable orbits are no longer possible – the innermost stable circular orbit (ISCO). The position of this orbit relative to the Schwarzchild radius is dependent on the spin of the black hole, in the non-rotating case $R_{ISCO} = 6R_g = 3R_S \approx 90$km M/10 $M_\odot$, in the extreme spinning case (Kerr black hole) $R_{ISCO} = R_g \approx 15$ km M/10 $M_\odot$. Astrophysical black holes can be therefore described simply

by their mass and angular momentum (spin).

To approximate the luminosity emitted as the source accretes we make the following assumptions. If the source is spherically symmetric and a fraction (η) of the gravitational potential of the accreted material was lost before it reaches the event horizon then the accretion luminosity should be-

$$L_{acc} = \frac{2\eta GM\dot{M}}{R_S} = \eta\dot{M}c^2 \tag{1.1}$$

where $\dot{M}$ is the accretion rate and R is the radius of the source. There is also a factor η, describing the radiative efficiency. As black holes do not have a surface a certain amount of energy will reach the event horizon without being radiated. η is dependent on the spin of the black hole and the dynamics of the accretion flow, for a non-spinning BH $\eta \approx 0.06$, however around a maximally spinning Kerr black hole the efficiency rises to $\eta \approx 0.42$ (see Thorne, 1974; Frank et al., 2002).

At a certain accretion rate, the infalling matter will be stopped by the radiation pressure from the photons being emitted. This point is referred to as the Eddington limit, nominally it describes the upper limit on luminosity from a source and is chiefly defined by the source mass. If the gravitational force inwards is defined as

$$F_{grav} = \frac{GMm_p}{R^2} \tag{1.2}$$

where m_p is the mass of a proton. The force applied by the radiation outwards is

$$F_{rad} = \frac{\sigma_T L}{4\pi R^2 c} \tag{1.3}$$

Based on a spherically symmetric object steadily emitting with a flux of $L/4\pi R^2$ at radius R. σ_T is the Thomson cross-section, this equation assumes that the accreting matter is pure hydrogen gas. The Eddington luminosity is defined at the point where these two forces are equivalent, equating them and re-arranging for the luminosity gives

$$L_{Edd} = \frac{4\pi G M m_p c}{\sigma_T} \tag{1.4}$$

Therefore $L_{Edd} \approx 10^{38}(M/10M_\odot)$ erg s^{-1}. Typically a source might not be expected to emit above this limiting luminosity, although super-Eddington accretors are observed and are discussed in section 1.4.3.

1.2 Emission processes

One method used to probe the environment close to the black hole is through studying the energy dependence of the emitted radiation. For the work in this thesis the main relevant emission processes are blackbody emission and inverse Compton scattering – primarily observed in the X-ray emission from black hole X-ray binaries. However other production mechanisms are briefly included for completeness. These radiation processes are discussed in detail within Tucker (1978) and Rybicki & Lightman (1986).

1.2.1 Blackbody radiation

If a system absorbs then emits all radiation incident upon it in thermal equilibrium it is a blackbody. All objects with any form of heat emit thermal radiation, the emission from black body objects has a very characteristic spectrum. The peak of this spectrum directly relates to the

temperature of the emitter, although it produces emission over a wide range of wavelengths. This relation between the peak wavelength emitted and the temperature is described by Wein's displacement law-

$$\lambda_{max} = \frac{b}{T} \tag{1.5}$$

where b is a constant $b = 2.897 \times 10^6$ nm K. Thus hot objects emit at shorter wavelengths and we expect to see the peak at higher photon energies for these sources. If the accretion disc surrounding a black hole is optically thick, all photons are scattered within it, then we expect the emission from the disc within a localised region to be approximate to that of a blackbody. The shape it takes is discussed later in this introduction in section 1.3.4.

1.2.2 Compton processes

The scattering of photons off electrons is described as either Compton or inverse Compton scattering depending upon which direction energy is transferred. In the former the photon loses energy to the electron, in the latter the photon gains energy - it is this process which is most important for the sources discussed here. A diagram of inverse Compton scattering is given in Figure 1.1.

Inverse Compton scattering of photons into the X-ray regime occurs in hot ($T_e \sim 10^9$ K) conditions where the population of electrons has a high fraction of kinetic energy relative to that of the photons. The spectrum produced is a non-thermal power law, due to either an underlying power-law energy distribution of scattering electrons or multiple scatterings by a non-power law distribution. Generally the resulting spectrum is approximately a power law in the X-ray band, ranging from the typical seed photon energy to the typcal electron energy. The effect of Inverse Compton scattering on the energy spectra is discussed in more detail in

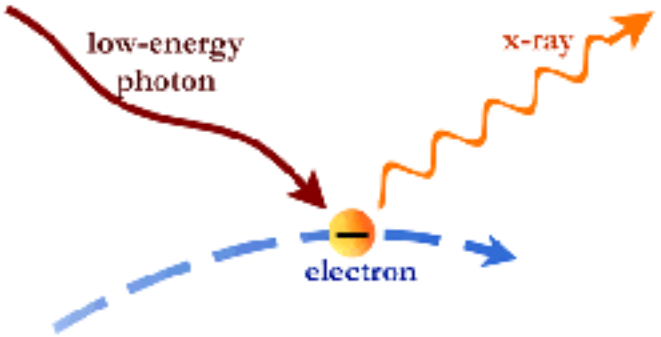

Figure 1.1: Diagram of inverse Compton scattering, taken from `http://chandra.harvard.edu/graphics/resources/illustrations/xlightScatter-72.gif`

section 1.3.4.

1.2.3 Bremsstrahlung

Bremsstrahlung, or free-free radiation, originates when a charged particle, such as an electron, passes by a positively charged ion causing the electron to be deflected releasing radiation. In ionised gas both the ion and the electron are not bound either before or after the collision, hence free-free emission. The motion of electrons and ions within the gas and the resulting interactions will produce a continuous spectrum with a sharp cut-off, that of thermal Bremsstrahlung.

1.2.4 Synchrotron emission

Electrons interacting with strong magnetic fields may be accelerated, radiating photons as they travel. Relativistic electrons spiral along the magnetic field lines emitting synchrotron radiation, if the electrons are non-relativistic then the emission is cyclotron rather than synchrotron

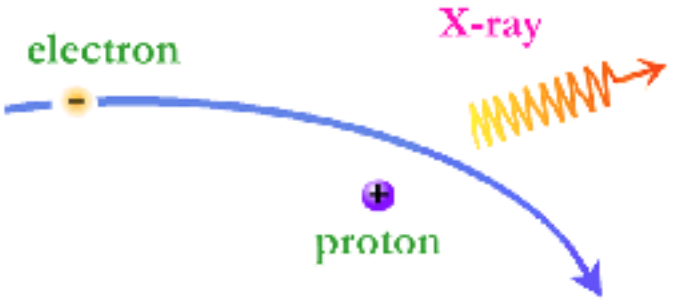

Figure 1.2: Diagram of Bremsstrahlung, taken from `http://chandra.harvard.edu/graphics/resources/illustrations/xlightCollision-300.gif`

Figure 1.3: Diagram of synchrotron emission, taken from `http://chandra.harvard.edu/graphics/resources/illustrations/xlightRadiate-300.gif`

but it is the former which is relevant close to compact objects. The amplitude power radiated is dependent on the energy of the electron, the strength of the magnetic field and its velocity relative to the field. If the initial energy distribution of electrons is of a power law form, the spectra produced should also be a power law with an index related to that of the original electron energy distribution.

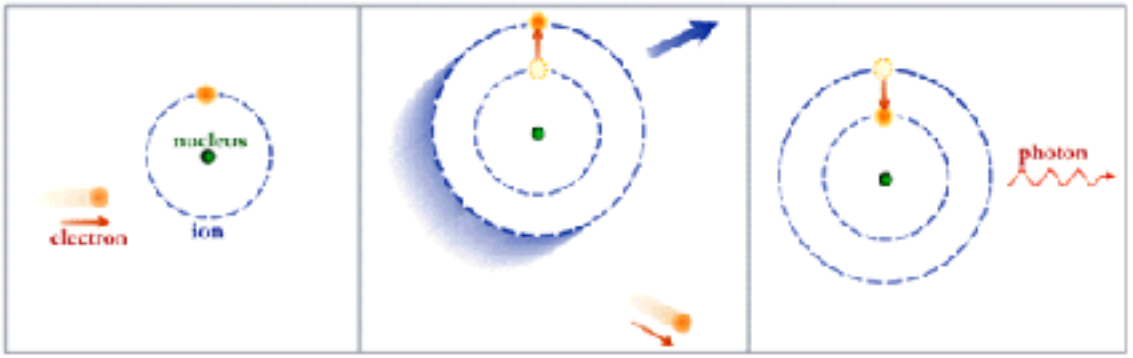

Figure 1.4: Diagram of Line emission, taken from `http://chandra.harvard.edu/graphics/resources/illustrations/xlightEmit-300.gif`

1.2.5 Line emission

Emission lines from hot plasmas are caused by the transition of electrons within atoms from higher to lower excitation states. Collisions with a free electron, ion or photon can cause the bound electron to be excited – it may reach a higher energy level, or be ionised and freed altogether. If the electron is not released it later decays, this may occur in one jump or through a series of steps, each of which has a specific drop in energy associated with it. Photons are thus released with these energies and this produces the characteristic line features in the final spectrum. A secondary process of radiative recombination also creates emission lines – a free electron is captured by an atom becoming bound. At this point it may either directly reach the ground state, in which case the photon produced is related to the initial energy of the electron, or to an excited state and then cascade down the energy levels producing line emission, in the manner previously described.

1.2.6 Pair annihilation

Finally, radiation can also be produced when a particle and its anti-particle interact and annihilate each other. Two photons are emitted which between them share the total energy and momentum of the original particles. In the case of an electron and a positron annihilating, the energy of a resulting photon must be at least $m_0c^2 = 0.511\ MeV$ corresponding to emission in the γ-ray regime.

1.3 Black Hole X-ray binaries

Galactic Black Hole X-ray binaries (BHBs) consist of a stellar mass black hole in a system with a non-degenerate secondary star. These black holes are typically the products of massive star collapse during the evolution of binary systems. In these cases the mass of the black hole can be estimated from observations of the companion. If the radial velocity measured from the companion's spectra reveal a periodic signal, so the period and radial velocity of the system can be estimated then the mass function for the system may be derived and the lower limit on the mass of the compact object inferred. Cygnus X-1, the first identified BHB, was initially detected in X-rays during a rocket flight (Bowyer et al., 1965). When an optical counterpart was found within the X-ray error box and identified as a high mass star with a clear periodicity from the radial velocities of 5.6 days (Murdin & Webster, 1971). This suggested that the mass of the unseen X-ray emitting companion must be greater than $2M_\odot$ leading to the conclusion that it could be a black hole (Webster & Murdin, 1972). Later derivations of the mass ratio further confirmed this conclusion (Bolton, 1972). X-ray variations on timescales of 100 ms had already been observed from Cyg X-1 by *Uhuru* (Oda et al., 1971), further confirmation that this was an accreting compact source. Both this and LMC X-3, the next confirmed BHB, are now known to be high mass X-ray binaries (HMXBs) i.e. their companion is a massive

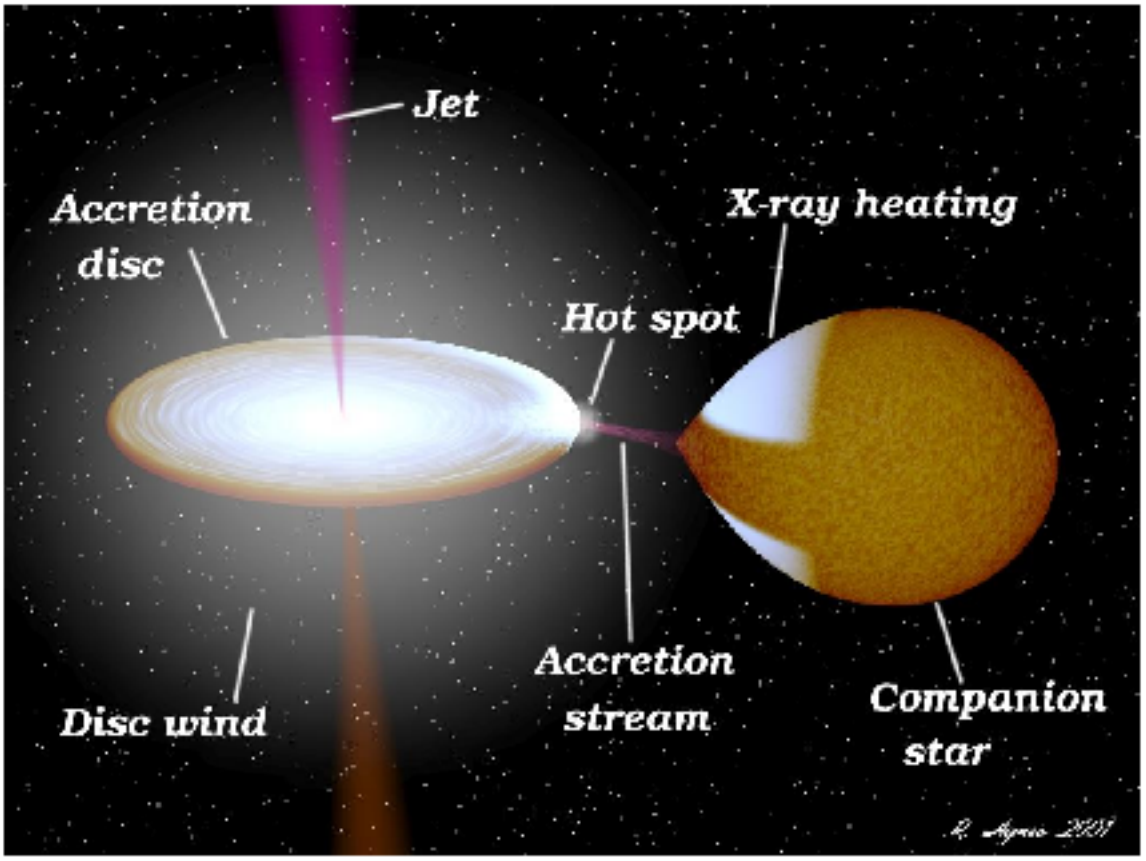

Figure 1.5: Cartoon of a black hole binary system, showing accretion through a Lagrange point via Roche Lobe overflow. Image made by Rob Hynes.

O/B spectral type supergiant. The next identified class of BHBs were those with low mass companions (LMXBs) and these showed quite different behaviour. A 0620-003 was only observed when it went into outburst in 1975, suddenly brightened to a level of $\sim$ 50 Crab ($\sim 1.45 \times 10^{-6}$ erg s^{-1} cm^{-2}) and then slowly decayed (Elvis et al., 1975). This source was only the first of a whole group of black hole X-ray transients which have now been observed going into outburst, often repeatedly. The properties and behaviour of these two groups of sources are discussed in the following sections.

1.3.1 Accretion methods

LMXBs - Roche Lobe Overflow

When the companion star is less massive than the compact object, accretion occurs primarily through Roche lobe overflow. Surfaces of equipotential exist between the two potential wells formed by the objects in the system. A point at which a small mass is allowed (by the combination of the equipotential and centrifugal forces) to remain stationary relative to the two stars is termed a Lagrange point. Five of these points exist within a binary system, as illustrated for an example system in Figure 1.6. The equipotential surface which passes through the first Lagrange point (the thick black line on this figure) defines the Roche lobes for the objects. During evolution the secondary star expands, filling its Roche lobe and then overflowing. At this point the excess matter is directed in a thin stream through the first Lagrange point and on towards the compact object. The lifetime of LMXBs is therefore determined by the length of time taken for the secondary to lose the expanding envelope until it no longer fills its Roche lobe – $\sim 10^7 - 10^9$ yr (for full discussion of the evolution of these objects see e.g Tauris & van den Heuvel, 2006)

HMXBs - Wind Accretion

Relatively few of the confirmed black hole X-ray binaries (~ 3) have high mass stellar companions ($3 < M < 10\ M_\odot$), far more of these systems are observed where the compact object is a neutron star. Only one well observed HMXBs (Cygnus X-1) is within the Galaxy, the other two are in the Large Megallanic Cloud, for this reason the formation and accretion mechanisms of these objects are less well understood than the NS systems (Brown et al., 2000). The high mass companion star sets these systems apart due to their ability to drive strong winds. Accretion from the secondary occurs when the gravitational potential well of the compact object

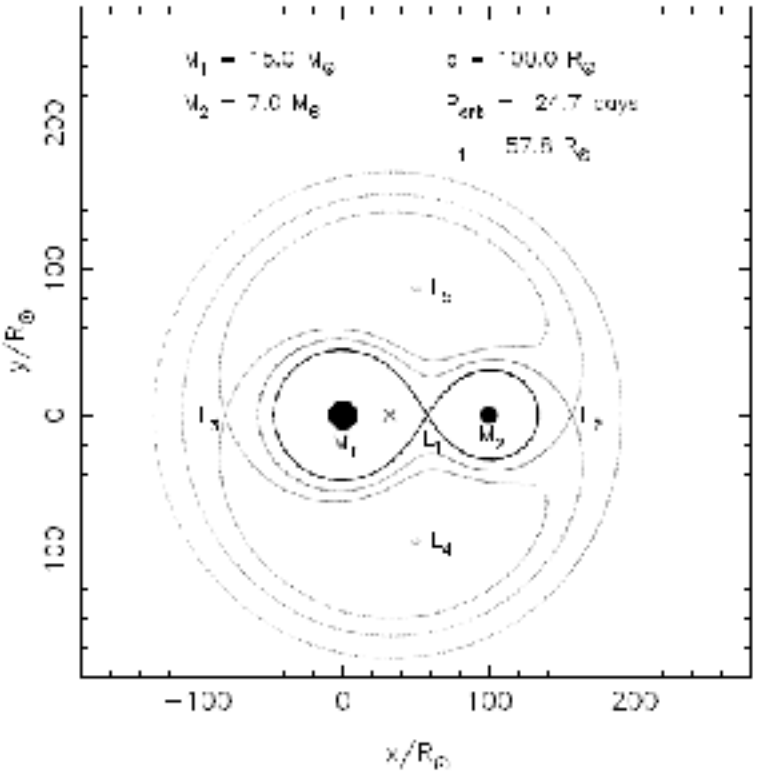

Figure 1.6: Illustration of the five Lagrange points and equipotential surfaces for an example system, taken from Tauris & van den Heuvel (2006)

captures the wind and focusses it inwards towards the accretion disc, although bright sources may also be accreting via Roche-lobe overflow (see e.g. Negueruela, 2010). The accretion rate in these systems is therefore highly sensitive to the wind properties, such as velocity, density and ionisation. The evolution of this secondary is relatively fast, meaning that the lifetime of HMXBs ($\sim 10^5 - 10^7$ yr) is shorter than that of LMXBs (see e.g Tauris & van den Heuvel, 2006).

1.3.2 Transiency and outbursts

Although HMXBs are observed as persistent X-ray sources, LMXBs are generally transient and new objects are only detected once they go into outburst. These outbursts may last from weeks to months with gaps of years between their appearance, one source, GRS 1915+105 is

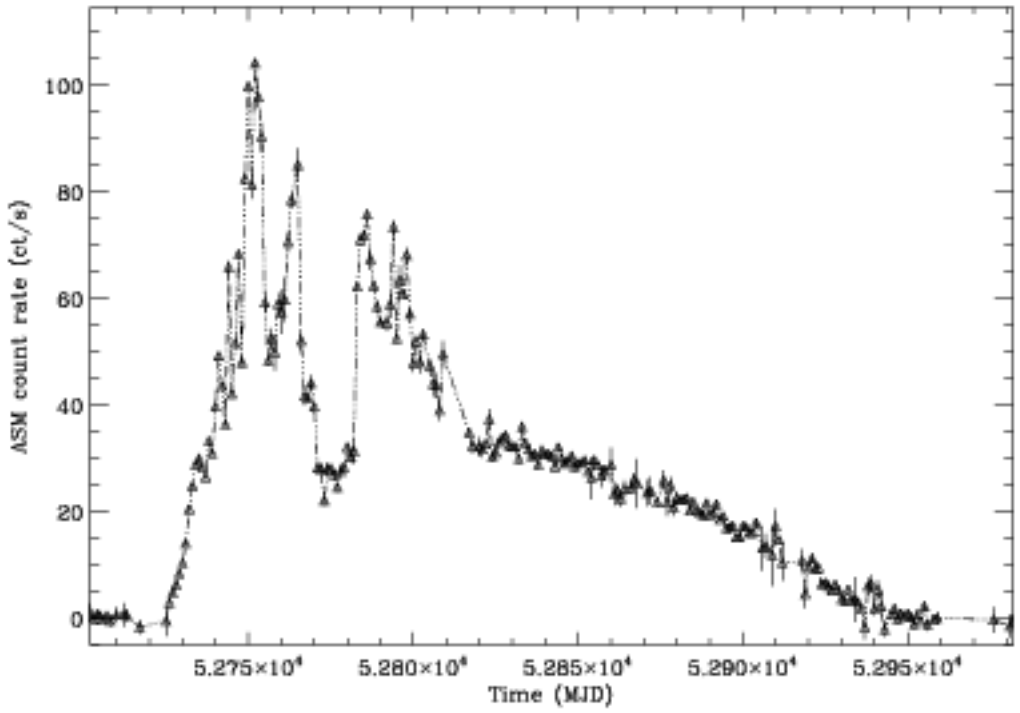

Figure 1.7: Outburst of the LMXB H1743-322 as observed by the all-sky monitor on *RXTE*.

thought to be a transient LMXB, but has been in outburst since 1992. In the past sixteen years the monitoring capabilities of *RXTE* have allowed transient sources to be closely monitored during these bright periods. Observations of repeated outbursts in a number of sources show that there are clear similarities in behaviour within each outburst, distinct "states" are visible both in the energy spectra and the short term variability, which appear in all sources with remarkable similarities between them. I now discuss some of the observational characteristics of these states, and the models put forward to explain them.

1.3.3 State changes in BHBs – Hysteresis

States in black hole X-ray binary systems were originally defined by a combination of the energy spectra and the flux. The first change of state in a BHB was observed in Cygnus X-1 in observations by *Uhuru*, the system transitioned from a state dominated by soft X-

rays (2-6 keV) to one mainly emitting in higher energy range (10-20 keV). During this time a radio counterpart associated with the source was observed to turn on (Tananbaum et al., 1972). These two states were then observed in other sources and seemed to be linked to the luminosity. The soft state was generally observed at during bright periods and so referred to as "High/Soft" (HS). The hard state when the source was fainter, thus "Low/Hard" (LH). Further observations of transient sources indicated that the two initial states were insufficient for a full explanation. States which did not fit into either of these two categories were then given a range of different names dependent on their flux or spectral appearance (i.e. "Intermediate", "Very High", "Steep power law"). Following the launch of *RXTE* the ability to observe an object at regular intervals over the course of an outburst meant that far more data on the range of states became available. Plotting the hardness ratio of observations within an outburst against the flux in a hardness-intensity diagram (HID), revealed a q-shaped hysteresis curve followed by the source clearly showing gradual evolution and blurring the edges between the zoo of states previously defined (see e.g. Homan et al., 2001; Belloni, 2004; McClintock & Remillard, 2006a; Belloni, 2010a). Energy spectral models make assumptions about the origins of various components, using the HID to define states reduces the reliance on these models being correct.

The uncertainty over exact designation of states has led to a disparate nomenclature, particularly for those which clearly fall outside the classic HS/LH boundaries. For this reason the same observation may have a different label according to when the analysis was carried out. It is therefore important to define what is meant by each of the names used herein, where the observations in this state are likely to appear on the HID, and the timing behaviour observed at each point. In Figure 1.9 examples are given for each of the states normally used in this thesis, along with other names also used for a similar state, this demonstrates the evolution of the both the energy and power spectra over the course of an outburst.

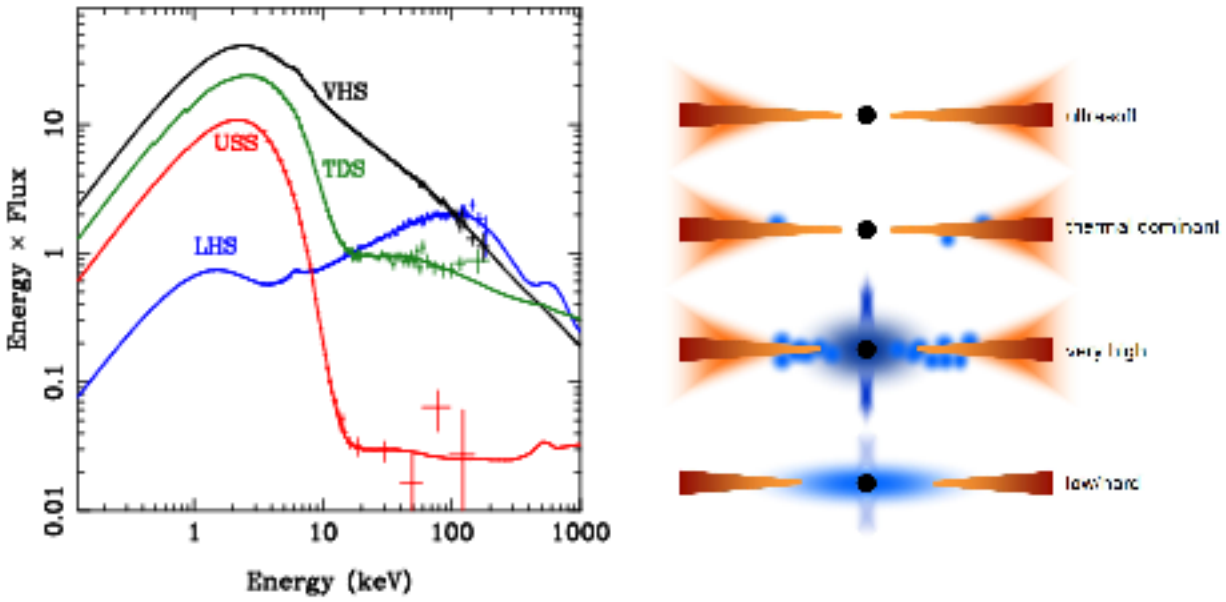

Figure 1.8: One proposed model for the evolution of the accretion flow close to the black hole, shown with example energy spectra from GRO J1655-40 from Done et al. (2007). As the source moves into the soft states, the inner edge of the disc moves closer to the compact object, the jets switch off, and the corona reduces in size. The ultra-soft state is a form of soft state with a very weak power-law tail and the very high state corresponds to the intermediate states, as described below.

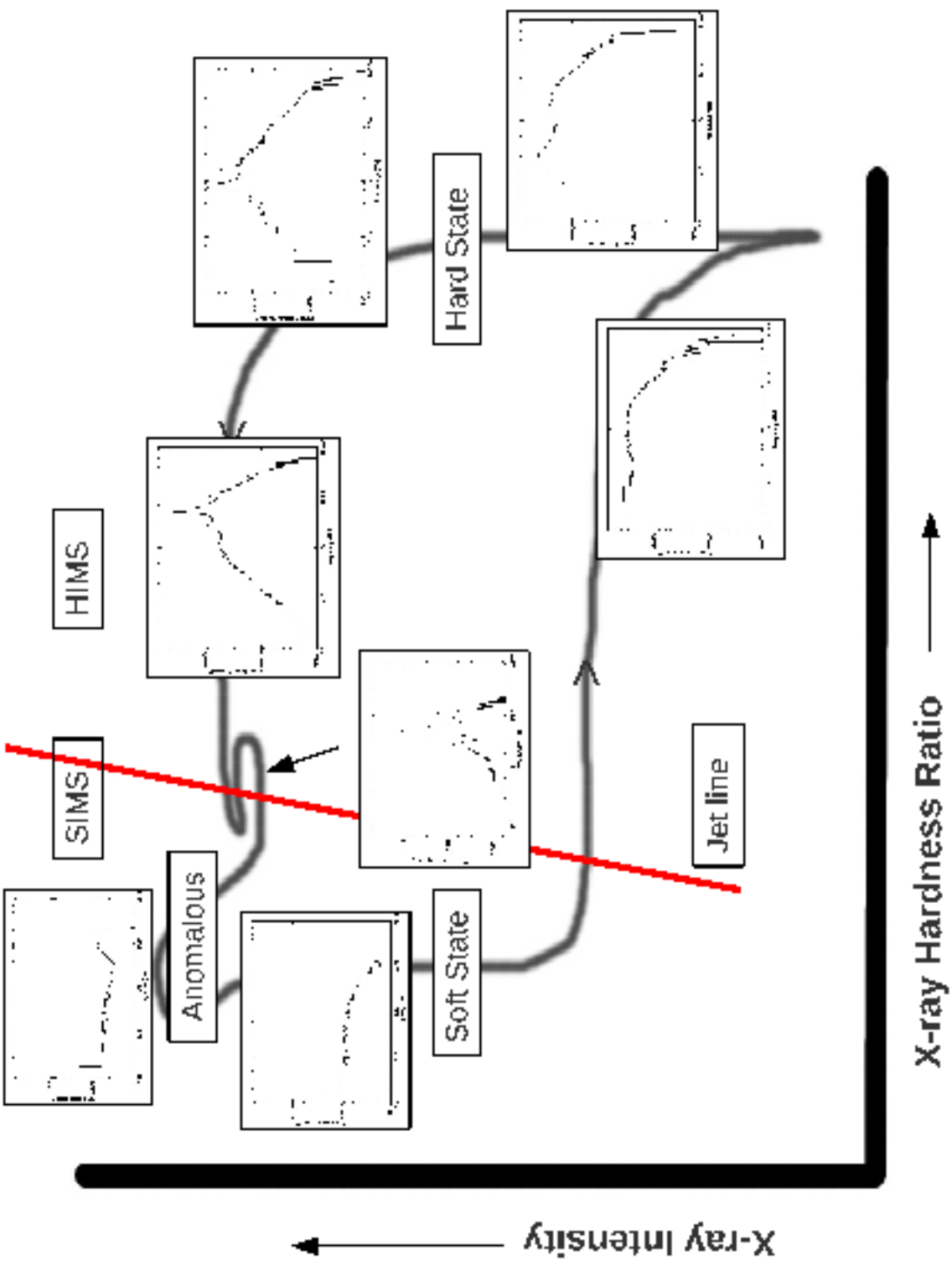

Figure 1.9: Cartoon of a hardness intensity diagram with example power spectra from each point on the Hysteresis curve.

1.3.4 Energy Spectral components

The energy spectra of BHBs typically consist of two main components – one non-thermal and the other thermal. The strength of these two components changes with state. In the soft state the thermal component dominates at lower energies, whereas in the hard state the non-thermal component is stronger in the high energy region. In general the thermal component is modelled by some variation on a multi-coloured disc model. The temperature of the accretion disc increases towards the black hole, therefore the peak of the blackbody emission from each consecutive annulus also rises in energy (see section 1.2.1). The resultant spectrum is a sum of various blackbody spectra each with a different temperature, in a BHB the component typically peak at kt $\sim$ 1keV ($T \sim 10^7$ K) in states where it is clearly visible. The inner radius of the accretion disc can then be derived from the highest peak temperature and the luminosity, possibly allowing for constraints to be placed on both the inner disc edge and the black hole spin (see e.g. McClintock & Remillard, 2006a). Figure 1.8 shows the evolution of the energy spectra over the course of an outburst.

The non-thermal component is typically modelled with a power law arising from repeated inverse Compton scatterings in a hot optically thin corona. The observed index is generally $\Gamma \sim 1.7$ in the hard state and $\Gamma \sim 2-3$ in the soft (see reviews such as Reynolds & Nowak, 2003; McClintock & Remillard, 2006a; Gilfanov, 2010; Done, 2010). The shape of this power law is dependent on the state of the source – in the hard state a high energy turnover is observed which is not present in the soft state. If the hot Comptonised electrons are from a thermalised area there will be a roll over at high values close to the scattering electron energy, typically observed in the hard state. If the electron distribution has a high energy non-thermal component, then the Compton tail may extend to much higher energies. The top end of the power-law is governed by the highest energy of the scattering electrons, as observed in the soft state (see e.g. Gilfanov, 2010; Done, 2010, and references therein).

In addition to these two main components an emission iron line at 6.4-6.9 keV and 'reflection' spectrum are often detected in the energy spectra of some black hole binaries, thought to be caused by a combination of line emission and reflection of photons from the comptonised corona back onto the disc. Relativistic effects, such as beaming and redshifting as the disc rotates make the line profile asymmetric. This asymmetry combined with the extension of the line profile have been used to derive values for both the black hole spin and the inner stable circular orbit (see Reynolds & Nowak, 2003; Done & Diaz Trigo, 2010; Hiemstra et al., 2009, 2010, and references within).

For spectral analyses there remains a great deal of uncertainty about the geometry and dynamics of the disc and corona. These may instead be investigated through the characteristics of their variability, understanding the behaviour of the accretion flow for different timescales

1.3.5 Power Spectral components

Fourier analysis techniques are regularly used to evaluate the variability properties of lightcurves from astrophysical sources. Probably the most commonly used tool is the power spectrum, which on the most basic level shows the power (the square of the Fourier amplitudes) of the variability as a function of the frequency (ν), this is further discussed in detail in Section 2.2. The integrated area under the power spectra gives the amount of variance in the lightcurve over that frequency range. It is generally plotted on a log-log scale, sometimes with $P \times \nu$ on the y-axis (where P is the power). In these units small variations in power laws become clearer and it becomes easier to compare the integrated power in components at different frequencies, as it represents this quantity in equally spaced logarithmic frequency intervals, making it a useful visual reference. Both forms of plotting (with just P on the y-axis or with $P \times \nu$) are used throughout this thesis.

As well and broad noise components power spectra can also feature sharp components such

as quasi periodic oscillations (QPOs). These are not strictly periodic as, although they are narrow, their power is spread over a range of frequencies and their shape can be approximated by a Lorentzian. A peak is typically defined as a QPO if the quality of the peak is greater than 2 ($Q = \nu_{peak}/FWHM$ where ν_{peak} is the peak frequency of the QPO and FWHM is its full width at half maximum) (van der Klis, 1989a).

The power spectra are also observed to evolve gradually over the course of an outburst, and this evolution can be closely linked to that of the energy spectrum. Timing properties such as the power spectrum and time lags reveal timescales and therefore estimate absolute size scales within the system. Explaining how the various power spectral features relate to structure at the source is difficult however, not least because the similar characteristic frequencies are commonly observed across all sources – regardless of different masses for both the compact object and its companion or orbital periods. There are various different models used to fit power spectra (For discussions of these models see Nowak, 2000; Belloni et al., 2002; van der Klis, 2006). The broad-band noise from power spectra has been fitted with multiply or singly broken or bending power laws (Nowak et al., 1999), a series of Lorentzians (Nowak, 2000), or a combination of the two dependent on source state – the method which is now most typically used. Generally power spectra in the hard states can be fitted with a series of broad Lorentzians, whereas those in soft states require additional power law components to fit the observed low frequency shape (see e.g. Klein-Wolt & van der Klis, 2008).

Hard states have particularly complex power spectral shapes, 3-4 Lorentzians may be used to describe the broad band noise, with up to 4 additional narrow components required to fit any QPO component with harmonics and sub-harmonics (see Klein-Wolt & van der Klis, 2008, for examples). There is no strict naming convention for these components, although Klein-Wolt & van der Klis (2008) clearly describe one which may be used, and exact differentiation of one feature from another may prove difficult. An example hard state power spectra, fitted with a combination of Lorentzians labelled using the naming convention for the work presented

here is shown in Figure 1.10. In contrast power spectra in soft states are generally well fitted by a power law bending at around 4.0 Hz from an index of ~ -1 to ~ -2.

Various correlations have been identified between power spectral components, some of which apply to both neutron star and black hole binaries, although these are obviously dependent on the model used to fit the power spectra. These include correlations between the low frequency QPO and peak of a broad-band noise component (Psaltis et al., 1999) and the low frequency QPO with the break frequency (Wijnands et al., 1999). Correlations are also clearly visible between the frequency of the components and their strength, such as that identified in Belloni et al. (2002) between break frequency and the power level. These correlations are further discussed in Chapter 6. Since this initial work it has become clear that many of these components evolve together as the sources go into outburst. Rao et al. (2010a) show that many of the components move up in frequency together as the source hardens and that many remain harmonically related. This behaviour is also similar to that observed in Neutron Star binaries – for examples see van der Klis (2006).

Origins of the X-ray variability

Although it has not yet proven possible to directly associate components within the power spectra to specific properties of the source, the variability has been linked to various energy spectral properties in a more general manner.

A positive correlation has been found between the amplitude of variability within a time interval and its mean flux. This relation has been observed for timescales of several years for approximately identical power spectral shapes (Uttley & McHardy, 2001; Gleissner et al., 2004). This is referred to as the rms-flux relation and is the subject of Chapters 4, 5 and 6. This relation has been observed in a range of different accreting compact objects (BHBs, NS and AGN), as well as from BHBs in optical wavelengths (see e.g. Uttley, 2004; Vaughan et al.,

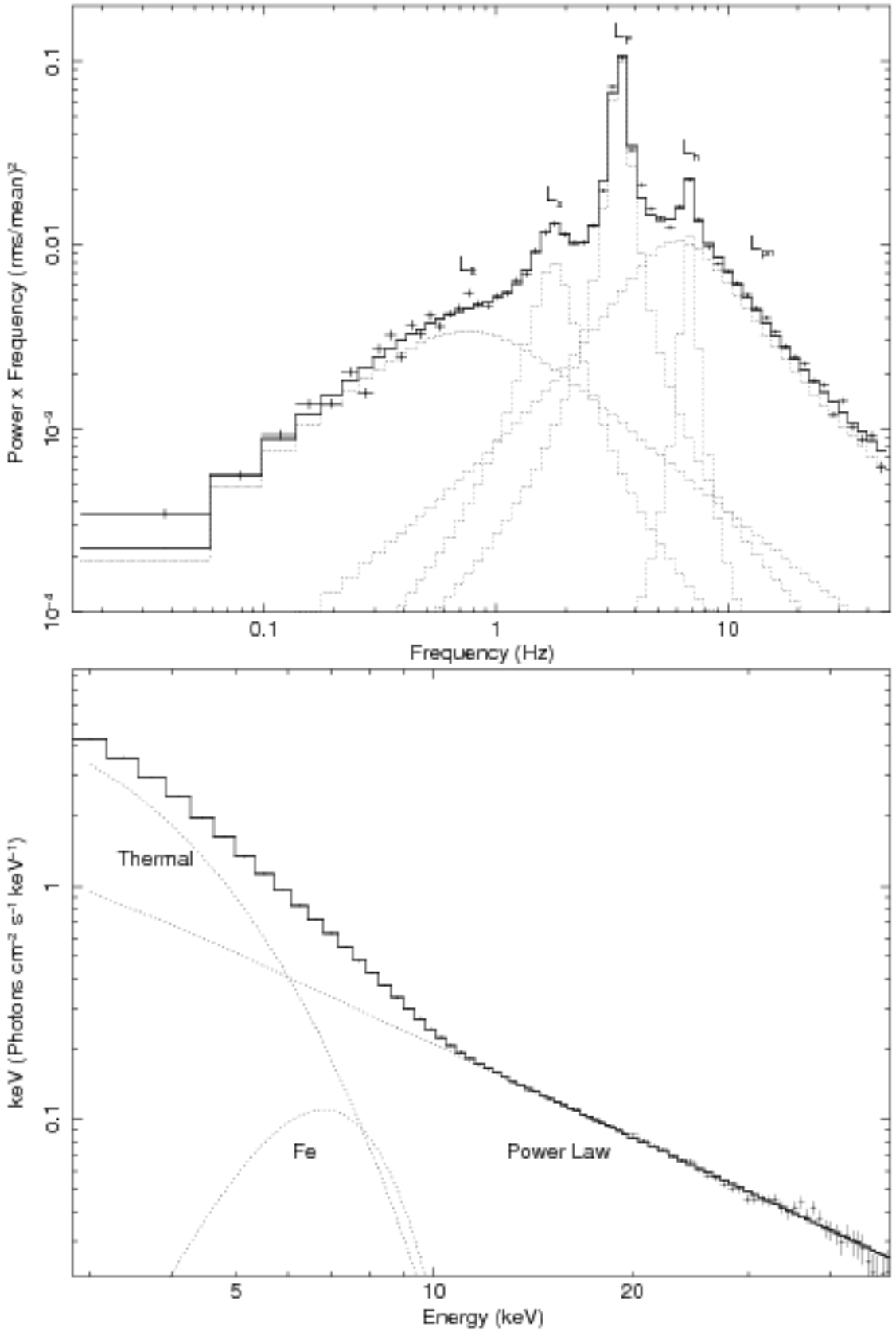

Figure 1.10: *Top.* Example power spectra in the Hard state fitted with multiple Lorentzians each labelled with the convention used throughout this thesis. *Bottom* Example energy spectra in the thermally dominated state showing the thermal (DISKBB) and power law (POWER) components and indicating the presence of an unresolved iron line.

2003a; Gaskell, 2004; Uttley et al., 2005; Gandhi, 2009). Early models of X-ray variability were based on shot noise – the superposition of independent pulses of emission which can reproduce practically any power spectral shape (Lehto, 1989; Doi, 1978), many of these models could reproduce power spectral shapes such as those seen from Cygnus X-1 but the shots are independent over a range of timescales and so cannot reproduce a linear rms-flux relation over a range of timescales (Uttley & McHardy, 2001). It is therefore more likely that the variability over all timescales is coupled. One model, suggested by Lyubarskii (1997), where long term variations from the outer edges of the disc propagate inwards multiplying together with faster variations at smaller radii and eventually creating the observed light curve, seems to provide an obvious solution. Simulations mimicking this multiplication effect (through exponentiation of a lightcurve simulated with a particular power spectral shape) can be used to recreate the linear relation between variability and flux observed over all timescales in lightcurves from other sources (Uttley et al., 2005).

1.3.6 Characteristic properties of the Energy and Power Spectra in various states

The launch of *RXTE* allowed for consistent monitoring of transient sources over the course of outbursts. It became clear that sources frequently reached states which did not fit into the high/soft or low/hard groupings. For this reason the classification of observations into states is inconsistent and still evolving. Although energy spectra and flux have historically been used to classify observations it has become clear that the most obvious transitions occur in the timing. In this section I define the states as they are referred to within this work, generally following the nomenclature from Belloni (2010b). Crucially these states are defined through the shape of the power spectra instead of the energy spectra as it is the variability which is studied here. Other names used for these states are also referred to and explained.

Quiescence

All confirmed LMXBs have been observed in quiescence, excluding GRS 1915+105 which has been in outburst since 1992 and has not entered quiescence since its discovery (Tomsick et al., 2005). Most of these sources show exceedingly low X-ray luminosities in these quiescent states generally $< 10^{32}$ erg s^{-1} (Tomsick et al., 2003), so $L/L_{Edd} \sim 10^{-7}$, this is remarkable as the luminosities of LMXBs reach luminosities close to $L/L_{Edd} \sim 1$ at the peak of an outburst and as a consequence the count rates are low so drawing full conclusions about the properties of this state is very difficult. The launches of *XMM-Newton* and *Chandra* have allowed for observations of BHBs to be made in this very faint state. In general the source properties in quiescence are assumed to be very similar to the standard hard state. Evidence of radio emission from a jet with a power-law dominated energy spectra and strong aperiodic variability is expected. Radio emission from a source in a quiescent state has been observed in A0620-00 (Gallo et al., 2006), as well as from V404 Cyg and GX339-4, however Calvelo et al. (2010) failed to detect either GRO J1655-40 or XTE J1550-564 in observations providing quite stringent upper limits on emission from both sources and suggesting that these sources are more radio quiet than others when in quiescence.

Determining the exact nature of the X-ray spectra is hampered by the low count rates. If the quiescent state is indeed an extension of the hard state down to low flux levels, then the energy spectrum is expected to be dominated by a strong non-thermal power law. In general this is what has been observed with indices between $\Gamma = 1.5 - 2.1$, McClintock & Remillard (2006a) provide a review of these observations up to 2003 (see also Kong et al., 2002, for a discussion on the use of a Comptonised model). Corbel et al. (2006) examined a set of seven observations of XTE J1550-564 by *Chandra*. Simultaneous fitting of all observations indicated that the energy spectra did not change significantly, although large changes in the flux were observed. They suggest that the observed photon index ~ 2.25 is softer than those typically observed in the hard state and that this softening may also be observed in the other

black hole binaries XTE 1118+480 and GX 339-4, which could indicate a difference between the typical hard state and quiescence in some sources.

The other significant property of BHBs in the hard state is the presence of strong aperiodic variability. Again the low observed count rates mean that this can only be tested at relatively long timescales, or with the more powerful X-ray telescopes. Tomsick et al. (2004) used a long observation taken by *Chandra* to measure the power spectra of XTE J1650-500 as it dropped from the hard state into quiescence. They observed strong aperiodic variability below ~ 0.4 Hz, and possible evidence for a QPO at 0.11 Hz. Corbel et al. (2006) used a 26 ks observation of XTE J1550-564 when it was relatively bright (0.46 ct s^{-1}), binned the lightcurve up to 1 ks and saw clear evidence for variability over this timescale, suggesting that short-term variability is still present and therefore that the source properties may be similar between the hard state and quiescence.

The Hard state

The hard state is observed at the start of the outburst as the source initially brightens and again before it drops back into quiescence. The energy spectra is typically dominated by a power law with an index of ~ 1.7 and a high energy turnover as discussed in section 1.3.4. The index remains relatively consistent whilst the source brightens, generally steepening slightly (see e.g. McClintock & Remillard, 2006a, for examples from a range of sources and outbursts).

Once the flux from the source is high enough to detect short-timescale variability the power spectra are also observed to gradually evolve as the flux rises. In this state the variability is strong with a fractional rms level > 20 %. The multiple Lorentzians often used to fit power spectra in the hard state (as discussed in Section 1.3.5) shift as the state changes. Initially starting at low frequencies, as the source brightens the peaks of these Lorentzians are observed to move up in frequency, in line with the steepening power law component observed in the

energy spectra (a good example of this behaviour can be seen in Rao et al., 2010a). In the hard state a low frequency (< 10 Hz) QPO is often observed, commonly with both sub and higher harmonics, this QPO is referred to as Type "C" (Remillard et al., 2002). This component shifts up in frequency along with the other Lorentzians. Initially observed at frequencies of ~ 0.01 Hz or even lower it has risen in frequency to above 2 Hz before the source transitions out of the hard state. Throughout this work the strongest QPO feature is assumed to be the fundamental component, although this may not necessarily be true Rao et al. (2010a) expand upon this point.

The increases in frequency observed over the course of the outburst have been interpreted as evidence for the inner edge of the disc moving inwards. In this case if the corona is positioned between the inner disc edge and the black hole then the inner edge of the accretion disc moving to smaller radii, reducing the size of this region could explain the increasing characteristic frequencies within the power spectra.

Radio emission is observed from objects in the hard state, interpreted as evidence of a constant compact jet. This has been seen in a range of sources – for a recent review see Fender et al. (2009). In some cases the compact jet has been resolved (Dhawan et al., 2000; Stirling et al., 2001; Corbel et al., 2002). The detected radio emission in the hard state is optically thick, has an approximately constant spectral index and appears to be steady (e.g. Gallo, 2010).

The Hard Intermediate State (HIMS)

The hard intermediate state is sometimes referred to as the very high state or the steep power law state. As suggested by these names, sources in this state are bright and close to the peak flux of the outburst if the source remains non-thermally dominated. On the HID, observations in the HIMS are first seen in the top right hand corner and persist as the source softens and moves to the left. The power law in the energy spectrum is observed with indices > 2.4, and the

contribution from the thermal component (presumably the disc) is often observed to increase, preceding the change into a soft state (see examples in McClintock & Remillard, 2006b; Dunn et al., 2010). Radio observations indicate that a persistent compact jet is still present.

The observed variability remains at high levels but begins to drop whilst the source is in this state. The power spectra gradually evolve from the hard state into the HIMS, all components moving up in frequency until the broad-band noise becomes strongly peaked. The type "C" QPO and its associated components moves up in frequency with the noise and is visible above ~ 2 Hz, reaching as high as ~ 15 Hz.

Transitions around the jet line and the soft intermediate state (SIMS)

Dramatic changes are observed in both the X-ray timing and radio properties when the object transitions from a HIMS to the SIMS. A very rapid transition in power spectral shape is seen on timescales < 1 day, the peaked broad band power observed in the HIMS disappears almost completely, although the QPO component remains with the fundamental typically ~ 6 Hz and a low frequency power law appears. This type "B" QPO (Wijnands et al., 1999; Homan et al., 2001) is very similar to the type "C" observed in the hard states, and is usually accompanied by harmonics and sub-harmonics. The transition to this power spectral shape may occur once before the source moves into the soft state, or a number of times inbetween observations of a typical HIMS or hard state power spectra with strong broad-band noise, again these transitions can occur over very short (< 1 day) timescales.

The transition is accompanied by a radio flare and then quenching of the radio emission. The point on the HID at which this quenching is observed to occur is referred to as the jet line. To the right, the jet is observed whereas to the left it is not. Fender et al. (2009) have investigated the peak radio luminosities in combination with the alterations in the variability. They do not observe a one-to-one correlation over time between timing transitions and radio flares but

conclude that both features are closely connected, appearing within a few days of each other.

Over the course of the transition from the hard to the soft state the thermal contribution gradually increases and then dominates. The distinct transformation from state to state observed within the variability does not appear to be as clearly observable in the energy spectra. Dunn et al. (2010) have carried out a systematic study of these transitions and discuss their identification using the energy spectra thoroughly. They confirm that although the fastest changes to the energy spectra occur during the state transitions to and from the hard state, the dramatic changes in variability are not replicated in the energy spectra.

Anomalous soft states

Whilst the source is still very bright, soft so called "Anomalous" states may occur where the energy spectra appear different to those observed in the typical soft-state. They are somewhat similar to those observed in the HIMS, with a very steep non-thermal component and a soft component which is not necessarily dominating the flux (Sobczak et al., 1999; Belloni, 2010b).

The power spectra in this state are often a combination of those observed in both the hard and soft states with the amount of variability observed higher than that seen in a true soft state. A power law bending from an index of ~ -1 to ~ -2 with the break frequency observed around 4–5 Hz is the typical PSD shape observed in the soft state. In the anomalous state this bending power law may be combined with a high frequency peaked noise component, sometimes defined as a type "A" QPO. Occasionally more than one QPO peak is clearly visible. This component can be quite strong and is usually observed above ~ 3 Hz (McClintock & Remillard, 2006a). The fractional rms is higher than that typically observed in the soft state, generally $6 - 10\%$.

All three of the above states are often linked to the closest approach of the disc to the compact

object.

The Soft State

In the thermally dominated soft state most of the X-ray luminosity is presumed to come from the disc, the contribution from a non-thermal power law component in the energy spectra is generally very low but is usually observed (McClintock & Remillard, 2006a,b; Belloni, 2010a; Done, 2010). A very low level of power is observed within the PSD, it can usually be described by the bending power law model described above, with a break in the 1-10 Hz frequency band (a number of examples are shown in McClintock & Remillard, 2006a). QPOs are typically not observed although sometimes very weak incoherent type "A" noise is visible (McClintock & Remillard, 2006b). Radio emission is either undetected or weak and optically thin, suggesting that it is more likely to be remnant emission following the flares observed during the transition to the SIMS (Fender & Kuulkers, 2001; Brocksopp et al., 2002; Fender et al., 2009; Gallo, 2010).

The low levels of variability ($<$ 3 % fractional rms) observed in this state were originally thought to be caused by the dominance of the disc, if most of the variability was originating from the non-thermal corona then as the disc encroaches the power is reduced (see many reviews including McClintock & Remillard, 2006a). This is supported by the fact that as the power spectrum transitions from the hard state to the HIMS, the hard and soft bands initially show similar amounts of variability. Sometimes the soft band is observed to dominate, but by the HIMS the hard energy band is noticeably more variable. This energy dependence is particularly clear in the QPO (Gierliński & Zdziarski, 2005). Recent work using observations taken with *XMM-Newton* has suggested that the disc does in fact vary. More power is observed at low frequencies in soft energies (below the energy range of *RXTE*) than in the higher energy band (Wilkinson & Uttley, 2009), indicating that on longer timescales –most likely to be

associated with the disc, the variability is primarily originating from the thermal power spectral component. More work needs to be done to establish the exact energy dependence of power spectral features but the standard solution that the thermal disc emission is less variable is overly simplistic and the true origins of the variability are more complex than first thought.

The source flux decays gradually in the soft state before the spectrum begins to harden again, the jet turns back on and the source transitions into the hard state and then finally back into quiescence. The jet does not seem to switch on at the same hardness ratio at which it turned off, so the jet line on the HID is not vertical and the exact cause of its recovery is not yet clear (Fender et al., 2009). Better radio monitoring over the course of many outbursts so that many observations of the jet reactivating can be collected is needed before this can be explained (Fender et al., 2009).

1.4 Ultraluminous X-ray Sources

Ultraluminous X-ray sources (ULXs) are extragalactic point-like sources with luminosities greater than 10^{39} erg s^{-1}, they were initially identified by the *Einstein* mission (Fabbiano, 1989). Early studies of short term variability indicated that they were likely to be accreting compact objects (Okada et al., 1998). They appeared unusual as their luminosities indicate that they contain objects with masses > 10 $M_{\odot}$, assuming they are accreting below the Eddington limit, but are located outside the nucleus of their host galaxies (Fabbiano, 1995). Large numbers of these sources have now been identified in various galaxies (Colbert & Mushotzky, 1999; Roberts & Warwick, 2000; Colbert & Ptak, 2002; Liu & Bregman, 2005a; Winter et al., 2006) suggesting that they are a relatively common phenomena, Ptak & Colbert (2004) suggested that up to ~ 12 % of galaxies contain at least one ULX and this number is now thought to be as high as ~ 20 % (Miller et al., 2004; Roberts, 2007). As a mass function for any ULX system is yet to be derived, there has been no clear determination of their mass. Even though

there are now many observations of these objects, including long observations of the brightest sources with powerful X-ray telescopes (*XMM-Newton*, *Chandra* and *Suzaku*) their exact nature is still not fully understood – are they the intermediate mass black holes ($100 - 1000\ M_{\odot}$) suggested from their high luminosities? Or stellar mass black holes ($< 100\ M_{\odot}$) undergoing super-Eddington accretion?

1.4.1 Populations, Locations and Environment

Population studies of ULXs have indicated that they are strongly linked to regions of star formation within galaxies (Fabbiano, 1995; Fabbiano et al., 2001; Humphrey et al., 2003; Swartz et al., 2004; Liu & Bregman, 2005a). Similar correlations have been observed between star forming regions and HMXBs (see e.g. Grimm et al., 2003; Fabbiano, 2006; Mineo et al., 2010). The X-ray luminosity function (the distribution of inferred luminosities of the detected point-like sources) for these galaxies is seen to break above $\sim 10^{39}$ erg s^{-1}, with the number of detected sources above this point consistent with contribution from the background (Irwin et al., 2004). The environment surrounding the ULX is also important: low metallicity environments could allow for the formation of massive metal poor stars (Pakull & Mirioni, 2002; Soria et al., 2005; Swartz et al., 2008). These massive stars ($< 40\ M_{\odot}$) are less affected by the effects of stellar winds and can therefore form more massive black holes ($25 - 80\ M_{\odot}$). These objects would require a massive companion to power them as ULXs (Patruno et al., 2005), but could explain the link in the X-ray luminosity function from HMXBs to ULXs and the connection to star forming regions (see e.g. Zampieri & Roberts, 2009; Mapelli et al., 2009, 2010). As metallicity differs within the galactic environment direct studies of the area immediately surrounding the ULX are necessary. Ripamonti et al. (2010) have attempted to establish the metallicity in the region surrounding NGC 1313 X-2 which has an established optical counterpart, but find that it cannot be well constrained until the effects of X-ray photoionisation on the nebula are better understood.

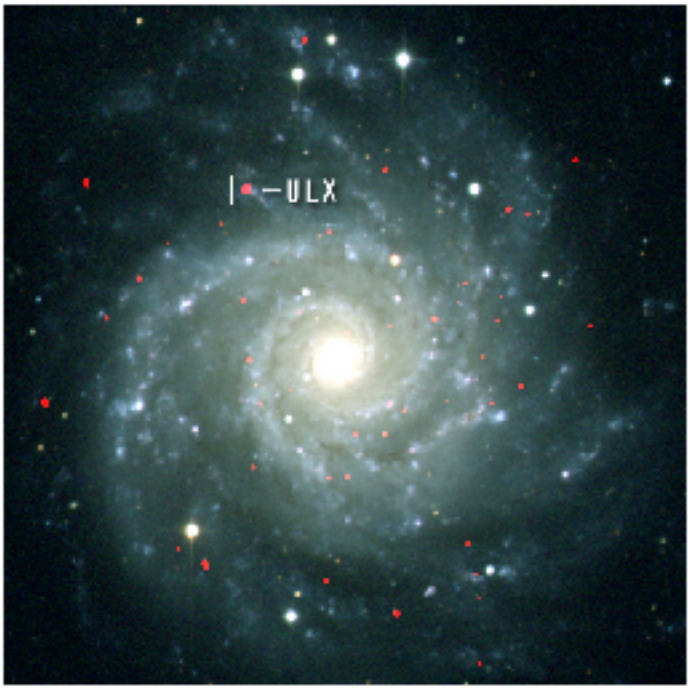

Figure 1.11: X-ray image *(red)* of M74 taken by *Chandra* and overlayed with observations in the optical. The ULX is clearly observed outside the galactic nucleus. Taken from `http://chandra.harvard.edu/photo/2005/m74/`

1.4.2 Spectral studies and states

As these objects appear to contain compact objects, presumably black holes, the first energy spectral studies relied upon there being some correlation between the observations of ULXs and the spectra observed from galactic black hole X-ray binaries. Miller et al. (2003) found that for both of the ULX sources in NGC 1313, high quality spectra taken with *XMM-Newton* were fitted best by a multicoloured disc + power law model commonly used to fit energy spectra from BHBs. In both of these sources the thermal component suggested a disc temperature lower than those indicated from fits to black hole binaries (~ 150 eV rather than $\sim$ 1 keV). As the peak disc temperature decreases as the mass increases the mass must be larger than the Galactic binary sources (Frank et al., 2002). Miller et al. (2003) suggested that the minimum masses of these objects were likely to be $\sim 10^2\ M_\odot$.

Systematic studies of the highest quality spectra from a number of ULXs have since been carried out. Stobbart et al. (2006) found that for a sample of observations from different ULXs taken with *XMM-Newton* simple models (i.e. just a multicoloured disc or power law) would not provide an acceptable fit and that two component models were more statistically acceptable. But they also found evidence for curvature in the energy spectra above ~ 2 keV in around two thirds of the spectra in their sample, suggesting inconsistencies with a power law at high energies. They found that the most effective model consisted of a disc with an optically thick Compton scattering component, indicating the presence of an optically thick corona. This appeared to be consistent with models of BHBs accreting at high rates such as that suggested by Done & Kubota (2006). The high energy turnover was observed in all bar one of the sample of 12 long observations of ULXs analysed by Gladstone et al. (2009), where Comptonised models of an optically thick corona were favoured in 10 out of 12 cases. As this model suggests differences from the optically thin corona observed in states from BHBs, the authors suggest that these sources exist in a previously unseen "ultraluminous" state. It is, however, also possible to fit this turnover with a reflected disc model (Caballero-García & Fabian, 2010) within the *XMM-Newton* band pass. Walton et al. (2010) point out that the observational energy range needs to be extended above 10 keV before the different effects of these two models may be seen in the spectra.

Thus it now appears that the states observed in ULXs do not correlate well with those seen in galactic black hole binaries, the high accretion rates presumably present alter the state of the source and thus the shape of the energy spectra. Gladstone et al. (2009) suggest that they observe evolution in the energy spectra between different sources. Beginning at something similar to a typical soft state where a strong disc component seems to be present, the secondary component gradually appears and becomes clearer at higher energies, producing something similar to the very high HIMS or anomalous soft state. Eventually the spectra is best described by a cool disc-like component combined with the Comptonisation component. However, evidence of spectral evolution over time from a single source is needed to fully es-

tablish any form of evolutionary sequence. Without the form of monitoring afforded to BHBs by their high fluxes, a good understanding of ULX evolution is difficult.

Some energy spectral changes have been observed over individual observations, Feng & Kaaret (2009) observe a low energy component in NGC 5204 X-1 which appears to drive the flux changes whilst the high energy component remains approximately constant, a similar affect was observed in NGC 5408 X-1 (Strohmayer & Mushotzky, 2009). Evidence for alterations in the energy spectra of Ho IX X-1, IC 342 X-1 and X-2 and Ho II X-1 have also been observed (see Soria, 2010; Belloni, 2010a, for a review of observations of these sources). Consistent monitoring is now possible using *Swift* which has revealed strong long term variability in Ho II X-1, Ho IX X-1, NGC 5408 X-1 and NGC 4395 X-2 (Kaaret & Feng, 2009; Grisé et al., 2010). Large flux changes have been revealed in these monitoring programmes displaying strong long term variability, although the changes in emission are not linked to alteration of components in the energy spectra and the spectral shapes remain remarkably consistent. Ho II X-1 was observed with *Swift* 3 years before the monitoring campaign began and spectral differences were observed between these observations and the later ones (Grisé et al., 2010). In short, there is not yet a consistent picture of spectral evolution for ULXs, but monitoring with both *Swift*and future missions will hopefully reveal clear evidence of spectral changes and the timescales over which they occur.

1.4.3 Timing characteristics

The other avenue to explore when comparing BHBs and ULXs is through their short term variability, this is discussed in detail in Chapter 3 but I provide a brief review of the main results up to this point here. Relationships between power spectral components and accretion rate or black hole mass are well known, McHardy et al. (2006) showed that the break frequencies for the high frequency break in AGN and BHBs display a correlation dependent on the mass

of the black hole and its accretion rate $T_{Break} \propto M_{BH}^{1.12}\dot{m}_{Edd}^{-0.98}$ when BHBs are in the soft state (assuming the power spectra are modelled using a broken power law). Körding et al. (2007) have altered and extended the analysis from McHardy et al. (2006) to BHBs in the hard state using the Lorentzian fitting method, forming a relationship between accretion, BH mass and the Lorentzian relating to the high frequency break. As ULXs are distant and therefore faint there is only a limited frequency range in which variability is observed before it is hidden in the Poisson noise, decomposition into Lorentzians in a similar manner to the analyses performed on BHB observations is not possible, for this reason the broad band noise is typically fitted using a power law or broken power law model. From these relations breaks in the power spectra of intermediate mass black holes are expected in the 0.001 - 0.1 Hz frequency range at which *XMM-Newton* is most sensitive (see e.g. Strohmayer et al., 2007). A break in the PSDs of ULXs NGC 5408 X-1 and M82 X-1, from a flat power law to -1 dependence, similar to the low frequency break seen in the hard state of BHBs, has been identified below QPOs by Soria et al. (2004) and Dewangan et al. (2006b); Mucciarelli et al. (2006) respectively.

QPOs have been detected in four ULXs, M82 X-1 (X41.4+60), NGC 5408 X-1, M82 X42.3+59 and NGC 6946 X-1 indicating that the systems may have similar variability properties to BHBs (Strohmayer & Mushotzky, 2003; Dewangan et al., 2006c; Strohmayer et al., 2007; Strohmayer & Mushotzky, 2009; Feng et al., 2010; Rao et al., 2010a). The QPOs in both M82 X-1 and NGC 5408 X-1 have been observed with *XMM-Newton* on more than one occasion, in the case of NGC 5408 X-1 the observations were taken two years apart and the QPO had shifted from 20 mHz down by 10 mHz, it appears to also have a harmonic component. In M82 X-1 the observations were separated by three years and the QPO shifted from 54 mHz to 114 mHz Dewangan et al. (2006c). Work by Mucciarelli et al. (2007) suggest that the QPO is variable over the course of an observation shifting down by $\sim$ 25 mHz and *RXTE* observations indicate that it varies between 50-166 mHz. The QPOs in M82 X42.3+59 and NGC 6946 X-1 are detected at 3-4 mHz and 8.5 mHz respectively. The QPO in M82 X42.3+59 also appears to be luminosity dependent – it is only visible when the source is above 10^{40} erg s^{-1}

(Feng et al., 2010). In NGC 5408 X-1 a break is detected below the QPO with some significance, Strohmayer & Mushotzky (2009) suggest this provides evidence that the BH is of an intermediate mass between 2000 - 5000 $M_{\odot}$. However Middleton et al. (2010) argue that the QPO is mis-identified and in fact is representative of the ultra low frequency QPOs observed in the galactic BHB GRS 1915+105. From this they suggest that the mass is likely to be < 100 $M_{\odot}$. The variability in these sources is observed to be energy dependent, it appears to be consistently higher in the 2-10 keV hard band than the 0.3-2 keV soft, similar behaviour to that observed in BHBs in the HIMS (Strohmayer et al., 2007; Strohmayer & Mushotzky, 2009; Feng et al., 2010; Rao et al., 2010b).

In contrast to the strong timing signatures observed in these ULXs, studies of other sources have shown that some do not display any evidence of strong short term variability, this lack of variability is not observed from BHBs (Feng & Kaaret, 2005; Goad et al., 2006; Roberts, 2007).

Chapter 2

Instrumentation and Data Analysis

2.1 Instruments

2.1.1 Rossi X-ray timing explorer (*RXTE*)

The Rossi X-ray timing explorer (*RXTE*) was launched at the end of 1995 into a low earth orbit. One of its primary goals was to take observations of objects with high temporal resolution. It is equipped with three main instruments: the All Sky Monitor (ASM), High Energy X-ray Timing Experiment (HEXTE) and the Proportional Counter Array (PCA). A diagram of *RXTE* is shown in figure 2.1. Although it is not an imaging mission like *Chandra* and *XMM-Newton*, the combination of high daily sky coverage, relatively wide spectral range and flexible scheduling allows for good monitoring and long observations of bright transient sources. Although this work has mainly made use of the PCA, the other instruments are described in brief, before a more thorough introduction to the PCA is given.

The ASM consists of 3 Scanning Shadow Cameras (SSCs) with a spatial resolution of 3' × 15'. The detectors are position sensitive Xenon proportional counters which, together with the

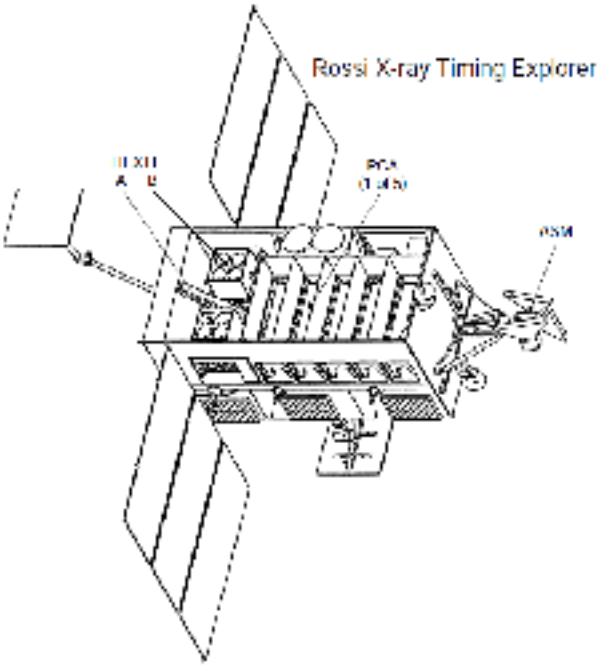

Figure 2.1: Diagram of *RXTE* indicating the fields of view for the three instruments, taken from Rothschild et al. (1998)

coded mask, allow for source placement within the 6° × 90° field of view. The cameras are rotated, meaning ~80% of the sky can be monitored over the course of one orbit (90 mins) in the 1.5-12 keV band. It is this monitoring capability which makes *RXTE* particularly useful for the study of transient sources, they can be identified as they go into outburst and this has allowed for the full analysis sources at a range of different flux levels.

HEXTE has two clusters of scintillation detectors (A and B) covering the energy range 15-250 keV which are co-alligned with the PCA. It has a 1° FWHM field of view and a maximum time resolution of 7.6 μs. On-off source rocking allowed the background to be continuously measured during the course of an observation, this rocking ability has now been lost in the two detectors and cluster A is now fixed in the on-source position whilst B is off-source.

The PCA is an array of 5 Xenon filled proportional counter units (PCUs), each with five collimator modules giving a field of view of 1° FWHM. A sketch of a PCU is given in figure

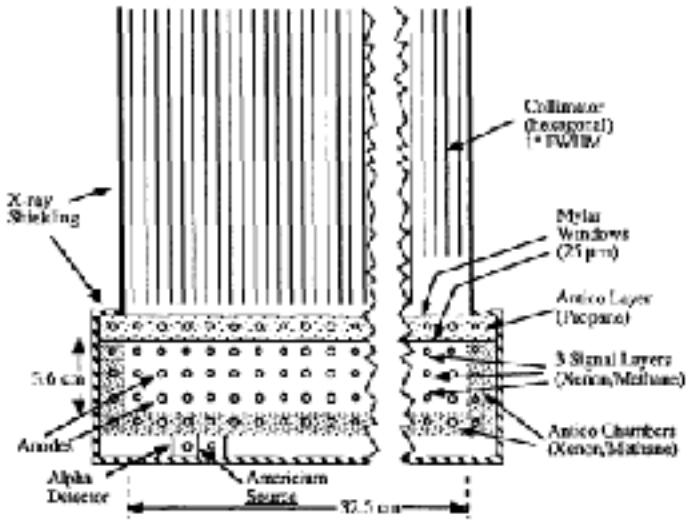

Figure 2.2: Diagram of the structure of a PCU from the PCA on *RXTE* taken from Bradt et al. (1990)

2.2 They each have an effective area of ~1400 cm^2, and the total collecting area is ~6500 cm^2. The detectors are sensitive in the 2-60 keV energy range, and the maximum possible time resolution is 1 μs. As neither HEXTE or the PCA have position sensitive detectors the background rates are quite high (typically ~ 7 ct s^{-1} PCU^{-1} in the 2-20 keV range). The PCUs are either numbered from 1-5 or from 0-4, for consistency in this work they will be referred to by the latter identifiers.

The PCA does not take a measurement of the background so models are used to estimate it (see Jahoda et al., 2006). Since launch the detectors have been affected by various issues limiting the amount of on-time they are now used for. PCUs 3 and 4 are regularly 'rested' as occasional break-downs have been noted, probably caused by the discharge of sparks within the Xenon chamber. On the 12th May 2000 PCU 0 lost its propane layer (see Figure 2.2) due to a micro-meteorite hit, this same problem then also hit PCU 1 on the 25th December 2006. For this reason few observations make use of all five PCUs, they often have various combinations of detectors on instead and PCU 2 is now the only one to be used constantly. This means that count rates are typically normalised to one PCU to allow for consistency between individual

observations.

Data taken by the PCA can be compressed into various different modes dependent on the requirements of the observer. Observations can be taken in seven data modes running in parallel, these include two standard data modes (Standard 1 and Standard 2) which observations are always taken in. The different modes then available to be chosen by the observer allow for focus on particular properties. 'Science array data' is collected into histograms over specific time intervals, this includes 'Binned' modes where the counts in one time bin are measured with a wide range of possible configurations for both time and energy binning and 'Single Bit' modes where each clock tick and event in only one (typically wide) energy band is recorded by *RXTE* and then converted into a histogram so it looks similar to 'Binned' modes. In contrast 'Event' mode data records the arrival time of each 'good' X-ray event individually, again with various time resolutions and energy ranges. These data modes, high time resolution and high throughput make *RXTE* ideal for observing bright X-ray transient systems within our own Galaxy.

2.1.2 *XMM-Newton*

XMM-Newton was launched in December 1999 into a highly elliptical orbit (with a 2 day period), the largest scientific satellite to be launched by the European Space Agency (ESA) up to that point (Jansen et al., 2001). It has two main X-ray instruments, the EPIC cameras consisting of an EPIC-pn (European Photon Imaging) camera and two EPIC-MOS imaging detectors, and also two Reflection Grating Spectrometers (RGS). The three X-ray telescopes each have large area mirror modules, consisting of 58 nested grazing incidence mirrors with a focal length of 7.5 m. The mirrors each have a paraboloid-hyperboloid surface with grazing angles ranging from 17' to 42'. Shallow incidence angles allow for high energy photons to be reflected towards a focal point. *XMM-Newton* also has an optical/UV monitor telescope

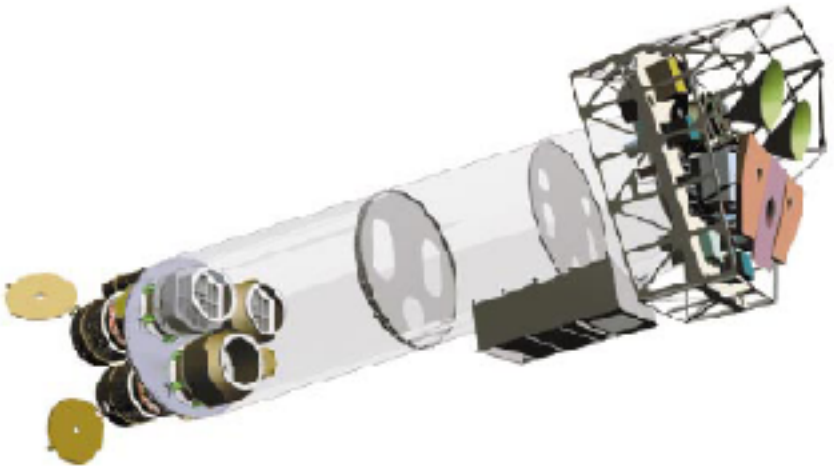

Figure 2.3: Diagram of *XMM-Newton* , the mirror modules are to the left and the instrument platform to the right. Taken from Jansen et al. (2001)

(XMM-OM) providing simultaneous observations of X-ray targets in the waveband λ = 170 - 650 nm (Mason et al., 2001). The RGS gratings on board *XMM-Newton* are positioned behind two of the mirror modules (see Fig. 2.3), they intercept around half of the light from the telescope. Each array operates in the 0.33-2.5 keV band and with a resolving power of ~150-800 (den Herder et al., 2001). This work has mainly made use of the EPIC-pn and data from the EPIC-MOS is discussed, therefore a more detailed description of these detectors is now given.

The EPIC cameras allow for high quality imaging across a ~30' field of view in the 0.2-15 keV energy band. There are two sets of MOS CCDs behind two of the mirror modules and one pn camera behind the other. They have reasonable spatial resolution of ~6" at FWHM.

The MOS cameras comprise of seven CCDs with 600×600 pixels, each 40 microns square. In this way each pixel covers 1.1×1.1 arcsecs on the sky. These cameras share their mirror module with the RGS and as such 44% of the light from the mirrors reach the CCDs. The central CCD is positioned at the focal point for the telescope and the surrounding ones are then stepped in order to correct for off-axis effects. The two MOS cameras are arranged in

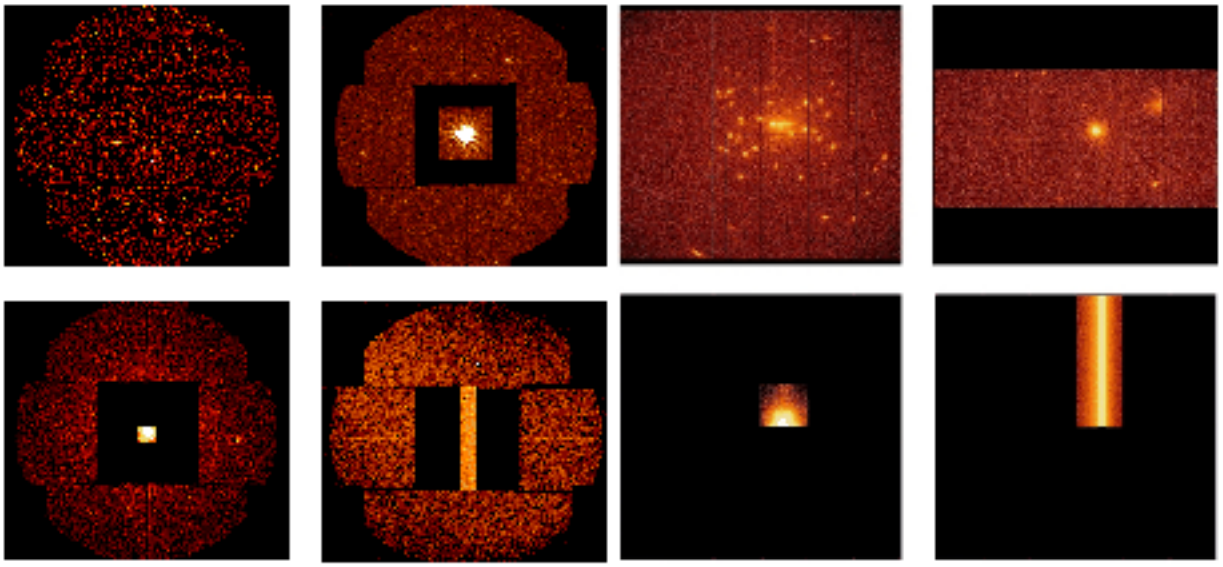

Figure 2.4: The operational portions of the CCDs in each mode for the EPIC-MOS cameras (*left*) and EPIC-pn (*right*). Clockwise the modes are full-frame, large window, small window and timing on each set of four. Images from "*The XMM-Newton Users Handbook*" available at `http://xmm.esa.int/external/xmm_user_support/documentation/uhb`

such a way that the gaps between chips in the outer CCDs on one camera are covered by the second camera, the central CCDs then match up exactly but the pn camera is arranged to cover the gaps around this chip allowing for the whole field of view to be covered. The basic read-out time for the MOS camera is 2.6s although different modes allow for higher time resolution (Turner et al., 2001).

The pn camera has 12 individual CCDs on a single wafer, each of which can be individually operated. The pixels are each 150 microns square corresponding to 4.1", each chip containing 200×64 pixels. As at the centre of the pn camera there is a gap between the chips, the camera is positioned so that the focal point is off-center. Chip gaps cannot be corrected for when using data from the pn and this fact must be recognised during data processing, however approximately 97% of the field of view from the telescope is covered by the camera. The basic time resolution of the pn camera is 73.4 ms, but again this can be raised through the use of different modes (Strüder et al., 2001).

The modes allowing for higher time resolution differ slightly depending on the camera, but in general include large and small window modes and timing modes. In window modes only a small area of the CCD is selected and read accurately so less time is needed to correctly measure the charge on the CCD. Reducing this processing time allows events to be read quicker and therefore gives less time for the CCD to 'pile-up' or saturate when observing bright sources at high count rates. For the MOS cameras this only applies to the central CCD and the outer chips continue functioning normally. Large window mode uses the central 300×300 pixels and gives a 0.9s resolution, in small window mode this is reduced further to 100×100 and 0.3s respectively (Turner et al., 2001). For the pn large window mode uses the inner half of each CCD, the image is transferred to the outer half for rapid read-out, giving a time resolution of 47.7 ms. In small window mode only a 63×64 pixel region is used around the focal point and the time resolution is reduced again to 5.7 ms (Strüder et al., 2001). Timing mode is slightly different but works even more rapidly, for the MOS cameras 100 rows of 100 pixels are compressed into one, so the flux is measured at resolutions of 1.75 ms per row. In the pn the 10×1 rows for each time slice are shifted up the chip and only read out after 9 transfers, this gives a time resolution of 30 μs. The use of timing mode requires a loss of positional information in one direction of the chip, this is less important for the MOS camera where the rotation of one camera against the other allows for the loss of position in one camera to be regained in the other. The areas used in the cameras for these different modes are shown in Figure 2.4.

There are three main causes for the observed background in *XMM-Newton* observations. Soft protons, possibly from some form of interaction in the Earth's magnetosphere, are scattered through the mirror modules creating strong flares which may dominate an observation, these periods of flaring need to be removed during processing. There is also higher energy background from cosmic rays - the charged particle background of space. These high energy events produce particular signature energy distributions and patterns on the chip, which are then rejected as bad events. Galactic diffuse emission and the cosmic X-ray background

also contribute to the total measured level. The CCDs on *XMM-Newton* are also sensitive to photons in other energy bands (IR, visible and UV). In order to reduce detections at these energies the cameras come equipped with thin, medium and thick filters which can be used as neccessary depending on the science required from an observation.

2.2 Power Spectra

The power spectral density (PSD) is a tool widely used in a variety of different fields. Plotting it provides a visual representation of the statistical properties of a time series i.e. the power density (amplitude squared) as a function of the Fourier frequency ($1/timebin$). Strictly periodic signals (such as sinusoids) appear in the power spectrum as discrete lines, all power is concentrated at one particular frequency. In contrast 'noise' (or stochastic) processes show continuous spectra with power over a broad range of frequencies. Flicker or red noise are common in nature and show power spectra of the form $f^{-\alpha}$ (where $\alpha > 0$) over a broad range of frequencies (see Press, 1978). As such the power spectrum contains information about the characteristic frequencies (timescales) of a process.

The PSD is usually estimated from the periodogram, defined as the modulus squared amplitudes of the Fourier transformed time series, and can be normalised in a number of different ways – van der Klis (1989a) summarises the use of PSDs in time series analysis with a focus on X-ray timing. Where continuous data is not available (a rare occurence for modern astronomy) the power spectra is best estimated from data binned in equidistant time steps. The discrete fourier transform is therefore defined as

$$X_j = \sum_{k=0}^{N-1} x_k \exp^{2\pi i jk/N} \quad j = -(N/2), ..., (N/2) - 1 \tag{2.1}$$

In this case x_k is the count rate in bin k of the time series where N is the total number of bins. The highest resulting frequency is referred to as the Nyquist frequency and is defined as $\nu_{N/2} = 1/2\delta t$ if δt is the time bin size. From this the periodogram is defined as

$$P_j = A|X_j|^2 \tag{2.2}$$

A is the normalisation constant applied, this can be chosen according to the task required. Three in particular are commonly used, the Leahy, fractional or absolute normalisations. Leahy normalisation, originally suggested in Leahy et al. (1983), is advantageous for sources with sharp signals but little broad-band noise in the power spectra. The power is normalised as –

$$P_j = \frac{2\delta t}{n\langle x\rangle}|X_j|^2 \tag{2.3}$$

where $|X_j|$ is the fourier amplitude, n is the number of points in the segment, $< x >$ is the mean count rate and δt is the time resolution of the original time series. This has a Poisson noise level of $N_p = 2$ distributed as χ^2 with 2 dof. So signals are easier to detect above the noise level as its properties are well understood (see e.g. van der Klis, 1989a).

The second normalisation method is probably the most commonly seen in recent works. Normalising to the fractional rms is particularly useful when comparing power spectra from different sources or epochs as the dependence on count rate is removed. In the notation used here it would be described by –

$$P_j = \frac{2\delta t}{n\langle x\rangle^2}|X_j|^2 \tag{2.4}$$

The noise level is then $N_p = \frac{2}{<x>}$ (see Miyamoto & Kitamoto, 1989; Miyamoto et al., 1991). The integrated area under the power spectra is then the fractional rms within the frequency limits, this value is often presented as a percentage.

A power spectrum measured in absolute normalisation differs in that the flux dependence is retained. The power can be described by -

$$P_j = \frac{2\delta t}{n}|X_j|^2 \tag{2.5}$$

In this normalisation the total variance is given by the area underneath the power spectra – the integration of the function over positive frequencies. The equivalent Poisson noise level in this case is then $N_p = 2 < x >$. Allowing the true variance to be measured means that alterations in the amount of variation with source count rate are clearly visible. This normalisation is used extensively within this thesis (see e.g. Uttley & McHardy, 2001; Vaughan et al., 2003a; Uttley et al., 2005, and references therein).

The periodogram of a random (stochastic) process is inherently noisy (and is known as an 'inconsistent' estimator of the true power spectrum), in fact the measured values of the power are distributed around the 'true' value according to a χ^2 distribution with 2 degrees of freedom. In order to estimate the real value of the power, binning gives a 'consistent' power spectrum estimator. This can be performed in two separate ways. In the first before the Fourier transform time series are split into a number of segments, and a periodogram computed for each, these can then be averaged together to find the mean power spectra over the whole observation, or gathered into different groups according to variables such as the mean flux in the orginal time series segment – this grouping is used throughout this work. Once an average power spectrum is measured it can also been binned in frequency, further reducing the errors on each point.

Both forms of binning reduce either the frequency bandpass or resolution of the data: in the

former case the lowest frequency becomes limited by the segment size, in the latter frequency resolution is lost. If the power spectra is flat then the errors on each power spectral point are given by $\delta\langle P\rangle = \langle P\rangle / \sqrt{MW}$ where M is the number of time series segments used, W is the number of points in each frequency bin and $\langle P\rangle$ is the binned power value. From this you can see that the greater the number of points in a bin, the smaller the variance on the estimator.

Chapter 3

Systematic Study of Variability in a Sample of ULXs

3.1 Introduction

This Chapter describes a power spectrum analysis of the time series obtained from 19 *XMM-Newton* observations of ULXs. Several of these observations have been analysed and discussed separately elsewhere (see section 2), but this paper presents the first uniform analysis and presentation of the power spectra from a reasonable-sized sample of good quality ULX observations (i.e. observations with good exposure time of sources with high X-ray fluxes). As noted above, some ULX observations show no evidence for rapid X-ray variability, but in almost all published studies (e.g. Feng & Kaaret, 2005) it is not clear whether the lack of detected variations is due to insufficient data or an intrinsically low variability amplitude (by comparison with well studied BHBs and AGN, and also the variable ULXs). Indeed, the careful analysis of Ho II X-1 by Goad et al. (2006) showed the ULX to be intrinsically under-variable. This raises some interesting questions, but it is not clear whether the lack of

strong variability is common in ULXs: in all other previous studies where no variability was detected, there was no attempt to constrain the amplitude of intrinsic variation allowed. In the present study we analysed the power spectra of all 19 observations, and where no variability was detected, we followed the approach used by Goad et al. (2006) to constrain the power spectrum. This allowed us to compare the variability properties of all the ULXs, whether variability could be detected or not, in a way not possible using the results of previously published studies.

The rest of this Chapter is organised as follows. Section 2 describes our sample selection criteria and search process. In Section 3 we discuss the basic data reduction techniques used and methods of temporal analysis. Section 4 explains our results in some detail including investigations into the upper limits of variation hidden within the power spectra. Finally Section 5 gives a brief discussion and conclusion.

3.2 Sample Selection

We have performed a search for bright ULXs with a flux previously observed to be greater than 0.5×10^{-12} erg s^{-1}. A sample was formed through use of sources previously identified in Stobbart et al. (2006), searching the *ROSAT* catalogues of Liu & Bregman (2005b) and Liu & Mirabel (2005) and by carrying out an archival study of papers studying ULXs using the ADS database (ADS[1]). A search was then made for long observations (> 25 ks) of regions including these sources available by February 2008 in the *XMM − Newton* public data archive (XSA[2]) . The final sample consists of 19 observations from 16 sources with the potential to provide useful timing data (see Table 3.1).

As mentioned above, several of these observations have been discussed elsewhere in the lit-

[1] http://ads.harvard.edu/
[2] http://xmm.esac.esa.int/xsa

erature, and here we briefly summarise these reports. The observations of NGC 1313 X-1 and X-2, NGC 5204 X-1, NGC 4945 X-2, NGC 4861 ULX and NGC 253 PSX-2 have no published discussion of their short-term variability.

The observations of NGC 55 ULX were known to display interesting variability (Stobbart et al., 2004), but this has not previously been analysed in detail. No variability was detected by Feng & Kaaret (2005) in the observations of NGC 4395 X-1, NGC 3628 X-1, M83 ULX and NGC 2403 X-1. Barnard et al. (2007) detected no variability in NGC 4559 X-1 (revising the previous report by Cropper et al., 2004). Only the remaining five observations have detailed power spectral analyses published to date. The PSDs from the two observations of M82 X-1 have been published in Strohmayer & Mushotzky (2003) and Dewangan et al. (2006b) respectively: these show a strong QPO and a break in the PSD. A similar QPO and spectral break has also been detected in the observation of NGC 5408 X-1 (Strohmayer et al., 2007). Dewangan et al. (2006a) claimed a modestly significant QPO in the power spectrum of the observation Ho IX X-1. Finally, as mentioned above, Goad et al. (2006) presented a detailed analysis of the lack of variability present in the long observation of Ho II X-1.

Source name	Alternate Names	Obs. Id.	RA (J2000)	Dec. (J2000)	Duration (ks)	Good Time (ks)	L_x 10^{39} erg/s
(1)	(2)	(3)	(4)	(5)	(6)	(7)	(8)
NGC 55 ULX[a]		0028740201	00:15:28.9	-39 13 19.1[a]	34.0	30.3	1.21
		0028740101			28.3	26.1	1.18
NGC 253 PSX-2[b]	NGC 253 XMM1[j]	0125960101	00:47:32.9	-25 17 50.3[j]	38.9	31.6	0.25
NGC 1313 X-1[c]	NGC 1313 ULX1[j], IXO 7[k]	0405090101	03:18:19.8	-66 29 09.6[j]	121.2	85.8	4.25
NGC 1313 X-2[c]	NGC 1313 ULX3[j], IXO 8[k]	0405090101	03:18:22.0	-66 36 04.3[j]	121.2	85.8	5.12
NGC 2403 X-1[d]		0164560901[r]	07:36:25.9	+65 35 38.9[j]	77.5	58.3	2.62
Holmberg II X-1[e]	PGC 23324 ULX1[j], IXO 31[k]	0200470101[q]	08:19:29.9	+70 42 18.6[j]	79.5	45.3	16.6
M82 X-1[f]	Source 7[m]	0112290201[i]	09:55:50.2	+69 40 47.0[m]	27.3	27.4	21.0
		0206080101[u]			91.0	57.5	20.5
Holmberg IX X-1[g]	M81 X-9[n], PGC 28757 ULX1[j], IXO 34[k]	0200980101[t]	09:57:54.1	+69 03 47.3[j]	111.8	58.7	8.67
NGC 3628 X-1[d]	IXO 39[k]	0110980101[r]	11:20:15.8	+13 35 13.6[a]	50.3	46.1	4.14
NGC 4395 X-1[d]	NGC 4395 ULX1[j], IXO 53[k]	0142830101[r]	12:26:01.5	+33 31 34.7[j]	106.1	78.6	0.21
NGC 4559 X-1[d]	NGC 4559 ULX2[j]; ULX-7[p], IXO 65[k]	0152170501[s,p]	12:35:51.6	+27 56 01.7[j]	40.2	33.3	9.01
NGC 4861 ULX[a]	NGC 4861 ULX1[j], IXO 73[k]	0141150101	12:59:02.0	+34 51 12.0[j]	15.4	13.8	7.90
NGC 4945 X-2[h]	NGC 4945 XMM1[j]	0204870101	13:05:33.3	-49 27 36.3[j]	62.5	22.0	0.15
NGC 5204 X-1[d]	NGC 5204 ULX1[j], IXO 77[k]	0405690201	13:29:38.6	+58 25 07.5[j]	43.4	28.5	5.27
		0405690501			40.0	15.9	5.00
M83 ULX[a]	NGC 5236 ULX1[j], IXO 82[k]	0110910201[r]	13:37:20.2	-29 53 47.7[j]	27.0	18.9	0.97
NGC 5408 X-1[i]	NGC 5408 ULX1[j]	0302900101[v]	14:03:19.6	-41 22 58.7[o]	130.0	95.7	5.28

Table 3.1: Observation Details. (1) Source Name; (2) alternate names; (3) *XMM − Newton* observation identifier; (4)-(5) Positions from *XMM − Newton* or *Chandra* data; (6) *XMM − Newton* observation length (ks); (7) length of good time with background flares excluded (ks); (8) Observed Luminosity measured from energy spectral fitting (see text). Footnotes indicate references as follows: Column 1-2 footnotes indicate the identification of sources with the given name(s); column 3 footnotes refer to previous power spectral analyses of the observations; column 5 footnotes provide references to source positions. [a]Guainazzi et al. (2000); [b]Roberts & Warwick (2000); [c]Stobbart et al. (2006); [d]Humphrey et al. (2003); [e]Soria et al. (2006); [f]Colbert et al. (1995); [g]Miller et al. (2004); [h]Dewangan et al. (2004); [i]Strohmayer & Mushotzky (2003); [j]Liu & Bregman (2005b); [k]Colbert & Ptak (2002); [l]Winter et al. (2006); [m]Matsumoto et al. (2001); [n]Fabbiano (1989); [o]Kaaret et al. (2003); [p]Cropper et al. (2004) [q]Goad et al. (2006) [r]Feng & Kaaret (2005) [s]Barnard et al. (2007) [t]Dewangan et al. (2006a) [u]Dewangan et al. (2006b) [v]Strohmayer et al. (2007)

3.3 Analysis

Lightcurves and energy spectra were extracted from the EPIC pn camera on *XMM-Newton*. In all observations the camera was operating in full-field mode excepting that of Ho IX X-1 (obs Id. 0200980101) which was taken in large window mode. The MOS cameras were not utilised due to their lower time resolution, making it harder to constrain the Poisson noise level during power spectral analysis. When the data were included they were found to add little to either the results or analysis. The data from each observation was extracted and processed using the *XMM-Newton* SAS version 7.1.0. Data was filtered leaving only events with `PATTERN` $\leq$ `4` and `FLAG==0`. Events were extracted either within the optimised radius of the source, as evaluated by the SAS, or a radius of our own definition if other factors (such as the source sitting close to a chip edge or near another X-ray point source) made this unsuitable. A background light curve was taken from a rectangular region on the same chip and as close to the source as possible.

Lightcurves for the 0.3-10 keV band were extracted with a time resolution of 73.4 ms for all sources except for Ho IX X-1, the lightcurve of which had a time resolution of 96 ms accounting for the different camera operational mode. Most of the ULXs are near the aimpoint of the image and are clearly detected as separate point sources, with a few exceptions. Most sources were therefore extracted from a region centred on the co-ordinates given in Table 3.1. NGC 4395 X-1 is close to the edge of the chip; M82 X-1 and NGC 3628 X-1 are close to the centre of their host galaxies and other bright X-ray sources, causing difficulties in exactly identifying the source whilst excluding all others given the resolution of *XMM-Newton*. For M82 X-1 we followed Strohmayer & Mushotzky (2003) and extracted an 18" region centred on the co-ordinates for the point source identified clearly in *Chandra* observations. Analysis of power spectra taken from regions surrounding the bright ULX in the *XMM-Newton* observations by Feng & Kaaret (2007) has suggested that this is where the QPO originates. NGC 3628 X-1 was extracted in a 23" region centred on the co-ordinates given in Table 3.1. The second ob-

servation of NGC 55 ULX (obs. Id. 0028740101) is off-axis, causing a lower average count rate than observed in the first observation (obs. Id. 0028740201) and so the two observations were treated separately.

In order to remove background flares a light curve was extracted from the entire chip in the $10 - 15$ keV band and then criteria applied to exclude regions where the count rate stayed continuously over three times the mean. Only flares longer than 30s were considered. Any telemetry effects where the count rate dropped to zero for a period longer than 15 s were replaced with the mean count rate in the source file (this had only a small effect on the overall light curve and subsequent temporal analysis). The second half of the light curve from Ho IX X-1 (obs Id. 0200980101) was particularly affected by this. The continuous regions not affected by flaring were defined as good time intervals.

Luminosities were measured through fitting each of the energy spectra with a multicoloured disc + power law model and are included in Table 3.1.

3.3.1 Timing Analysis

In order to estimate the PSD from an observation the available good time was split into at least five segments of equal length. The FFTs from each segment were averaged and the result re-binned in frequency giving a factor 1.1 increase in frequency per bin (i.e binning over $f_i \rightarrow 1.1 f_i$), but ensuring there were at least 20 points in each. This averaging process permits minimum-χ^2 fitting to be used as a maximum likelihood method (van der Klis, 1989a; Papadakis & Lawrence, 1993). The PSD was normalised to the fractional rms squared (van der Klis, 1997). Visual examination revealed no QPOs in addition to those already reported in M82 X-1 (Strohmayer & Mushotzky, 2003) and NGC 5408 X-1 (Strohmayer et al., 2007). Figure 3.-1 shows a selection of eight of the sample of PSDs, these are all plotted with the same segment size for ease of comparison, it must be noted that some of the PSDs used for

the analysis were produced with larger segments and this allows a few more points of data to be visible at low frequencies.

At high frequencies the PSD is expected to be dominated by Poisson noise, random fluctuations in the photon counts even in the absence of intrinsic variability in the source flux. This produces a constant (i.e. flat) additional component in the PSD (van der Klis, 1989a) with an expected noise level (in the absence of detector non-linearities) of approximately $2(S + B)/S^2$ where S is the source count rate and B is the background count rate, calculated from the counts in the good time intervals (Uttley et al., 2002; Vaughan et al., 2003a). In order to determine the Poisson noise level in each observation the high frequency region of the PSD ($\geq$ 0.5 Hz) was fitted with a constant and the normalisation compared to the expected Poisson noise level. Generally these correspond within the $\sim$ 2% errors on the PSD estimate. However for the two brightest sources, Ho II X-1 and M82 X-1, the measured values were $\sim$ 3% below the prediction levels. In a sample of this size an observation is expected to deviate from the expected value, but as these are the two brightest sources these differences may be due to instrumental effects such as event pile-up or dead time (see also Goad et al., 2006).

3.4 Results

The following subsections describe the results of fitting various simple models to the power spectral data.

3.4.1 Variable Sources

In the absence of any intrinsic variability from the source the power spectrum is expected to be constant with frequency resulting from Poisson noise in the photon counting detector.

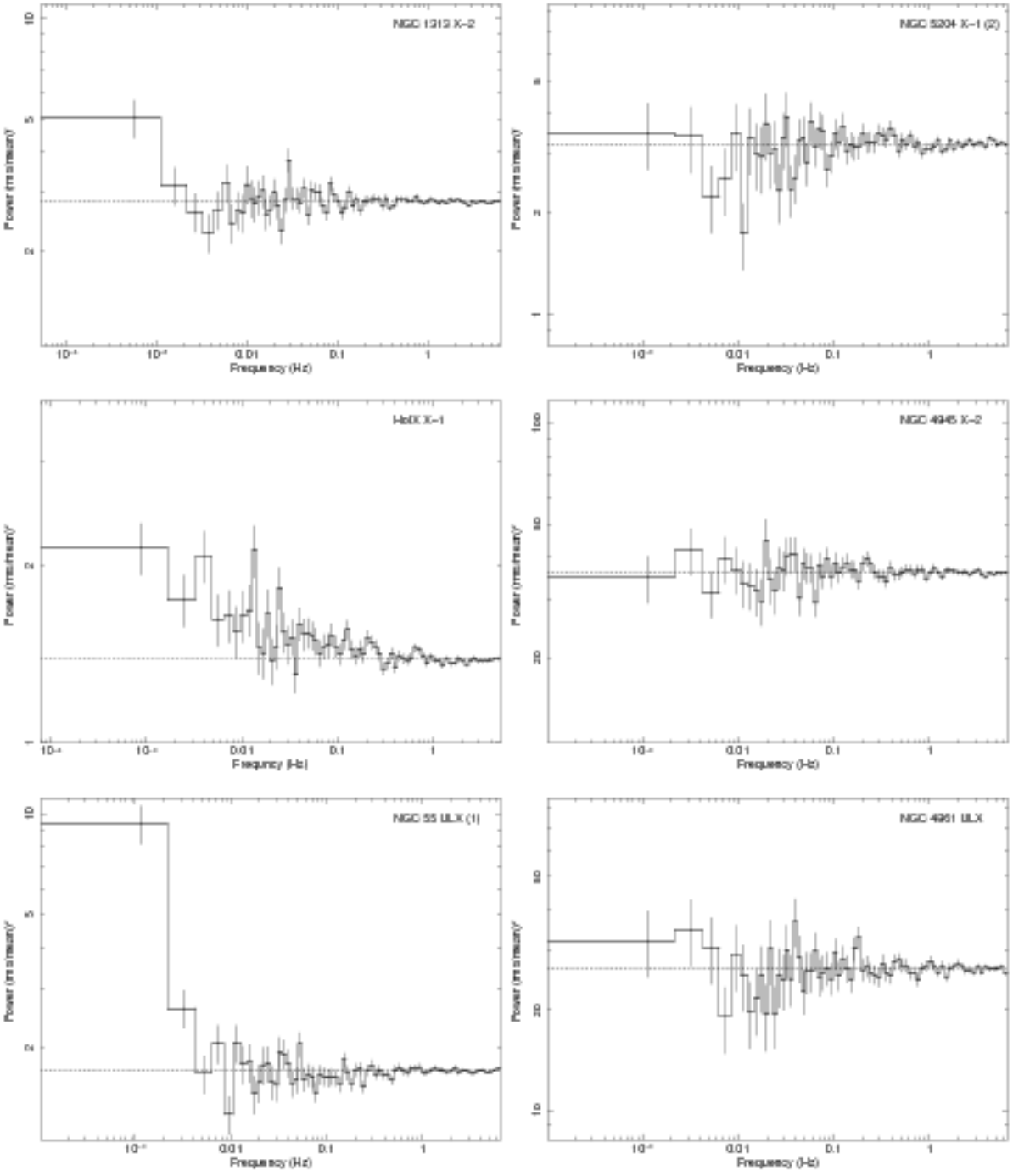
NGC 1313 X-2
NGC 5204 X-1 (2)
Holmberg IX X-1
NGC 4945 X-2
NGC 55 ULX (1)
NGC 4951 ULX
Power (rms/mean)²
Frequency (Hz)

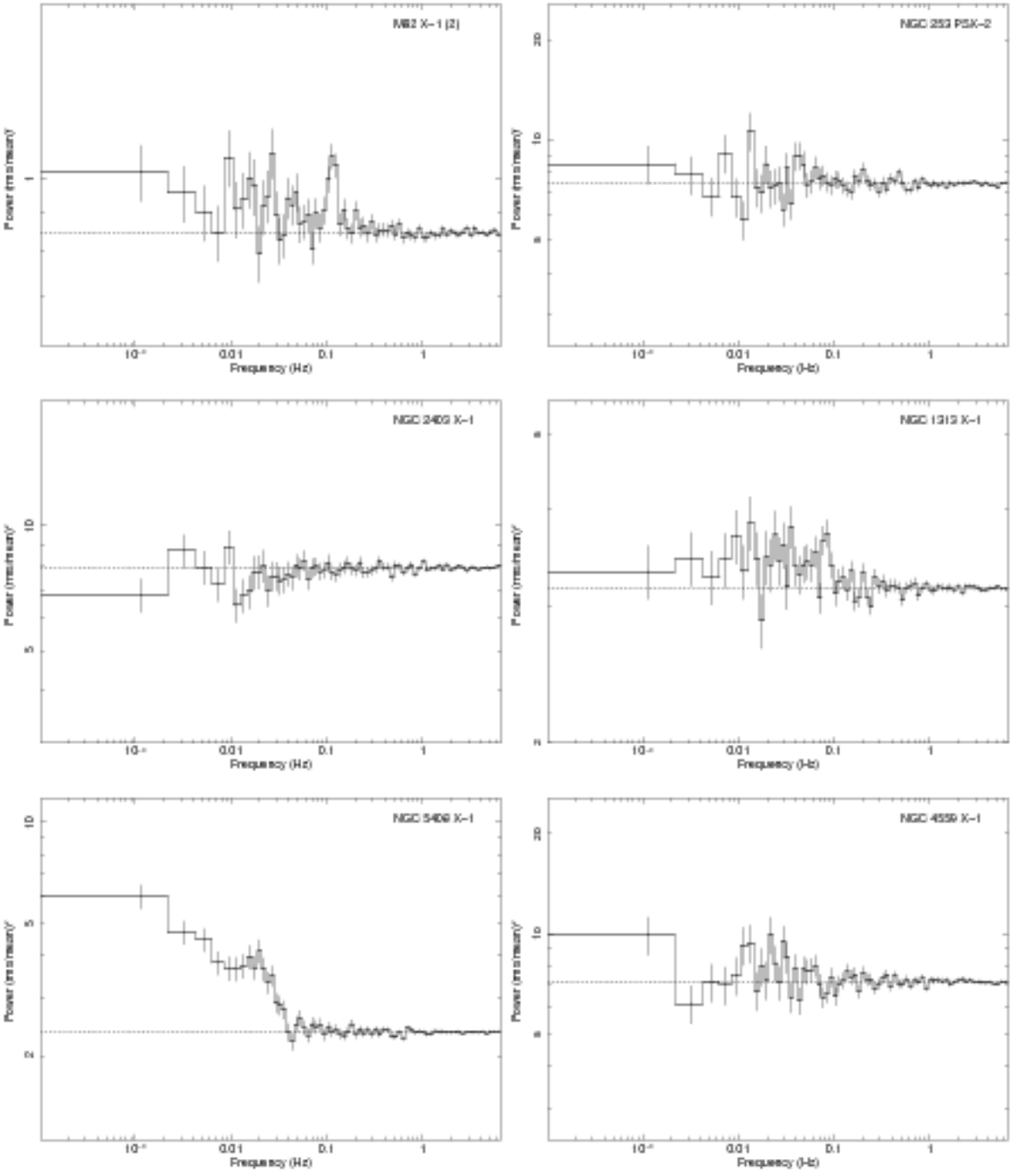
M82 X-1 (2)
NGC 253 PSX-2
NGC 2403 X-1
NGC 1313 X-1
NGC 5408 X-1
NGC 4559 X-1
Power (rms/mean)²
Frequency (Hz)

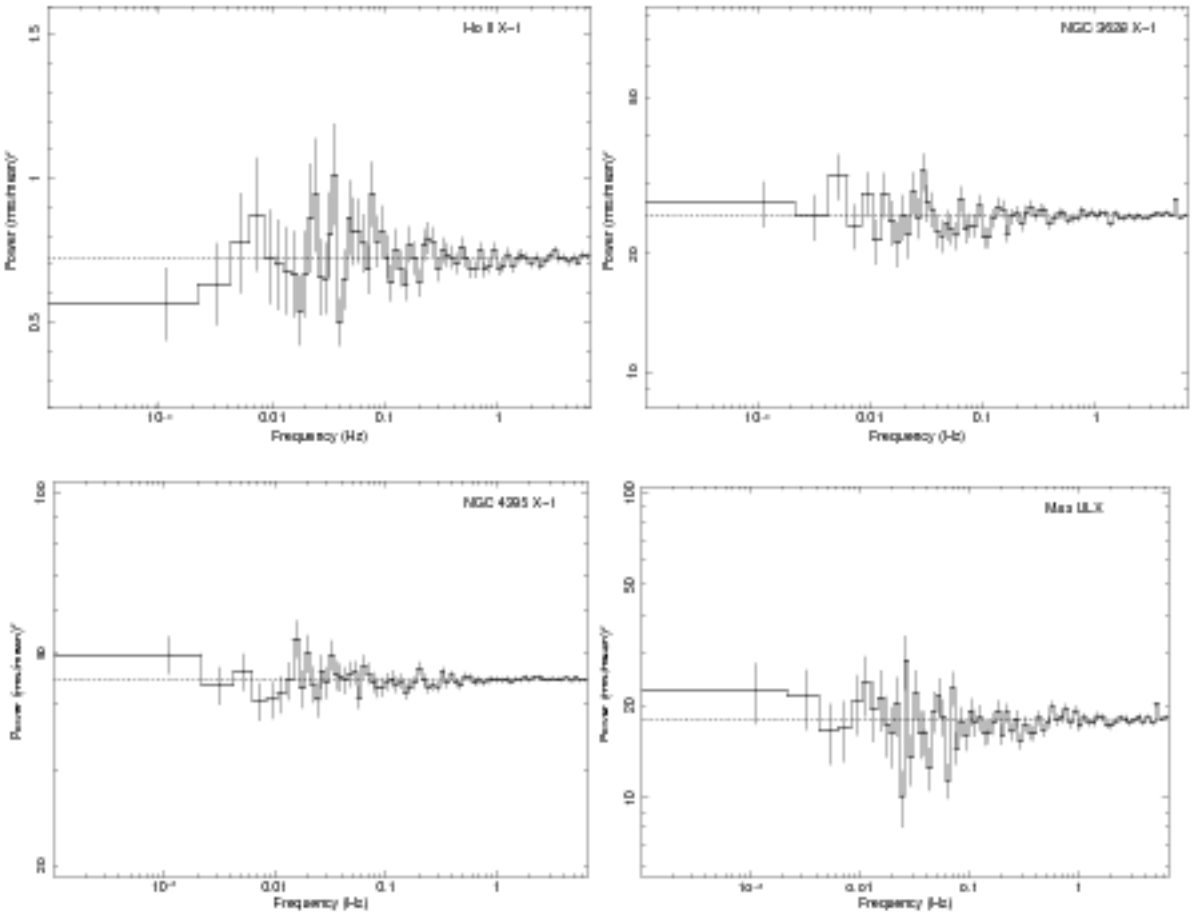

Figure 3.-1: Power spectra of 16 observations from the sample, representative of the range of variability and power seen. All light curves are split into at least 5 equal segments in time and then re-binned in frequency to give increments of $1.1f_0$. The Poisson noise level for each observation is also shown (dotted line). The top six figures show comparisons between sources which display power law type variability and sources which display no strong short term variability, just Poisson noise. The figure of the second observation of M82 X-1 (obs. ID. 02060801) shows variability but not of a power law type, it is visible as excess power in the PSD above the line indicating the Poisson noise level. The QPO in M82 X-1 at 0.12 Hz is clearly visible, as is the steep, strong red-noise feature at low frequencies in the PSD from the first observation of NGC 55 ULX (obs. ID. 0028740201)

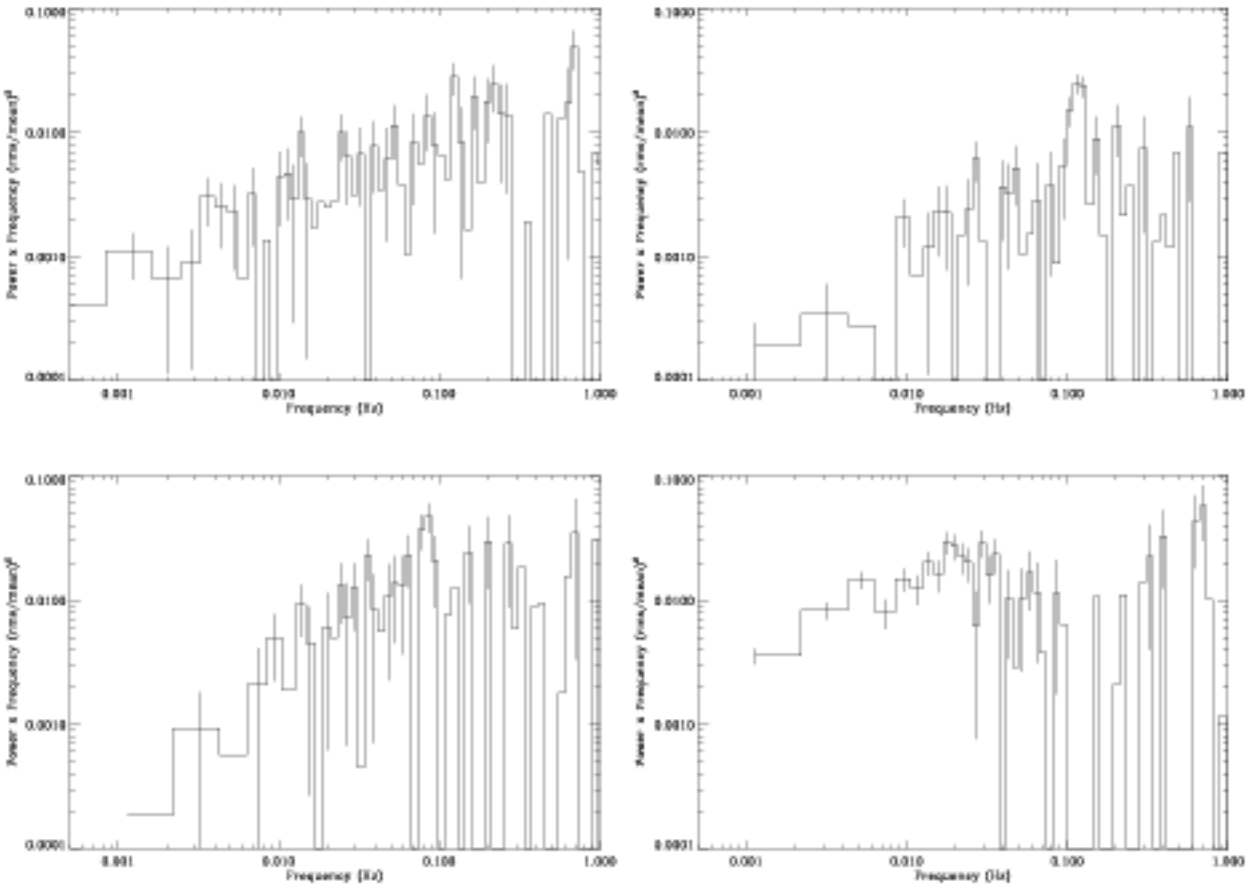

Figure 3.0: Figure showing the most variable sources with $\nu \times P$ on the y axis, this allows for greater comparison between ULXs and black hole binaries. *Top Left* Holmberg IX X-1 *Top Right* M82 X-1 (2) *Bottom Left* NGC 1313 X1 *Bottom Right* NGC 5408 X-1

A reasonable test for the presence of intrinsic variability is therefore a χ^2 goodness-of-fit test comparing the data to a constant. The results are given in Table 3.2. Sources with a $p-$value ≤ 0.05 were considered to show significant intrinsic variability (with this threshold one might expect $\sim$ 1 false detection in a sample of 19 observations). In fact six sources (eight observations) showed significant variability: Ho IX X-1, NGC 5408 X-1, NGC 1313 X-1, NGC 1313 X-2, NGC 55 ULX and M82 X-1. Investigation of the PSD from NGC 4559 X-1 revealed it to be flat with no indication of the variability features analysed in Cropper et al. (2004), this is believed to be due to artificial variability caused by the analysis method as discussed in Barnard et al. (2007).

Source Name (1)	χ^2/dof (2)	P_{null} (3)	Var. (4)
NGC 55 ULX	128.9/63	1.35×10^{-3}	P
	155.4/63	$< \times10^{-6}$	P
NGC 253 PSX2	74.8/63	0.255	N
NGC 1313 X-1	110.0/63	3.07×10^{-3}	P*
NGC 1313 X-2	128.6/91	1.13×10^{-2}	P
NGC 2403 X-1	58.9/63	0.193	N
Holmberg II X-1	85.3/63	0.554	N
M82 X-1	108.3/63	3.78×10^{-2}	Pq
	160.3/63	$< \times10^{-6}$	Pq*
Holmberg IX X-1	261.6/63	$< \times10^{-6}$	P
NGC 3628 X-1	84.7/64	0.134	N
NGC 4395 X-1	78.1/77	0.413	N
NGC 4559 X-1	78.3/63	0.409	N
NGC 4861 ULX	64.6/63	0.375	N
NGC 4945 XMM1	61.1/63	0.746	N
NGC 5204 X-1	47.2/63	0.875	N
	68.8/63	0.276	N
M83 ULX	158.3/63	0.068	N
NGC 5408 X-1	437.9/63	$< \times10^{-6}$	Pq

Table 3.2: Results on fitting a constant to determine variability. (1) Source Name; (2) χ^2 and dof values for PSD after fitting with a constant model; (3) Null Hypothesis Probability for PSD fit with a constant (4) Assessment of Variability; N denotes no observed variability, P power law type variability, $*$ indicates the variability is of a white noise form, q PSD contains a QPO

With the exception of the second observation of M82 X-1 and the observation of NGC 1313 X-1, which display variability in the power spectrum close to the Poisson noise level (Dewangan et al., 2006b; Mucciarelli et al., 2006), the variable objects all show a clear rise towards low frequencies compared to the observations with flat PSDs (e.g. Ho II X-1, NGC 5204 X-1). The continuing rise seen in *RXTE* observations of M82 X-1 with a power law of -1 (Kaaret et al., 2006; Kaaret & Feng, 2007) supported by evidence of breaks seen in NGC 5408 X-1 suggests that the PSDs are best fit with a broken power law model over a broad Lorentzian. For this reason power law models were fitted to the variable sources, although the limited number of points at low frequencies made it difficult to constrain the model parameters. The

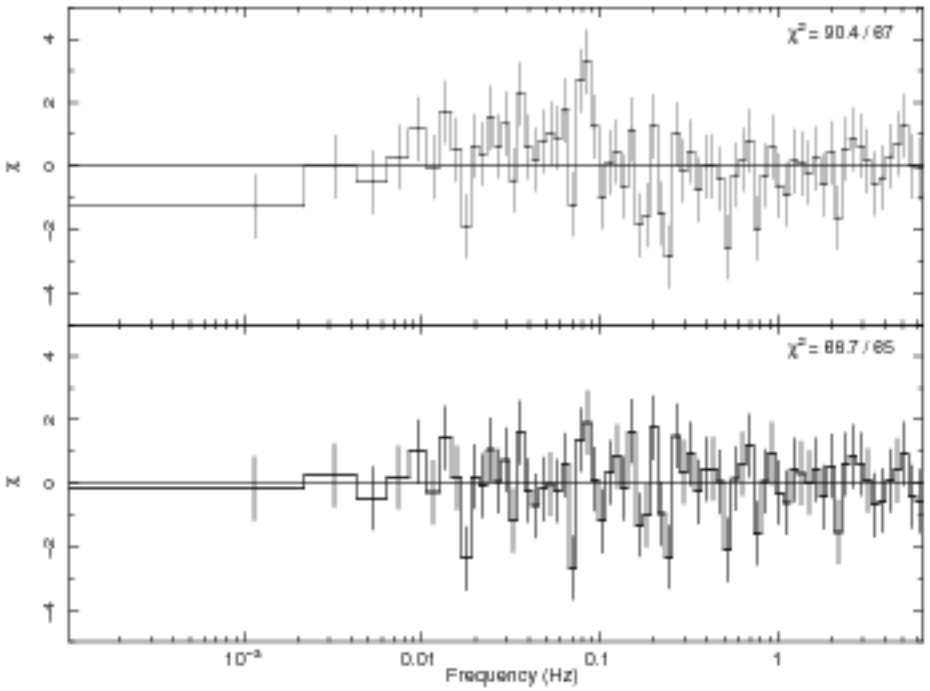

Figure 3.1: Standardised residuals for Power law (*top*) and Broken Power law (*bottom*) fits to the PSD of NGC 1313 X-1. χ^2 values for the fits are also included.

results are given in Table 3.3.

Ho IX X-1, NGC 1313 X-2, NGC 55 ULX and M82 X-1 (obs. Id. 0112290201) were fitted best with a power law (plus a constant for the Poisson noise). NGC 5408 X-1, M82 X-1 (obs Id 0206080101) and NGC 1313 X-1 were fitted better with a broken power law (plus a constant) as used in Strohmayer et al. (2007) to model the PSD from NGC 5408 X-1. This is the first report of a broken power law PSD in NGC 1313 X-1 and in order to test the plausibility of the detection we have attempted to fit the PSD with a power law (+ constant) model, and compared the χ^2 value from this fit to that of a broken-power law (+ constant) model which has two further free parameters. Analysing the difference between the two χ^2 values both through direct comparison and the *F-test* suggest that the spectral break at 0.09 Hz is significant and necessary to the fit with $p_{null} \approx 10^{-4}$. Fig. 3.1 shows the standardised residuals after fitting these two models.

In the cases of M82 X-1 and NGC 5408 X-1 the obvious QPOs were modelled with narrow Lorentzians (see below). The power law-like regions can all be fitted with slopes between -2 and -0.5. For those sources with previous analyses of their variability (M82 X-1, NGC 5408 X-1 and Ho IX X-1) the power law slopes, break frequencies and Lorentzian parameters found agree with the previous results, with the exception of the QPO identified in Holmberg IX X-1 by Dewangan et al. (2006a) which was not reproduced with high significance although a continuum PSD is visible.

Source	α_1	f_b (10^{-2} Hz)	α_2	A_1	C_P	χ^2/dof
(1)	(2)	(3)	(4)	(5)	(6)	(7)
NGC 55 ULX (1)	1.75±0.2	-	-	(1.53±0.6)×10^{-5}	$1.71^{+0.06}_{-0.02}$	86.9/70
NGC 55 ULX (2)	1.96±0.04	-	-	(6.55±2.0)×10^{-6}	3.87±0.02	122.6/70
NGC 1313 X-1	-0.082±0.07	$9.1^{+0.6}_{-0.9}$	2.35±1.0	0.26±0.06	3.16±0.008	71.9/70
NGC 1313 X-2	$1.91^{+0.05}_{-0.1}$	-	-	(5.82±3.0)×10^{-7}	2.59±0.007	69.3/70
M82 X-1 (1)	0.70±0.06	-	-	(1.1±0.3) × 10^{-2}	1.346±0.006	41.6/55
M82 X-1 (2)	$0.14^{+0.02}_{-0.05}$	2.0±1	$1.11^{+0.8}_{-0.3}$	(5.5±2.2) × 10^{-2}	0.847±0.002	66.7/70
Holmberg IX X-1	0.48±0.04	-	-	(2.55±0.3)×10^{-2}	1.36±0.04	73.6/70
NGC 5408 X-1	$-0.10^{+0.07}_{-0.03}$	$0.3^{+0.04}_{-0.07}$	$1.45^{+0.5}_{-0.2}$	4.0±0.8	2.31±0.01	100.2/77

Table 3.3: Best fit models for the sample sources displaying variability. (1) Source names; (2) Power law index (below break for broken power law); (3) Break frequency of broken power law component in Hz; (4) power law index above the break; (5) Normalisation of power law/broken power law component; (6) Normalisation of Poisson noise component; (7) χ^2 and dof values for the fitted models. A Lorentzian component (with $Q = 5$) was included in the models fitted to the QPOs in M82 X-1 and NGC 5408. For more detailed examination of the QPOs see Strohmayer & Mushotzky (2003) and Strohmayer et al. (2007).

3.4.2 Establishing limits on the variability

The other 11 observations show no strong evidence for intrinsic variability, despite a range of observation lengths and source fluxes, and therefore sensitivity to variability. In these cases the variability amplitude was constrained, following the procedure of Goad et al. (2006), by assuming the intrinsic power spectrum has one of two generic forms common to the PSDs of BHBs and AGN.

The first model is a broken power law model. It is well established that BHBs and AGN show PSDs that are usually dominated by a broad-band noise component with a form that resembles to first-order a broken power law. Most sources show a frequency range in which the spectral index (PSD slope) is approximately -1, noise with this PSD are known as "flicker noise" (Press et al., 1992). The integral of a f^{-1} spectrum diverges (if rather slowly) to low and high frequencies, and so must break to flatter and steeper slopes respectively. Therefore, we may use a broken power law as an approximate model of the generic broad-band noise PSD.

In many AGN and soft state BHBs the low frequency break (to an index flatter than -1) is not observed and must occur at very low frequencies (Reig et al., 2003; Markowitz et al., 2003; Uttley et al., 2002; Reig et al., 2002; Churazov et al., 2001). This means a good approximation to the observed PSDs can be made by considering a singly broken power law (BPL) with indicies of -1 and -2 below and above some break frequency, respectively.

$$P(f) = \begin{cases} A\left(\frac{f}{f_b}\right)^{-1} + C_P & \text{where } f < f_b \\ A\left(\frac{f}{f_b}\right)^{-2} + C_P & \text{where } f \geq f_b \end{cases} \tag{3.1}$$

where A is a normalisation, f_b is the (high frequency) break frequency, and C_P is a constant to account for the Poisson noise. This model is shown in Figure 3.3

If we represent this spectrum in $f \times P(f)$ form the f^{-1} part of the intrinsic (i.e. after subtracting

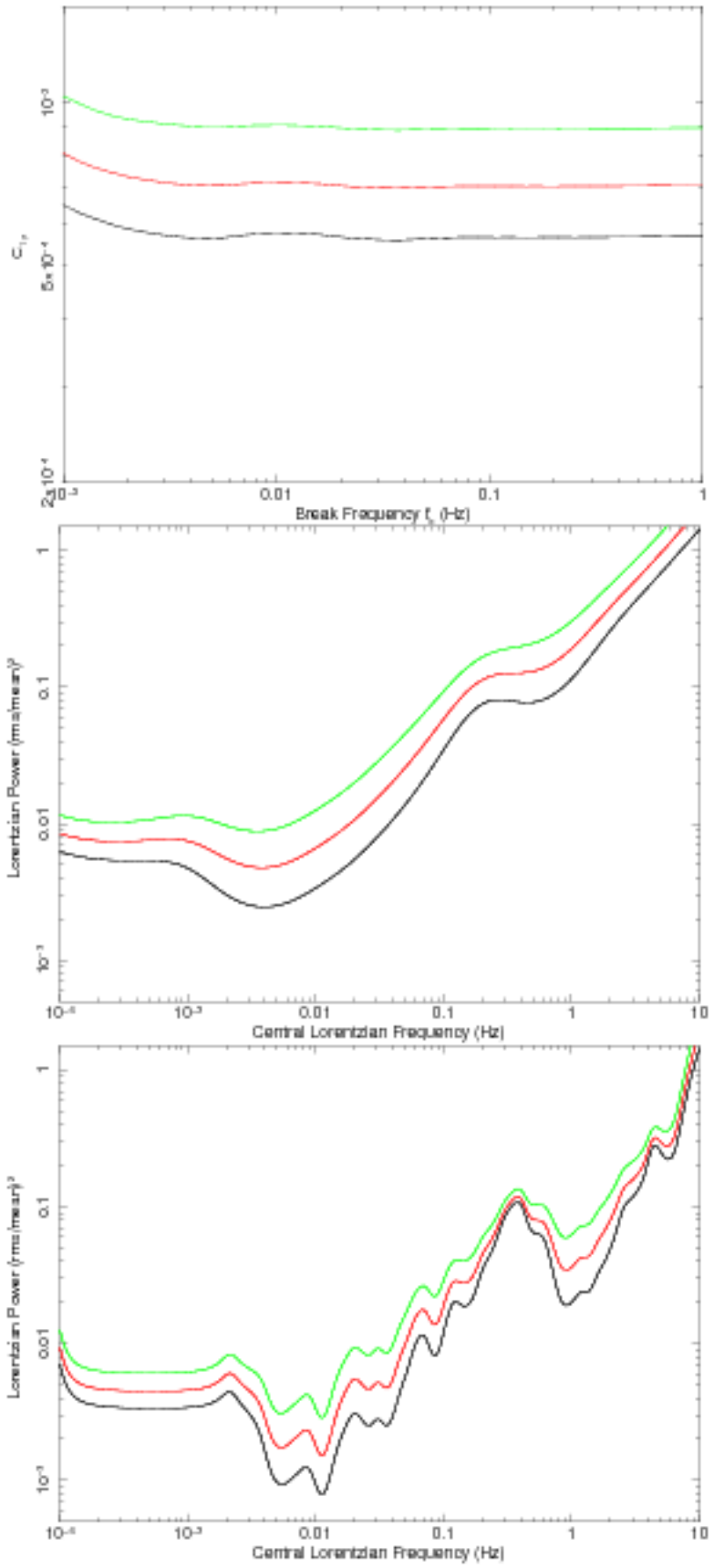

Figure 3.2: Contour plots for our three variability models from NGC 5204 (obs Id. 0405690201), limits shown correspond to $\Delta\chi^2$ = 1.0, 2.71 and 6.63. *Top:* High/soft model, broken power law -1/-2. *Centre:* Band-limited noise, Lorentzian (Q=0.5). *Bottom:* Narrow Lorentzian (Q=5.0)

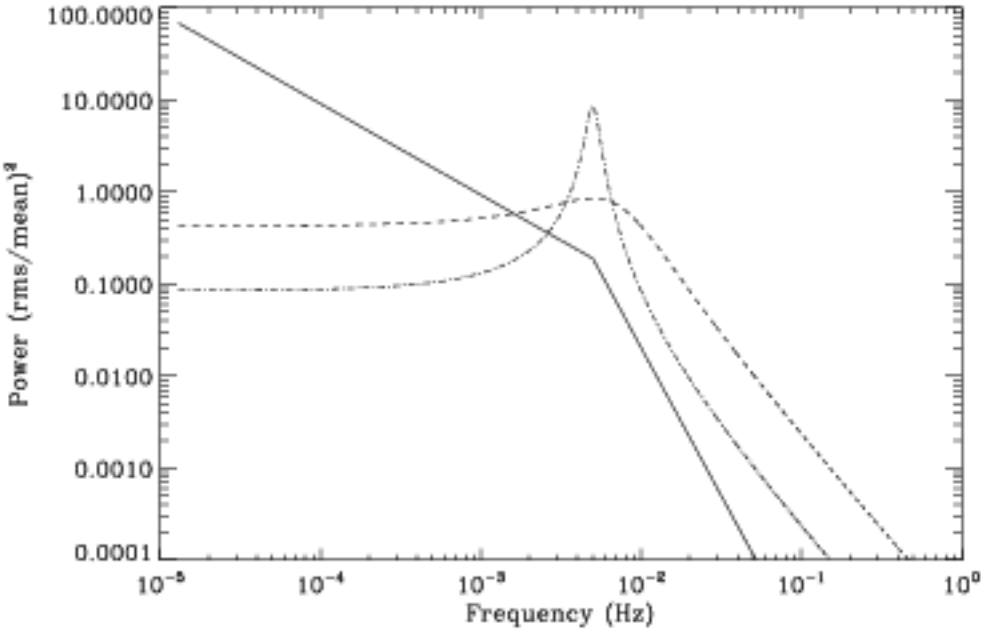

Figure 3.3: Models used to test the variability levels in the power spectra, all either break or have a central frequency of 0.005 Hz. *line* Broken power law (soft state); *dash* Broad Lorentzian Q=0.5 (BLN); *dot-dash* Narrow Lorentzian Q=5.0 (QPO)

the contribution due to Poisson noise) spectrum ($f < f_b$) becomes flat, with a constant level $C_{1/f} = f_b P(f_b) = A f_b$. It has been suggested that the value of $C_{1/f}$ is fairly constant across BHBs and AGN, with values in the range $0.001 - 0.03$ (Goad et al., 2006; Papadakis, 2004). Of course the break frequencies f_b vary widely from source to source – from 10^{-7} Hz for AGN with BH masses $\sim 10^8$ $M_\odot$, to ~ 10 Hz in stellar mass BHBs – and on long timescales the break frequency may vary by as much as a decade in frequency for a single source (Belloni & Hasinger, 1990; Uttley et al., 2002; Belloni et al., 2002). For the non-varying ULX observations there was generally no observational constraint on f_b and so $C_{1/f}$ was estimated (or constrained) as a function of break frequency over the range $10^{-4}-1$ Hz. Figure 3.2 (top panel) shows a contour plot of the upper limit on $C_{1/f}$ as a function of f_b for NGC 5204 X-1 (obs. Id. 0405690201). The contours show the value of $C_{1/f}$ at which the χ^2 fit statistic increased by 1.0, 2.71, and 6.63 over the minimum. These correspond to the 68.3, 90 and 99 per cent quantiles of the χ^2 distribution with $\nu = 1$ degrees of freedom, and are conventionally used to

delimit confidence regions on one parameter. Here they are used to define approximate limits on the magnitude of $C_{1/f}$ as a function of f_b. Table 3.4 gives 90% limits on the value of $C_{1/f}$ for each of the sources in the sample calculated assuming two different values of f_b, namely 10^{-3} Hz and 1 Hz.

For the variable sources for which an unbroken power law was a good fit we estimate the value of $C_{1/f}$ by fitting a BPL model. Where the observed power law index was ≈ -2 (i.e. in NGC 55 ULX and NGC 1313 X-2) it was assumed that the high frequency break, f_b, must lie below the observed frequency range ($\lesssim few \times 10^{-3}$ Hz), and so we assumed $f_b = 10^{-4}$ Hz. If, on the other hand, the observed power law index was close to -1 (i.e. Holmberg IX X-1, and the first observation of M82 X-1), it was assumed that the f_b must lie close to, or higher than, the highest frequency at which ULX variability can be detected above the Poisson noise. In these cases we assumed $f_b = 1$ Hz.

In the cases of NGC 1313 X-1, NGC 5408 X-1 and the second observation of M82 X-1, where a break in the power law is detected, the observed indices at low frequencies are rather low (closer to 0 than -1) indicating that the observed PSD covers the low-intermediate part of the model. Here it is flat, breaking from an index of 0 to -1 the low frequency flattening discussed earlier. In these cases the intermediate-high part of the PSD was again assumed to break from an index of -1 to -2 at $f_b = 1$ Hz, while the low frequency index of 0 was fixed, the location of the lower frequency break was left as a free parameter.

The second model represents the band-limited noise (BLN) commonly observed in BHB hard states (Nowak, 2000; Belloni et al., 2002). In this model the variability is mostly limited to $\sim 1-2$ decades of temporal frequency (van der Klis, 2006). A simple model for this type of noise is a broad (incoherent) Lorentzian:

$$P(f) = \frac{R^2 Q f_0/\pi}{f_0^2 + Q^2(f - f_0)^2} + C_P \tag{3.2}$$

where R^2 is a normalisation term (approximately integrated power, Nowak, 2000), f_0 is the resonant frequency, and Q is the quality factor. Again, C_P is a constant to account for the Poisson noise. The Q-factor defines the frequency width of the Lorentzian, $Q \approx f_0/HWHM$ where f_0 is the central Lorentzian frequency and $HWHM$ its half width at half maximum. Typically a feature with $Q > 2$ is classified as a QPO and $Q < 2$ as band-limited noise (van der Klis, 1989a, 2006). In order to model band-limited noise a value of $Q = 0.5$ was assumed. The same model form but with $Q = 5.0$ was used to model QPO features. Of course, given the quality of the data the resonant frequency f_0 of the BLN could not be constrained, and so the strength of any BLN was estimated (or constrained) as a function of f_0 spanning $10^{-4}-1$ Hz, in the same manner as with the BPL model. In those observations that showed no obvious QPOs the same procedure was used to put limits on the strength of any QPOs as a function of QPO frequency. The middle and bottom panels of Fig. 3.2 show the upper limits on amplitudes of the BLN and QPO models for NGC 5204 X-1 (obs Id. 040569201). These were found through minimising the fit to the models over 1000 different values of either the central Lorentzian frequency or the break frequency over the *XMM-Newton* frequency range.

Table 3.4 gives the approximate limits on the amplitudes of the two models (BLN and BPL) assuming two representative values of the characteristic frequency in each case (1 mHz and 1 Hz). The limits were calculated using a $\Delta\chi^2 = 2.71$ criterion (which corresponds to the 90 per cent limit of a χ^2 distribution with $\nu = 1$). The fainter sources (such as NGC 4945 X-2, NGC 4395 X-1, NGC 4861 ULX, NGC 3628 X-1 and M83 ULX) have upper limits such that variability from these sources would have to be particularly strong to have been detectable. For example, in NGC 4395 X-1 a BLN spectrum could have $R \approx 20\%$ fractional rms and this would barely reach the 90% confidence limit even assuming a characteristic frequency best-suited to detection ($f_0 \sim 10^{-3}$ Hz). For those sources in which variability was detected the measured values of the amplitude are given for each model. The observation of NGC 5408 X-1 gives the amplitude of a BLN spectrum (assuming $f_0 \approx 10^{-3}$ Hz) as $R \approx 18\%$ whereas the upper limit on the amplitude of the same model in the case of NGC 5204 X-1 (obs Id.

0405690201) gives $R \lesssim 7\%$ even though the two observations show comparable Poisson noise levels.

3.4.3 Limits on QPOs

The data were examined for possible QPOs by re-binning the FFT data in both frequency and time using various different bin widths. As discussed above a narrow ($Q = 5$) Lorentzian was used to model a QPO. For each observation the change in χ^2 was calculated as a function of the two free parameters R^2 and f_0. An improvement of $\Delta\chi^2 = 11.3$ was considered indicative of a QPO. This process clearly recovered the known QPOs in NGC 5408 X-1 and M82 X-1 but did not find any further candidates. The known QPOs show typically $R^2 \sim 10\%$ and $f_0 \sim 2-5\times10^{-2}$ Hz. By comparison the limits on the QPO strength derived from observations of several other bright ULXs, such as NGC 5204 X-1 and Ho II X-1, show that such QPOs would have been detected if they were present (see Fig. 3.2). The QPO claimed in Ho IX X-1 by Dewangan et al. (2006a) was not reproduced with high significance. In these sources QPOs similar to those in NGC 5408 X-1 and M82 X-1 sources would have to be fairly muted if present.

3.5 Discussion

The main results of the temporal analysis of 19 observations of 16 sources may be summarised as follows:

- Six sources (eight observations) showed significant intrinsic flux variability in the $10^{-4}-1$ Hz range (NGC 5408 X-1, NGC 1313 X-1, NGC 1313 X-2, NGC 55 ULX, M82 X-1 and Ho IX X-1).

Source	Broken Power Law (BPL)		Band limited noise (BLN)		
Name	$C_{1/f}$ (10^{-4}) $10^{-3}Hz$	$C_{1/f}$ (10^{-4}) $1Hz$	R^2 (10^{-2}) $10^{-3}Hz$	R^2 (10^{-2}) $1Hz$	R^2_m (10^{-2})
(1)	(2)	(3)	(4)	(5)	(6)
NGC 55 ULX	-	177±46	-	-	3.2±0.5
	-	463±142	-	-	9.2±2
NGC 253 PSX2	< 65.4	< 18.5	< 1.64	< 35.2	-
NGC 1313 X-1	-	136±46	-	-	$6.0^{+0.8}_{-2}$
NGC 1313 X-2	-	26±14	-	-	$0.65^{+0.9}_{-0.1}$
NGC 2403 X-1	< 2.9	< 2.3	< 0.282	< 15.5	-
Holmberg II X-1	< 2.88	< 3.7	< 0.0610	< 2.23	-
M82 X-1	-	7.4±5.0	-	-	4.2±2
	-	22.1±6.0	-	-	2.5±0.5
Holmberg IX X-1	-	6.0±1.7	-	-	0.88±0.2
NGC 3628 X-1	< 170	< 43.1	< 4.49	< 33.1	-
NGC 4395 X-1	< 260	< 64.7	< 5.58	< 92.8	-
NGC 4559 X-1	< 7.11	< 28.4	< 1.72	< 43.4	-
NGC 4861 ULX	< 401	< 99	< 10.8	< 206	-
NGC 4945 XMM1	< 180	< 51.8	< 5.37	< 293	-
NGC 5204 X-1	< 21	< 5.9	< 0.494	< 10.5	-
	< 34.3	< 5.4	< 0.539	< 13.3	-
M83 ULX	< 29.1	< 64	< 7.56	< 42.3	-
NGC 5408 X-1	-	104±11	-	-	2.99±0.5

Table 3.4: Upper limits on the fitted model amplitudes using two different power spectral models. The estimate of $C_{1/f}$ from the BPL model at $f_b = 10^{-3}$ Hz for Ho II X-1 differs from the value found in Goad et al. (2006) differs due to the use of different binning for the fitting process. Columns: (1) Source Name; (2) $C_{1/f}$ from the broken power law model with $f_b = 10^{-3}$ Hz; (3) For non-varying sources: $C_{1/f}$ from the broken power model with the $f_b = 1Hz$; For varying sources: $C_{1/f}$ from fit to model according to shape of PSD: See text; (4) Upper limit on fractional rms within a Lorentzian of coherence Q=0.5 fit at 10^{-3} Hz; (5) Upper limit on fractional rms within a Lorentzian of coherence Q=0.5 fit at 1 Hz; (6) Fit normalisation values to Band limited noise when present. All limits correspond to $\Delta\chi^2 = 2.71$ (which is approximately 90% confidence).

- Of these six, two show strong QPO features (NGC 5408 X-1 and M82 X-1, as previously identified) and all show a continuum spectrum consistent with a power law or broken power law model.
- Of the remaining 10 sources, the intrinsic variability amplitudes were constrained by comparing the data to simple PSD models based on BHB observations.
- The limits obtained for several of the observations (e.g. NGC 4559 X-1, NGC 5204 X-1, Ho II X-1) are such that the strength of the intrinsic variability, in the frequency range observed, must be substantially lower than the observed power seen in the variable sources.

3.5.1 Break Frequencies and BH mass

It is in principle possible to draw inferences about the nature of the putative accreting black hole in the ULXs if analogies can be formed between their observed properties and those of BHBs and AGN. Perhaps the simplest and best studied relation linking BHBs and AGN is the correlation between the PSD break frequencies and BH mass (e.g. Markowitz et al. (2003); Done & Gierliński (2005); McHardy et al. (2006)), a correlation which may well include ULXs.

The 3 PSDs of NGC 5408 X-1, M82 X-1 (obs. ID. 0206080101) and NGC 1313 X-1 show a break from an index of ~ -1 above the break to ~ 0 below, which resembles the 'low frequency break' observed in hard BHB observations (Belloni & Hasinger, 1990; Nowak, 2000; McClintock & Remillard, 2006b). Soria et al. (2004) have used the break frequency in NGC 5408 X-1 to derive an expected BH mass of $\sim 100\ M_{\odot}$. For M82 X-1 Dewangan et al. (2006b) measured the PSD break frequency in relation to the QPO frequency and drew a comparison with BHB features in order to estimate the BH mass at $25 - 520\ M_{\odot}$. Casella et al. (2008) applied the relationship in Körding et al. (2007), which extends the analysis

from McHardy et al. (2006) into systems in a low/hard state, to estimate a BH mass between $115 - 1305\ M_{\odot}$ for NGC 5408 X-1 and $95 - 1260\ M_{\odot}$ for M82 X-1. However Middleton et al. (2010) argue that this comparison is inconsistant, they suggest that the expected break frequency should be lower than that observed in this observation of NGC 5408 X-1. Instead this QPO may be similar to the ultra-low frequency QPOs occasionally observed from GRS 1915+105.

By contrast the break in NGC 1313 X-1 at 0.09 Hz is comparable to those observed in BHBs, for example the observed break of Cyg X-1 in the low/hard state is 0.08 Hz. Cyg X-1 is thought to have a BH mass of $\sim 10 M_{\odot}$. However the observed luminosity of Cyg X-1 in this state is only $\sim 4 \times 10^{37}$ erg/s (Nowak et al., 1999) a factor of 100 lower. Either NGC 1313 X-1 hosts a commensurately larger BH mass than Cyg X-1, or it does not but is accreting at a much higher relative rate ($L/L_{\rm Edd} > 1$), or at least appears to be due to anisotropic emission (or some combination of these). In either case the flat PSD below 0.09 Hz is difficult to account for. The flat slope is most commonly observed in hard state BHBs, but this state is thought to occur when $L/L_{\rm Edd} \lesssim 0.05$ (McClintock & Remillard, 2006b). Assuming NGC 1313 X-1 to be in such a state would therefore require $M_{\rm BH} \gtrsim 600 {\rm M}_{\odot}$, yet the frequency of the break matches well the expectation for a $M_{\rm BH} \sim 10 {\rm M}_{\odot}$ black hole. This supports the suggestion that ULXs may represent a different, 'ultraluminous' state (Roberts, 2007).

NGC 1313 X-2, NGC 55 ULX and Ho IX X-1 show excess power rising to low frequencies below $\sim 5 \times 10^{-3}$ Hz. As can be seen in Figure 3.-1, the PSD from the first observation of NGC 55 ULX (obs. ID. 0028740201) shows a steep red noise region at low frequencies, also visible in the PSD from the second observation (obs. ID. 0028740101). When the two observations are fitted with a power law + constant model, spectral indices of 1.75±0.2 and 1.96±0.4 are found respectively, with no sign of a low frequency break. This would suggest, assuming the system is in the soft state, that the high frequency break would have to be below 10^{-4} Hz, indicative of a BH with a mass in excess of $10^{6}\ M_{\odot}$ (Roberts, 2007) more typical

of AGN. However it must be pointed out that dips in the light-curve have been identified (Stobbart et al., 2004) and that these features affect the PSD on timescales commensurate with the strong variability power seen in its PSD. The power laws seen in the PSDs from Ho IX X-1 and NGC 1313 X-2 have spectral indices of ~0.5 and ~1.91 respectively. The few rising points visible in the PSD of NGC 1313 X-2 do not allow for accurate fitting and so little can be derived from this value. For Ho IX X-1 however, the slope is much clearer and we have carried out a basic analysis. We have been able to constrain the likelihood of a brake to a slope of -2 to be above 0.1 Hz. This would indicate a BH with a mass below 1000 $M_{\odot}$ (Roberts, 2007).

The possibility of estimating the masses of ULXs by comparing characteristic (e.g. break or QPO) frequencies with those observed in BHBs and AGN, is dependent on there being a suitably strong analogy mapping PSD characteristics between the source, together with a simple mass-frequency scaling relation (McHardy et al., 2006). The recent discovery of an apparent high frequency QPO within a AGN (Gierliński et al., 2008) indicates that these features are common across the range of observed sources. If however ULXs do not display variability in forms typical to either BHBs or AGN and instead exist in a new 'Ultraluminous state' (Stobbart et al., 2006; Roberts, 2007; Gladstone et al., 2009) with distinct and different characteristics to those states observed in AGN and BHBs, then these mass estimates will no longer be reliable.

3.5.2 Variability vs Flux and Luminosity

The two main properties of an observation that determine the sensitivity to intrinsic spectral power at a given frequency are the length of the observation T (the number of 'cycles' of that frequency that were observed) and the count rate of the source (which determines the Poisson noise in the observation). Denoting the mean count rate as I we may approximate

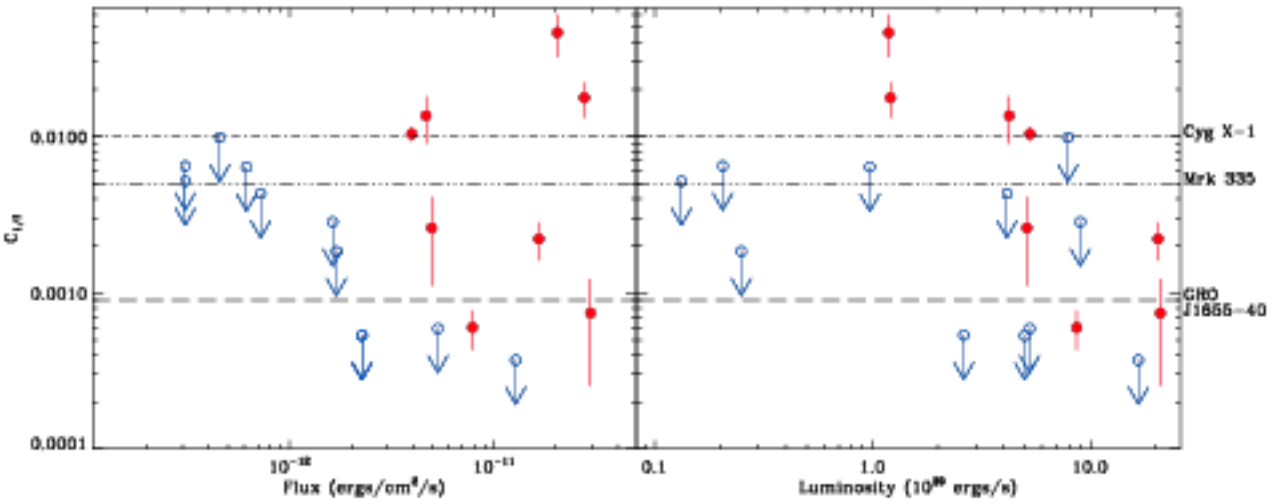

Figure 3.4: Upper limits to high/soft model against Flux *(left)* and luminosity *(right)* for f_b = 1 mHz. Points defined as varying are represented by filled circles, whilst non-varying sources are unfilled. Also shown are the measured values of $C_{1/f}$ for BHBs Cygnus X-1 (Uttley, 2007) and GRO J1655-40 from an anomalous soft state, also the AGN Mrk 335 (Arévalo et al., 2008), for reference the luminosities of these sources are ~3×10^{37} erg/s, ~7×10^{37} erg/s and ~3×10^{43} erg/s respectively.

the significance (in units of σ) of an excess in power over the Poisson noise level by $n_\sigma(f) \approx \frac{1}{2}IP_S(f)\sqrt{T \times \Delta f(f)}$ (see van der Klis, 1989b) where $P_S(f)$ is the power density due to the intrinsic variations in the source flux, and $\Delta f(f)$ gives the frequency binning. Thus, with similar observation lengths T and frequency re-binning $\Delta f(f)$ the sensitivity should scale as $n_\sigma \propto IP_S(f)$ and so if a detection is made when n_σ exceeds some number the limit on the power that can be detected scales as $P_S(f) \propto I^{-1}$.

Fig. 3.4 (left panel) shows the estimated variability amplitudes (detections and upper limits) against source flux. Also on these plots are typical values for $C_{1/f}$ observed in the BHBs Cyg X-1, GRO J1655-40 in an anomalous soft state and the AGN Mrk 335, illustrating the consistency in $C_{1/f}$ between BHBs and AGN. The upper limits clearly improve (i.e. give tighter limits) at higher fluxes, as expected. In particular, they indicate it is in general not possible to detect even strong variability ($C_{1/f} > 0.05$) in sources fainter than $\sim 10^{-12}$ erg s^{-1} cm^{-1}. Fig. 3.4 (right panel) shows the same variability amplitudes against observed X-ray luminosity, with no strong trend apparent. Above 10^{39} erg s^{-1} (i.e. definite ULX luminosities) there is

a range of ~ 30 in the variability amplitude, confounding any efforts to identify source states on the basis of luminosity-variability correlations. Considering only those source for which variability was detected (filled circles) there appears to be a correlation suggesting a decrease in variability with increasing luminosity. However there are two reasons why this could be misleading. The first is that the two highest estimated values of $C_{1/f}$ are the observations of NGC 55 ULX. This source shows dipping episodes in its variability (Stobbart et al., 2004), not seen in other ULXs, and this anomalous behaviour enhances the variability amplitude. Removing these points substantially decreases the apparent significance of any luminosity-amplitude anti-correlation. Secondly, including the limits from observations that did not have variability detections shows that some lower luminosity sources ($\sim 10^{39}$ erg s^{-1}) must have very low amplitude variability, opposite to the prediction of a general luminosity-amplitude anti-correlation. When these points are considered there appears to be no obvious correlations within the plot.

3.5.3 Are some ULXs significantly less variable?

The upper limit contours from four bright sources (Ho II X-1, NGC 2403 X-1, NGC 5204 X-1 and NGC 4559 X-1) show that these sources are significantly less variable than others (such as NGC 55 ULX, NGC 5408 X-1, etc.). Fig. 3.6 compares the data from NGC 5204 X-1 with the model obtained by fitting the data from NGC 5408 X-1 (these two have similar luminosities and count rates, and hence Poisson noise levels in their PSDs). The figure clearly shows the variability seen in NGC 5408 X-1 to be absent or greatly suppressed in NGC 5204 X-1.

The difference between the strength of variability observed in many ULXs and that expected by analogy with BHBs was confirmed using simulated data. Two PSDs of Cyg X-1 – one showing BLN (hard state) and one showing BPL (soft state)[3], an observation of GRO J1655-

[3]For Cygnus X-1 the observations were taken from the *RXTE* archive: the BLN data came from proposal P10236 made on 1996 December 16-18 and the BPL data came from P10512 made on taken 1996 June 18. The

40 in an anomalous soft state and one of XTE J1550-564 in a typical soft state – were used as examples of BHB variability. Random time series were generated from these PSDs (using the method of Timmer & König, 1995) and given the same mean count rate and exposure time as the *XMM-Newton* observation of Holmberg II X-1. Poisson noise was included at the appropriate level, and the simulated data were analysed in the same manner as the real ULX data. Variability was clearly detected (i.e. a constant was rejected by a χ^2 goodness-of-fit test) in the simulated data for the first three PSD shapes. The same was true when the PSD frequencies were reduced (by factors of up to 10^5) prior to generating the time series - i.e. simulating the effects of larger black hole masses by scaling the variability timescales. The simulations with the same shape as the soft state PSD from XTE J1550-564 had no detectable variability, although if the source is in a similar state to this the energy spectra is expected to be dominated by a disc-like component which is not observed here – this is discussed further below.

The results confirm that if Holmberg II X-1 was variable with a PSD shape and amplitude similar to that seen in Cyg X-1 its variability should have been detected (at high significance) in the *XMM-Newton* observations. This is true whether the PSD shape is BPL or BLN, and holds when the characteristic variability frequencies are reduced as might be expected for IMBHs. The results of the simulations confirm the the PSD fitting results (discussed above), namely that the apparent lack of variability in the observations of sources such as Holmberg II X-1 and NGC 5204 X-1 must be intrinsic to the sources, not a result of insufficient observations.

3.5.4 Interpreting the lack of variability

There are two fundamentally different ways to account for the lack of variability in the ULX observations: as an observational effect caused by the limited energy or frequency bandpass of

observation of GRO J1655-40 was from P91702 taken on 2005 May 24 and XTE J1550-564 from P40401 on 1999 Jan 6.

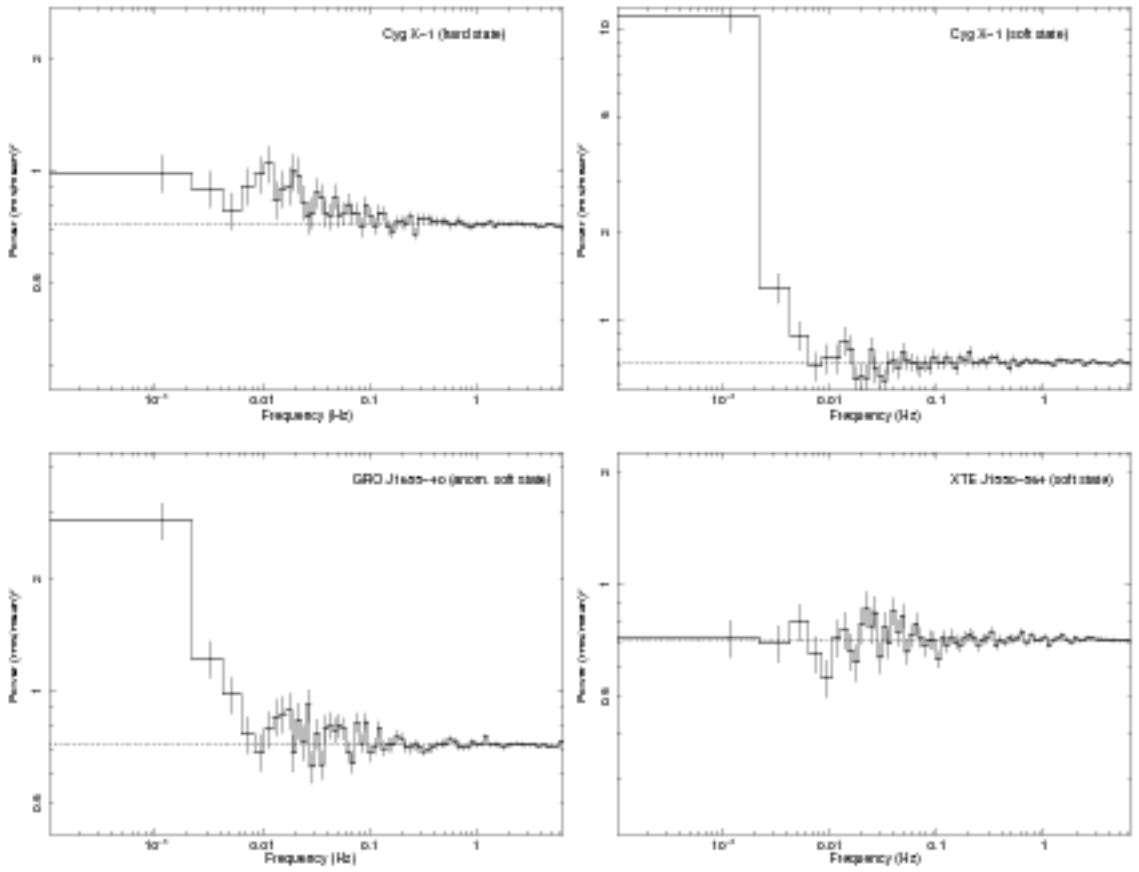

Figure 3.5: Simulated power spectra from Holmberg II using models from black hole X-ray binaries scaled down to frequencies expected for IMBHs. *top left* Cygnus X-1 hard state; *top right* Cygnus X-1 soft state; *bottom left* GRO J1655-40 Anomalous soft state; *bottom right* XTE J1550-564 soft state.

the observations, or as a result of the sources being intrinsically under-variable. We consider some specific possibilities below.

The energy spectra of BHBs in their higher accretion rate states are often dominated by a (quasi-)thermal component associated with the accretion disc. By comparison with the non-thermal (power law-like) hard X-ray continuum, this spectral component shows little short term variability (Churazov et al., 2001). LMC X-3 is an example of a BHB that often shows very low amplitude short term variability in the soft state (dominated by thermal disc emission; Nowak et al., 2001). See also a discussion of this point in the context of BHB-AGN comparisons in Done & Gierliński (2005). It could be that a similar component dominates the

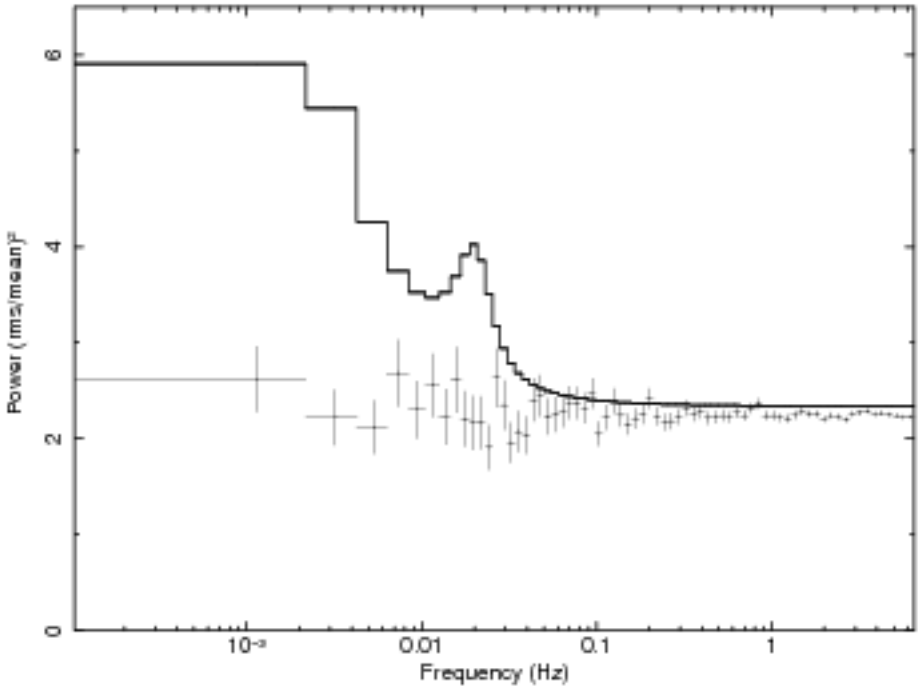

Figure 3.6: Average power spectra of NGC 5204 (obs Id. 0405690501) with the best fitting model for NGC 5408 X-1, demonstrating clear absence of variability in the former source even though the observed luminosities from the two observations are very similar.

spectra of the under-variable ULXs within the *XMM-Newton* bandpass. If this was the case we would expect the thermal emission to peak around $\sim 1-2$ keV, higher than expected for IMBH models, which predict a much cooler temperature ~ 0.2 keV (Miller et al., 2003, 2004; Stobbart et al., 2006), i.e. this solution requires BH masses similar to Galactic BHBs. One problem with this hypothesis is that the energy spectra of ULXs often appear more complex than the thermal-dominated spectra of soft BHBs when viewed in the highest quality XMM-Newton observations (Stobbart et al. (2006); Gladstone et al. (2009)), they can only be fit with a model consisting of two components rather than a single thermal one. There are some ULXs that do appear to have modified disc-like spectra, although they still do not appear to be in a true thermally dominant state (e.g. Vierdayanti et al. (2006); Hui & Krolik (2008); Feng et al. (2010)). A prediction of this hypothesis is that the sub-variable ULXs should show stronger variability at higher energies, where the spectrum is dominated by variable non-thermal emission.

Goad et al. (2006) suggested that the lack of variability seen in Holmberg II X-1 may be

related to states observed in GRS 1915+105, where the variability power is concentrated in a BLN spectrum at high frequencies (> 0.1 Hz) and there is often little variability on longer timescales, such as the 'χ' state or that observed with ultra-low frequency QPOs (Belloni et al., 2000; Middleton et al., 2010). The integrated power over the $10^{-4} - 0.1$ Hz range is typically only $\sim 10^{-3}$ (fractional variance; see e.g. Zdziarski et al., 2005) which is close to the detection limits of the ULX observations. Again, this explanation requires BH masses comparable to that of GRS 1915+105 (~ 14 M$_{\odot}$; Greiner et al., 2001) as a significantly larger BH mass would shift the BLN variability into the frequency bandpass of the ULX observations ($10^{-4} - 0.1$ Hz) where it would be detectable. A prediction of this hypothesis is that ULXs should show significant variability power at higher frequencies (e.g. $0.2 - 20$ Hz), in the form of a BLN component and possibly strong QPOs, as does GRS 1915+105.

The above explanations hypothesise that the variability in ULXs is similar to that of BHBs (and AGN) but is often not observed due to the limited energy and/or frequency bandpass of the available data. Another possibility is that the X-ray emission from ULXs is intrinsically less variable (on frequencies > 10^{-3} Hz) than expected by analogy with other accreting systems.

The timescales involved are sufficiently large to suggest difficulties with at least one model for the suppression of variability within the ULX system: scattering in an extended region. Recent studies of the X-ray spectra of ULXs (e.g. Done & Kubota, 2006; Stobbart et al., 2006; Goad et al., 2006) have put forward the idea of an optically thick corona of hot electrons that modifies the emerging energy spectrum. The timescale for the diffusion of photons through an electron scattering medium is of order $\Delta t \sim R\tau_{es}/c$, where R is the size of the scattering region and τ_{es} ($\gtrsim 1$) is the optical depth to electron scattering (see e.g. Nowak et al., 1999; Miyamoto et al., 1988, and references therein). On timescales shorter than Δt the variability will be strongly attenuated. The ULX observations show weak or absent variability on timescales at least as large as $\sim 10^2$ s, which would require $R\tau_{es} \sim 100$ lt-s. This is exceedingly large; even with $M_{\rm BH} \sim 100$ M$_{\odot}$ an optical depth of $\tau_{es} \sim 10 - 20$ (see Gladstone et al., 2009) would need

a scattering region as large as $R \sim 2 \times 10^9$ m ($\sim 7 \times 10^3$ gravitational radii), comparable to the binary separation of Cyg X-1. This analysis suggests electron scattering requires a very large covering outflow before it can be a viable mechanism for suppressing variability in ULXs on such long timescales, although the effect on the energy spectra require a much smaller emission region than needed here.

Of course, it remains plausible that ULXs are examples of an accretion state that is simply not found (or very rare) among the commonly observed BHBs and AGN, and which displays very stable X-ray emission. Nevertheless, any mechanism for explaining the lack of variability in some ULXs faces a challenge: the X-ray spectra of the variable (e.g. NGC 5408 X-1) and non-variable (NGC 5204 X-1) ULXs are quite similar (Soria et al., 2004; Roberts et al., 2006; Stobbart et al., 2006) while their variability properties appear very different (see Fig. 3.6). This apparent inconsistency requires further study to understand fully, multiple observations of a few ULXs could allow for further clarification of this problem.

Longer observations with *XMM-Newton* would allow the frequency range to be extended to lower frequencies and could reveal in more detail the PSDs of ULXs such as NGC 55 ULX and NGC 1313 X-2, allowing better comparisons with BHBs and AGN. Observations of ULXs with more powerful X-ray missions (such as *Astro-H* and the proposed *International X-ray Observatory*) are needed before ULX variability can be studied at the higher frequencies and in the higher energy bands needed to test the hypotheses discussed above.

Chapter 4

Rms-flux relation in a selection of black hole binaries

4.1 Introduction

One property which appears to be common to some accreting compact objects is a linear relationship between the rms variability of a source and the count rate. Initially discovered in observations of BHBs (Uttley & McHardy, 2001), this rms-flux relation has now been investigated in a few observations of a number of BHBs, AGN and a neutron star X-ray binary (Uttley & McHardy, 2001; Uttley, 2004; Gaskell, 2004; Uttley et al., 2005, see e.g.) and studied in detail for all *RXTE* observations of Cyg X-1 up to early 2003 (Gleissner et al., 2004). It has also been observed in optical observations of three BHBs in the low-hard state (Gandhi, 2009). The range of compact objects from which this relationship has now been observed is striking and leads to the question of how ubiquitous it is. If it is seen in a wide range of objects in a variety of different states, then is it in fact an essential product of the accretion flow?

The rms-flux relation in Cygnus X-1 is visible over a wide range of timescales, from seconds to years (Gleissner et al., 2004). This time range and consistency is difficult to explain using models employing additions of independent shots, a connection is required between variability occuring over timescales of years and that happening in seconds. A propogating fluctuations model, such as that suggested by Lyubarskii (1997); King et al. (2004), where long-term variations from the outer reaches of the disc propogate inwards coupling to short-term variations at smaller anulli. This modulation implies that the flux distribution from the source should be log-normal (Uttley et al., 2005), if the variations containing an rms-flux relation are the dominant emmision component. Log-normal flux distributions have been observed from various BHBs and AGN (see e.g. Uttley et al., 2005; Gaskell, 2004; Giebels & Degrange, 2009). Other models suggested for the rms-flux relation in ULXs includes emission from a clumpy wind (Middleton et al., 2010).

Although the relation has been studied in many observations of Cyg X-1 and a selected few other BHBs, it has not been consistently observed in a transient source which shows the full range of states. If the rms-flux relation is visible in all states then this points to the ubiquity of the relation, alternatively if the relation is not seen in a particular state it futher demonstrates differences in the variability. In order to test the ubiquity of the rms-flux relation in BHBs we have utilised the full range of data from 9 BHBs in the *RXTE* archive.

4.2 Data Analysis

4.2.1 Lightcurve extraction

We have utilised most of the publicly available data (excluding only Observations Identifiers containing less than 5 observations) from the *RXTE* archive for the 9 BHBs in table 4.1 taken

by the *RXTE* Proportional Counter Array (PCA) since the mission began. All lightcurves have been extracted and then binned to around 3 ms depending on the mode the data was initially taken in and the initial time resolution. The analysis was limited to those observations taken in either Binned, Single Bit or Event modes, observations not taken in any of these modes have been excluded from the data set. If observations were made with some or all of these modes in the energy range required, then binned or event mode data was used preferentially due to the restricted energy selection in single bt mode. We have also excluded observations without a concurrent file in standard 2 mode, as this data was used for the background reduction (this mainly applies to a few observations taken when there were problems with the hardware on *RXTE*). In order to adjust for the differing combinations of detectors used in observations taken with the PCA all results presented here are corrected to one PCU. In general these objects have been observed when they go into outburst as the count rates in quiescence are very low (excepting for Cygnus X-1). Consequently the observations are not evenly sampled in time but do represent a range of states for each source.

The initial analysis was carried out in the closest range to 2-13 keV allowed by the energy binning for the observation. As standard 2 channel 0 is thought to introduce artificial variability into the lightcurves (see e.g. Gleissner et al., 2004) this channel was excluded. The energies which can be extracted over are dependent on the channel grouping used for the data mode, consequently the range is not the same for all observations, but the counts extracted were from the closest to the 2-13 keV range possible. The lightcurves are then background corrected, using simulated background lightcurves produced by the ftool PCABACKEST. It is recommended that observations with count rates < 40 ct/s/PCU use the models for faint sources. As our observations span a wide range of count rates, we tested observations close to the faint model limit with both background models. This showed little difference in our final results whether the model was chosen based on count rate or the bright model was applied to all data. We chose the latter as this ensured consistency in data extraction. It also excluded the possibility of anomalous results for observations with count rates close to the recommended cut-off

Table 4.1

Target	Total obs.	Obs. >3% σ_{frac}	Good obs.
(1)	(2)	(3)	(4)
GX 339-4	487	376	234
XTE J1118+480	33	30	26
GS 1354-64	8	7	7
4U 1543-475	97	25	12
XTE J1550-564	153	106	80
XTE J1650-500	177	69	39
GRO J1655-40	462	140	93
H1743-322	667	297	129
XTE J1859+226	123	55	12
Total	2178	1159	676

Table 4.2: Note: The 1998 outburst of XTE J1550-564 is excluded from this data set due to the strong QPO

between the two models, where observations with very similar count rates could have different background models applied. Observations with a count rate < 10 ct/s/PCU are excluded from the sample.

4.2.2 Calculation of the rms-flux relation

The resultant background corrected lightcurves were then split into continuous segments of 3 s in length and the mean flux ($\langle F \rangle$) was found for each segment. Periodograms were then measured for the segments in absolute normalisation (see Chapter 1), in this normalisation the integrated area underneath the power spectrum is equal to the variance. The stochastic nature of the lightcurve results in scatter in the periodogram, as discussed in Chapter 1 the measured power values are scattered around the true value according to a χ^2 distribution with two degrees of freedom (see e.g. van der Klis, 1989a). In order to reduce this effect and estimate the real value of the power in each frequency bin, the periodograms were averaged into flux bins. The number of periodograms per bin was dependent on the number of segments in the individual observations but this ranged between 25 - 100, ensuring each observation

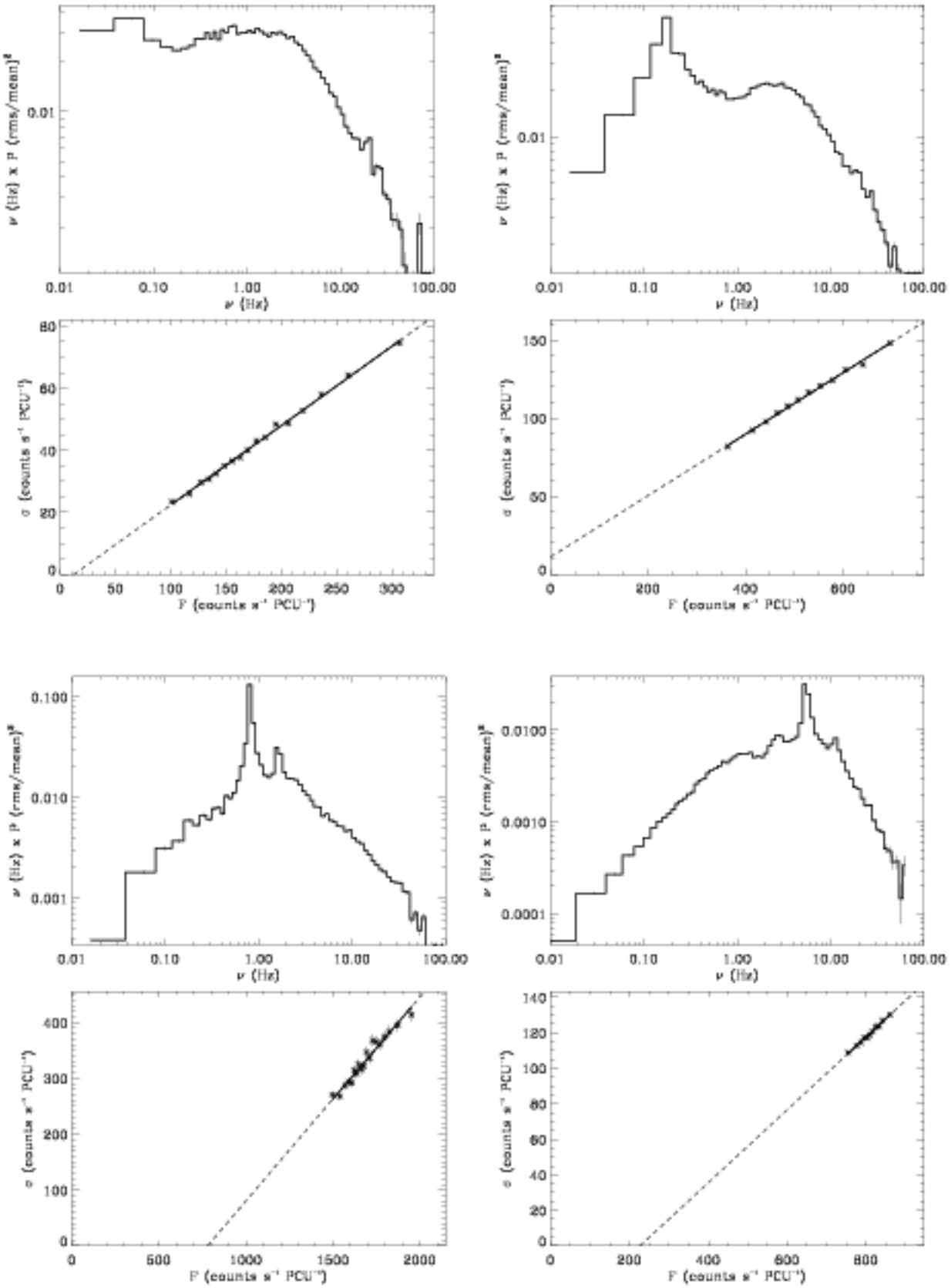
ν (Hz) x P (rms/mean)²
ν (Hz)
σ (counts s⁻¹ PCU⁻¹)
P (counts s⁻¹ PCU⁻¹)

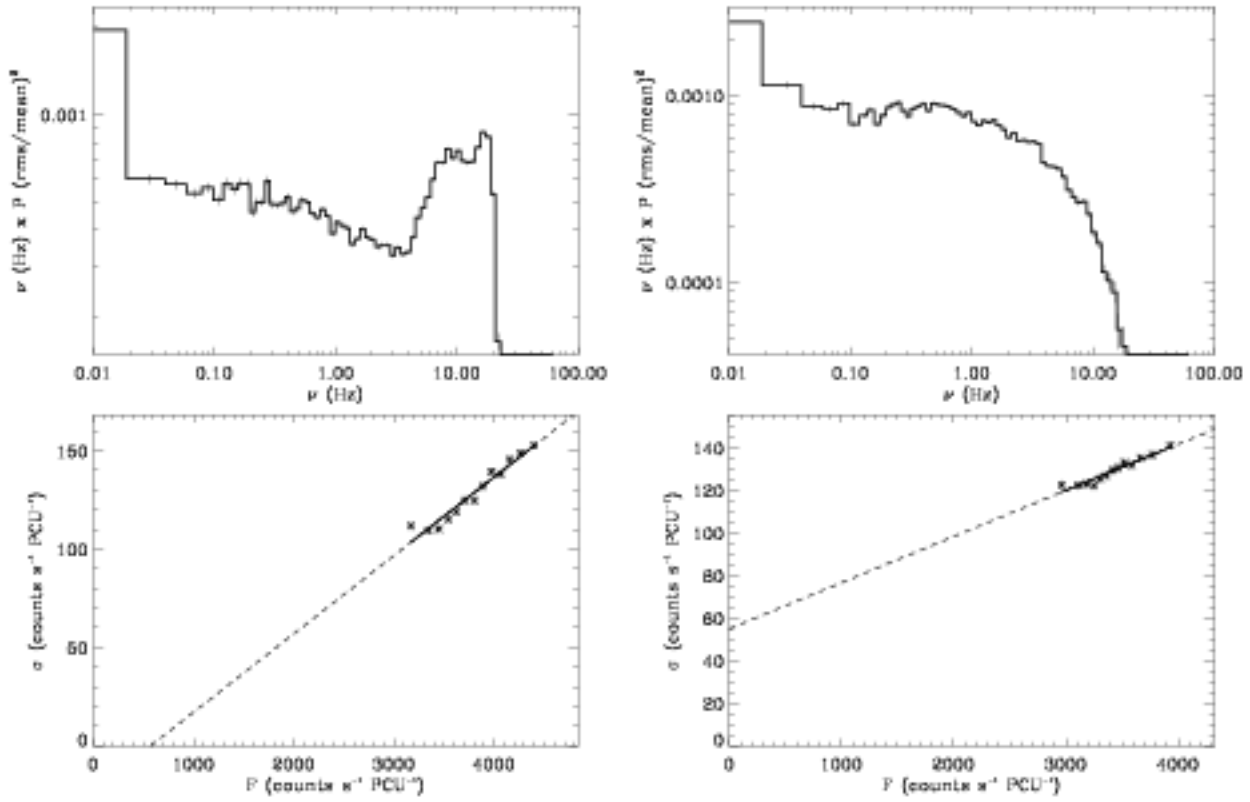

Figure 4.1: Examples of good rms-flux relations. *Overleaf: Top left a*: XTE J1550-564 (obs.id. 80135-01-04-00) *Top right b*: GX339-4 (obs. id. 95409-01-12-01), *Bottom left c* XTE J1550-564 (obs. id. 30188-06-01-02) *Bottom right d*: GX 339-4 (obs.id. 70109-04-01-01) *Above: Left e*: GRO J1655-40 (obs. id. 91702-01-63-00), *Right f* GRO J1655-40 (obs. id. 91702-01-62-00)

contained a minimum of 10 points. The rms (σ) in absolute units is found by taking the square root of the variance, given by summing the power over the required frequency range $\nu_1 - \nu_2$ (in this case $\nu_1 = 1$ and $\nu_2 = 10$ Hz), and then multiplying by the frequency resolution ($\delta\nu$) i.e.

$$S^2 = \sum_j \langle P_j \rangle \delta\nu \tag{4.1}$$

Where the flux binned power is summed over all frequencies between ν_1 and ν_2. As the power

in each frequency bin contains a contribution from the Poisson (P_N) noise this needs to be estimated and removed so that the rms can be found

$$\sigma = \sqrt{S^2 - P_N W \delta\nu} \tag{4.2}$$

Where P_N is the power density for the Poisson noise component of the variance and is given by $P_N = 2(x + B)$, where x is the source count rate and B is the background. W is the number of frequency bins between $\nu_1 - \nu_2$. The flux binning allowed for an accurate calculation of the errors on the binned σ values, these were found in a more general manner to that applied in Gleissner et al. (2004). The standard error on the power for each frequency bin within the power spectra is given by

$$\delta P = \frac{\langle P_j \rangle}{\sqrt{N}} \tag{4.3}$$

where N is the number of power spectra averaged in each bin (see e.g. van der Klis, 1989a). As the variance is found by summing over each frequency bin, the error on the variance is found by summing the errors on each bin in quadrature and then corrected to find the error on the rms -

$$\delta\sigma = \frac{1}{2\sigma} \sqrt{\frac{\delta\nu^2 \sum_j \langle P_j \rangle^2}{N}} \tag{4.4}$$

The errors calculated in Gleissner et al. (2004) assumed that the power remains the same in all frequency bins which produces smaller errors than expected if the power is instead concentrated into a few frequency bins.

4.2.3 Fitting the linear relation

Following Uttley & McHardy (2001) we have assumed that the rms-flux relation is linear and described by

$$\sigma = k(F - C_x) \tag{4.5}$$

Where the gradient of the relation is given by k and C_x is the intercept on the x-axis. Non-zero intercepts have previously been widely observed. Gleissner et al. (2004) found both positive and negative x-axis intercepts in the rms-flux observations from Cygnus X-1, possibly indicating the presence of two components within the light-curve.

4.2.4 Testing for good results

In order to evaluate the rms-flux relation for each individual observation we employed a method similar to that used in Gleissner et al. (2004), using Kendall's rank correlation coefficient, τ (Press et al., 1992), in addition to the χ^2 test to evaluate the fit. Kendall's tau can test for the trend which the bulk of points follow without being heavily affected by outliers, as long as the number of points is sufficient. Due to the lower levels of variability and count rates in data from the BHBs compared to observations of Cygnus X-1, less stringent limits were used to define good data than those used in Gleissner et al. (2004). Whilst their minimum threshold was set at $\tau_{min} = 0.9$ we have used $\tau_{min} = 0.5$. Observations with this value of τ still display a positive linear corellation but greater scatter is allowed around the mean. The assumption was made that if tau was significant at a level of $2\sigma_\tau$ the data were sufficiently strongly correlated. In addition to this we require the fit to be accepted using $\alpha < 0.003$ (i.e. not rejected at $3\sigma_{\chi^2}$.

In general the data were found to agree with the assumed linear model, with the majority of discrepant observations due to data at low count rates and/or with low fractional rms. A

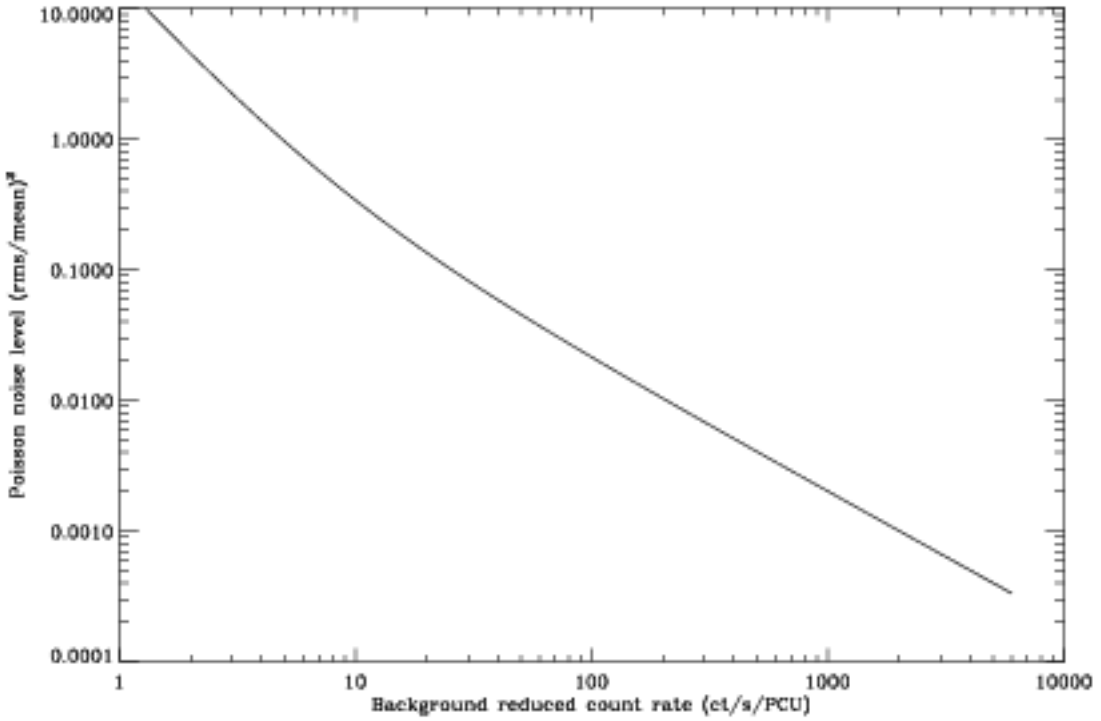

Figure 4.2: Estimated Poisson noise level against background reduced count rate for the range of count rates observed in the sample.

fractional rms of more than 3% was found to be necessary to measure an rms-flux relationship even at high count rates (assuming a background rate of approximately 7 ct/s/PCU) and a count rate of 100 ct/s/PCU the fractional rms of the noise level is 2.14%. Although this level drops rapidly with increasing count rate a significant amount of power above the noise is required to satisfactorily measure the rms. An estimation of the Poisson noise level in fractional rms units vs. an estimated background reduced count rate is shown in Figure 4.2 This means that some observations below ~ 500 ct/s/PCU (where the noise level drops to 0.4%) may still not have enough power for the source variance to be measured accurately in the frequency band, if the fractional rms is ~ 3%. Most observations with count rates lower than 100 ct/s/PCU are typically observed in a hard state where the fractional rms is generally higher than 10% (see e.g. McClintock & Remillard, 2006b) and so are less strongly affected by this limit. However, in a standard soft state the variability often drops drop below the required 3% fractional rms

level, therefore few observations of sources in this state are included in the following analysis.

Many of the rejected observations had low count rates which resulted in flux binned PSDs with low signal to noise and negative Poisson noise subtracted variances. Observations containing negative variance bins were therefore excluded from the sample. Short observations also limit the signal to noise for the flux binned PSDs as the number of points per flux bin are low. The length of good time required for a detected rms-flux relation varied according to the count rate and the level of intrisic variability within the observation, but more than 1 ks was generally found to be required.

4.3 Results

4.3.1 Ubiquity of the rms-flux relation

2178 observations of the sources listed in table 4.1 have been tested for a simple linear rms-flux relation. Of these observations 1159 displayed the 3% fractional rms required for the rms-flux relation to be measured. A good rms-flux relation as defined by the criteria set out in section 4.2.4 was observed in 676 of these observations.

Observations where a positive rms-flux correlation was not observed were inspected indvidually in order to screen out any obvious reasons for the non-detection. If the power spectral shape alters significantly over the course of an observation then the rms-flux relation will also change, this can cause a 'wavy' rather than strictly linear function to be observed, such as those shown in figure 8. of Gleissner et al. (2004). The flux-binned PSDs of long, bright observations which deviated significantly from a positive linear rms-flux correlation were inspected for any shape change over the course of the observation. In some observations plotting the individual flux binned power spectra for each point in the rms-flux relation, revealed QPOs

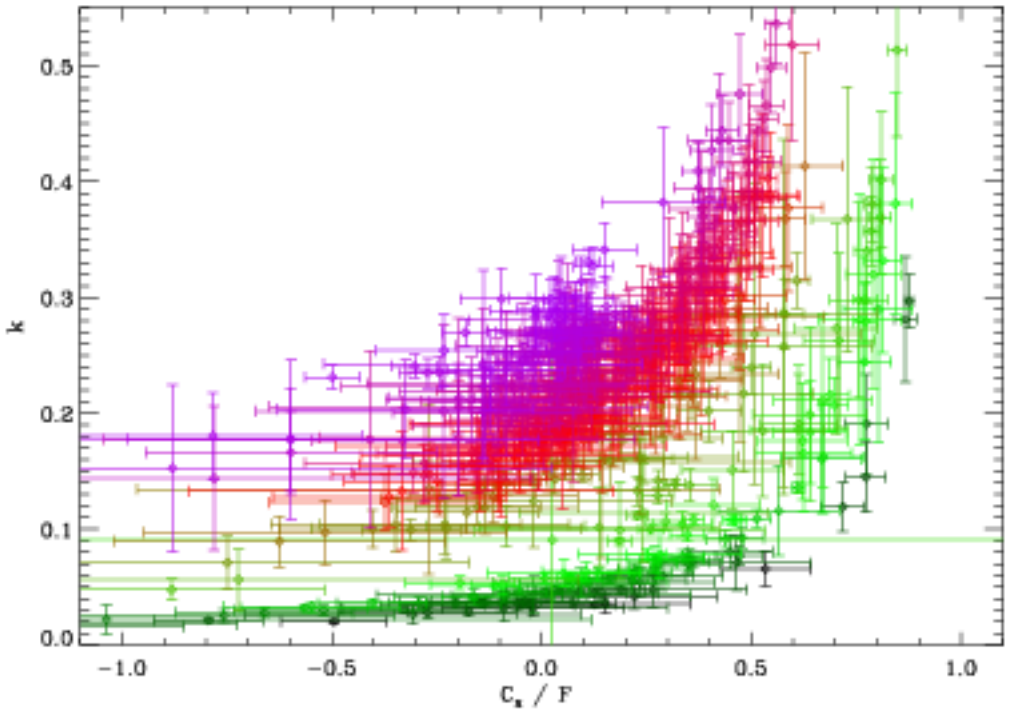

Figure 4.3: Results for all good rms-flux relations. The colours correspond to the fractional rms of the point, with purple highest and dark green lowest.

shifting with flux in either frequency or amplitude over the course of the observation, similar to those discussed in Chapter 6. In other cases it was apparent that the shape of the whole power spectra was evolving with flux. No examples of non-linear or negatively correlated rms-flux relations were found within the sample which could not be explained by one of the above reasons. Aside from these cases the rms-flux relation appears to be ubiquitous in the broad-band noise from BHBs.

Figure 4.1 illustrates observations of the rms-flux relation across a range of different states and sources, from the low-hard to a soft-intermediate state. The range of gradients and x-intercepts observed are representative of the range for these parameters found throughout the sample.

Figure 4.3 shows the gradients against the intercepts for all sources within the sample. As the x-intercept (C_x) is dependent upon source count rate the values plotted are shown as a fraction

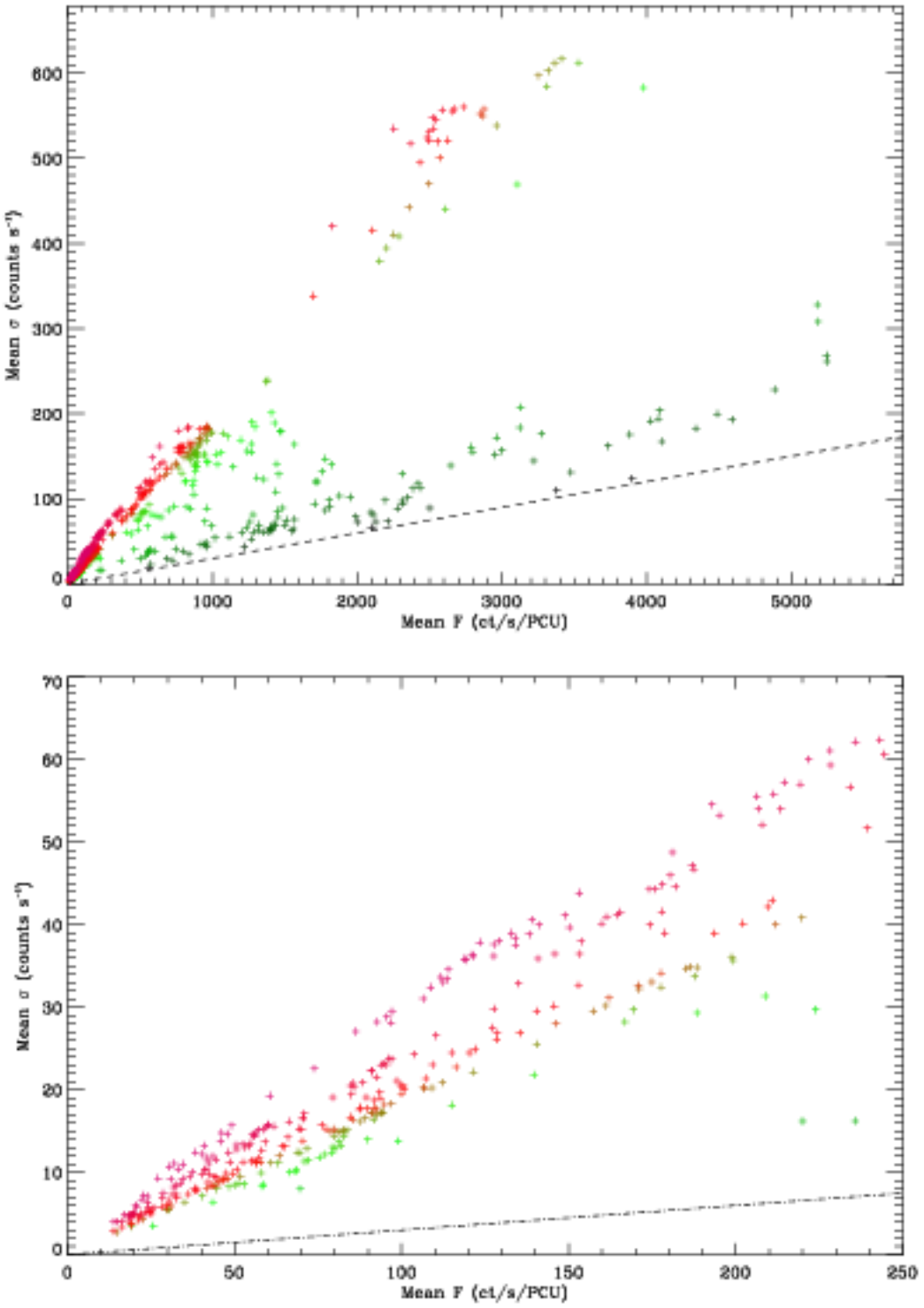

Figure 4.4: *Top*. Long term rms-flux results for all good rms-flux relations. *Bottom* As *Top* but concentrating on lower values. The dotted line plots the lower limit on detection for the rms-flux relation – 3%fractional rms. The colours represent the fractional rms of the points, where purple is the highest values and dark green is the lowest.

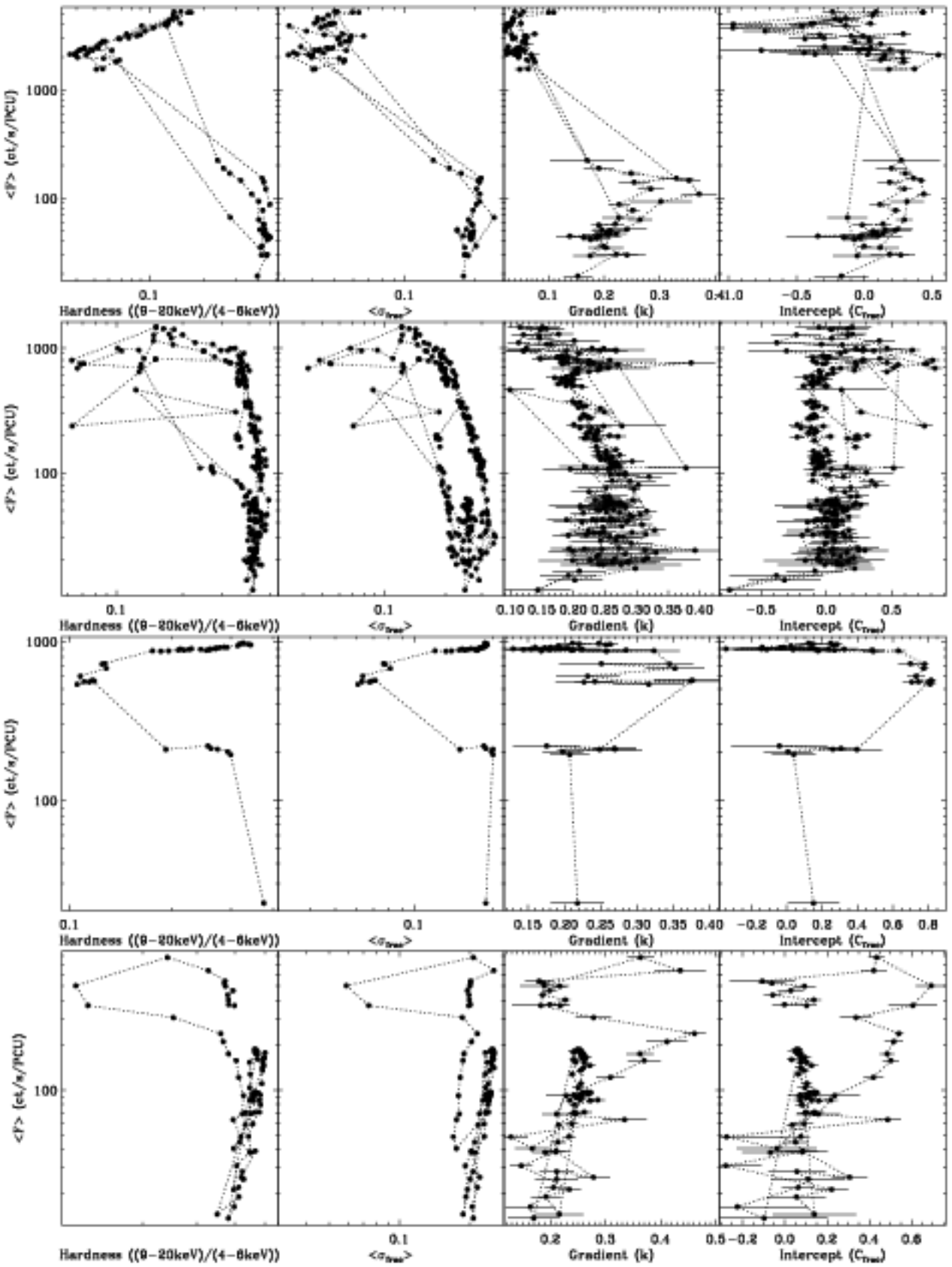
<F> (ct/s/PCU)
1000
100
0.1
Hardness ((9−20keV)/(4−6keV))
<σ_rms>
Gradient (k)
Intercept (C_rms)
−0.5
0.0
0.5
0.10 0.15 0.20 0.25 0.30 0.35 0.40
0.15 0.20 0.25 0.30 0.35 0.40
−0.2 0.0 0.2 0.4 0.6 0.8
0.2 0.3 0.4 0.5
−0.2 0.0 0.2 0.4 0.6

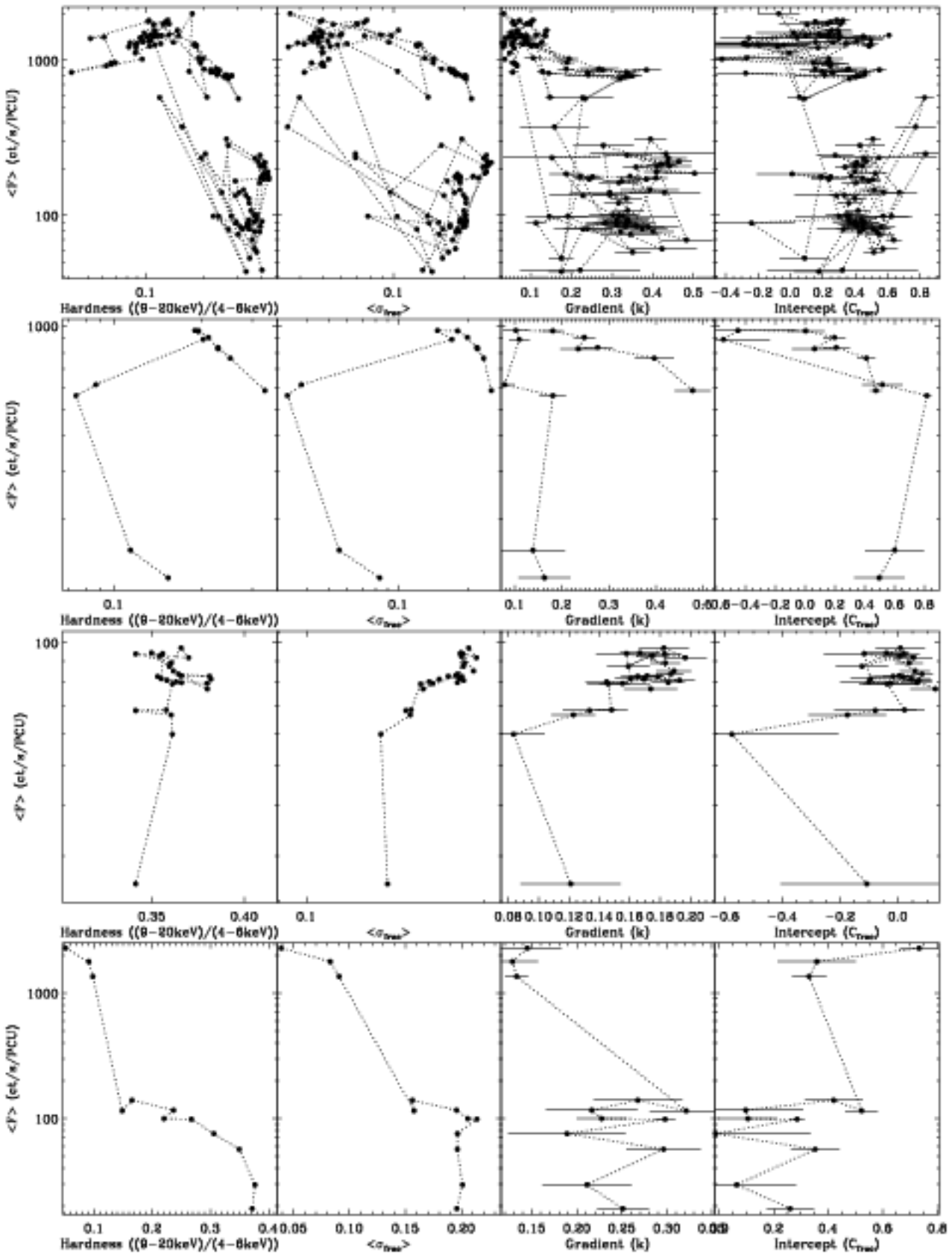
<F> (ct/s/PCU)
Hardness ((9−20keV)/(4−6keV))
<σ_true>
Gradient (k)
Intercept (C_true)

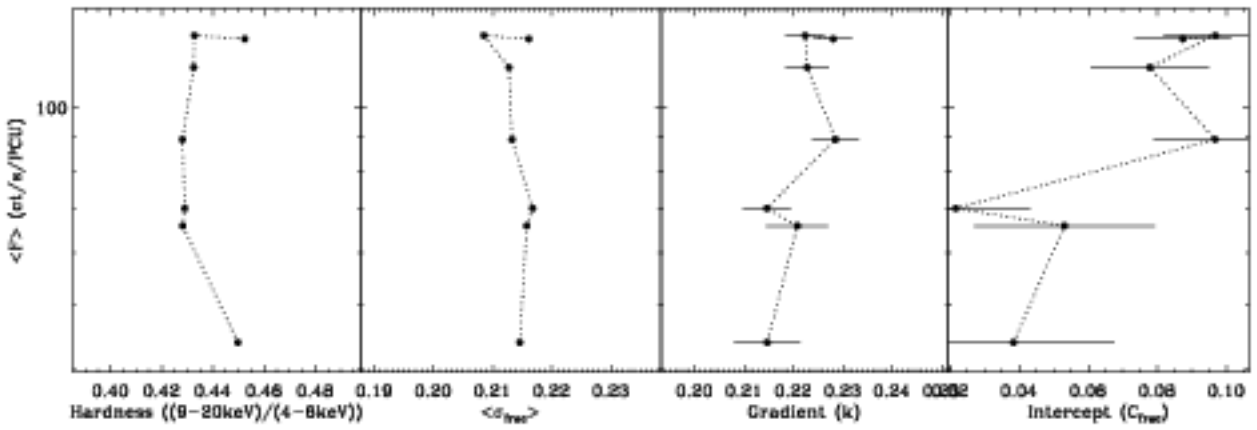

Figure 4.5: Hardness ratio, fractional rms, Gradient and Intercept vs. Count rate for all sources. From top to bottom- A) GRO J1655-40 B) GX 339-4 C) XTE J1650-500 D) XTE J1550-564 E) H1743-322 F) XTE J1859+226 G) XTE J1118+480 H) 4U 1543-475 I) GS 1354-64

of the mean count rate over the observation (the fractional intercept – C_{frac}), this allows the parameters from all sources in all states to be compared directly. There initially appears to be a few distinct paths within this plot, these can be easily explained if we re-write the gradient as

$$k = \frac{\langle \sigma \rangle}{\langle F \rangle - C_x} \tag{4.6}$$

In this case the value of the gradient may be interpreted as the fractional rms of the observation modulated by the intercept on the x-axis, if $C_x = 0$ then $k = \sigma_{frac}$ (where σ_{frac} is fractional rms). It is therefore intercept which is perhaps the most useful property. With a zero intercept the gradient is entirely governed by the fractional rms. With the inclusion of an offset on either axis the gradient is altered. Observations with the same overall fractional rms but different intercepts (C_x) will show rms-flux relations that pivot around a common point, meaning either steep or shallow gradients may arise from observations with the same mean rms and flux. When k is plotted against $C_x/\langle F \rangle$ then the changes in C_x and $\langle F \rangle$ work to produce the observed curves: $k \to \infty$ as $C_x/\langle F \rangle \to 1$ and $k \to 0$ as $C_x/\langle F \rangle \to -\infty$. The lower the curve on Figure 4.3 the lower the fractional rms of the observations. As fractional rms is well known to be related to source state (see e.g. McClintock & Remillard, 2006a) then the position of points on

the k vs. $C_x/\langle F \rangle$ diagram provides a link to the energy spectral properties of the observation.

Whilst the paths on this plot are therefore just contours of different fractional rms values, the new information that it does display is the full range of intercepts and gradients observed within the sample. Almost all possible parameter space allowed by the observed fractional rms values is covered at some point. It is also apparent that C_x is less well constrained at negative values than at positive ones, this is partly an artefact of the fitting, by nature negative intercepts are further from the actual observed rms-flux values than positive ones and therefore the point where the fitted line intercepts the x-axis is less certain. The range of intercepts and gradients observed within the sample is striking, particularly when compared to those observed by (Gleissner et al., 2004) from Cygnus X-1. Whereas their figure 5 indicated only a few observations with negative x-intercepts in the softer states and none in hard states, we observe a full range of positive and negative C_x values over a range of spectral colours. Explaining the position of points with the same fractional rms value on the $k - C_x/\langle F \rangle$ plot could lead to a deeper understanding of the processes creating the variability within the source.

4.3.2 Long term rms-flux relation

In a similar manner to Gleissner et al. (2004) the long-term rms-flux relation is plotted for all of the sources in the sample by taking the mean rms and flux values for each observation in the 1-10 Hz band. Each of these points again represent a measurement of the fractional rms of each observation, but it is interesting to observe how the rms and flux develop over long timescales and whether a linear relationship is still visible. The rms-flux relation measured here relies on the PSD remaining the same shape in the 1-10 Hz frequency band. Intermediate states show rapid changes i.e. QPOs or broad band noise components shifting in frequency, so the long term relation in these states is not representative of those observed when the PSD shape remains approximately stationary. In contrast evolution of the power spectra within the

hard state occurs mainly below the 1-10 Hz range and although the shape does not remain completely stationary it is more suitable for this comparison.

In Cygnus X-1 linear rms-flux relations were observed in the long-term rms-flux relationships in both the hard and softer states. Figure 4.4 shows the mean rms and flux values for all good rms-flux observations within the sample. The lower edge of this plot is artificially introduced by the requirement that there be at least 3% fractional rms within the 1-10 Hz frequency band in order to measure the rms-flux relation, so there is a wider range in the lower fractional rms soft state observations than appears on this plot. However, the relations for individual outbursts appear to be remarkably linear over a wide range of count rates, and there is distinct similarity in those observed between different sources. The agreement in these paths over repeated outbursts of GX 339-4 has been remarked upon in Muñoz-Darias et al. (2010) and we return to this point in section 4.4.1. This plot also clearly shows the sharp drop in fractional rms over a few observations within the transition from the HIMS through the SIMS to soft states, seen in the points which lie in between the hard (upper) and soft (lower) state rms-flux relations. Further differences between the rms-flux relations over the course of the outbursts are discussed in the following section.

4.4 Discussion

The rms-flux relation appears to be ubiquitous for broad-band noise in a large sample of observations from bright BHBs. This extends the study of the rms-flux relation in binaries to a much wider range of states, luminosities etc.

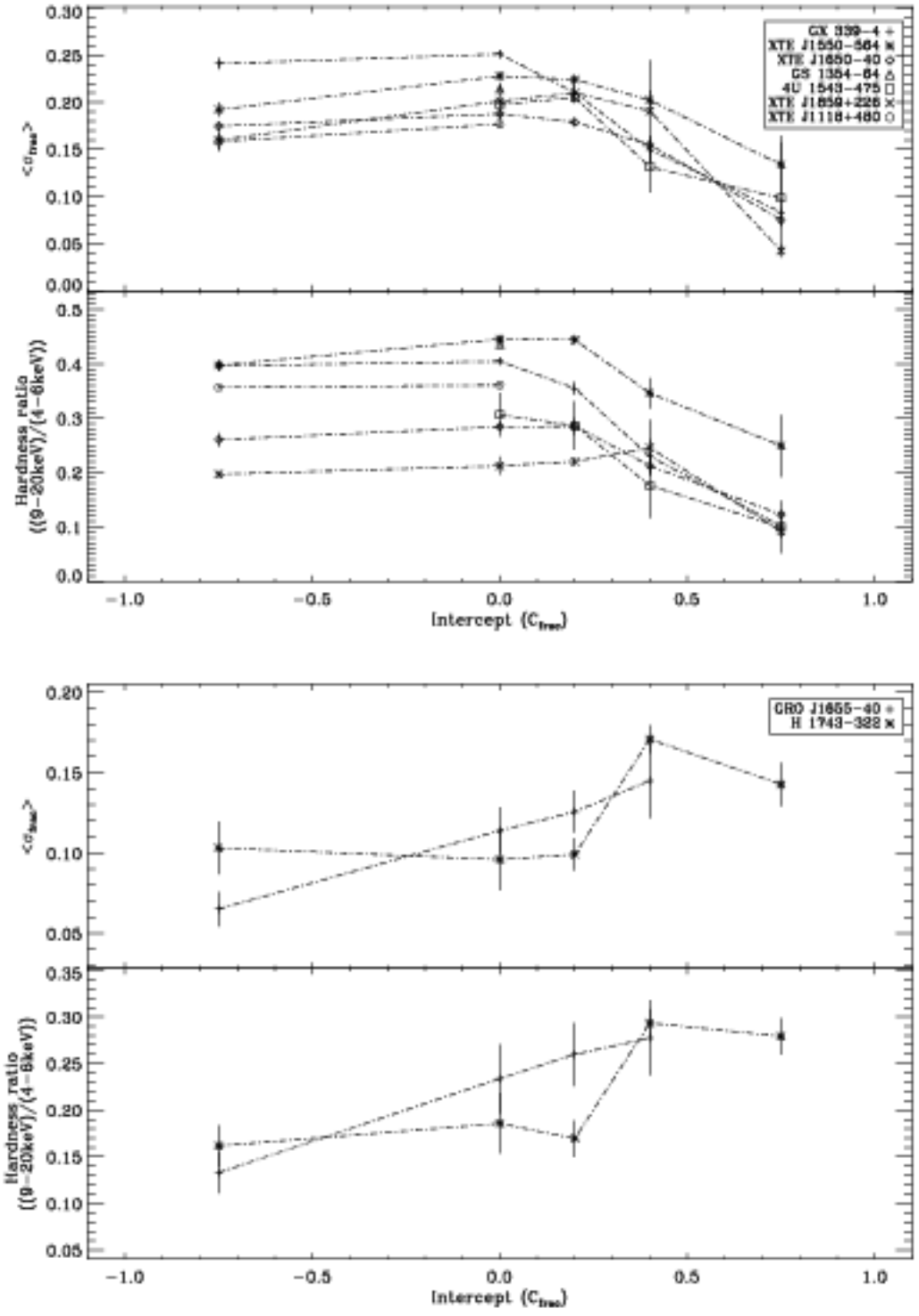

Figure 4.6: Intercept vs. fractional rms for two example sources. *Top:* H1743-322, *Bottom:* XTE J1650-500

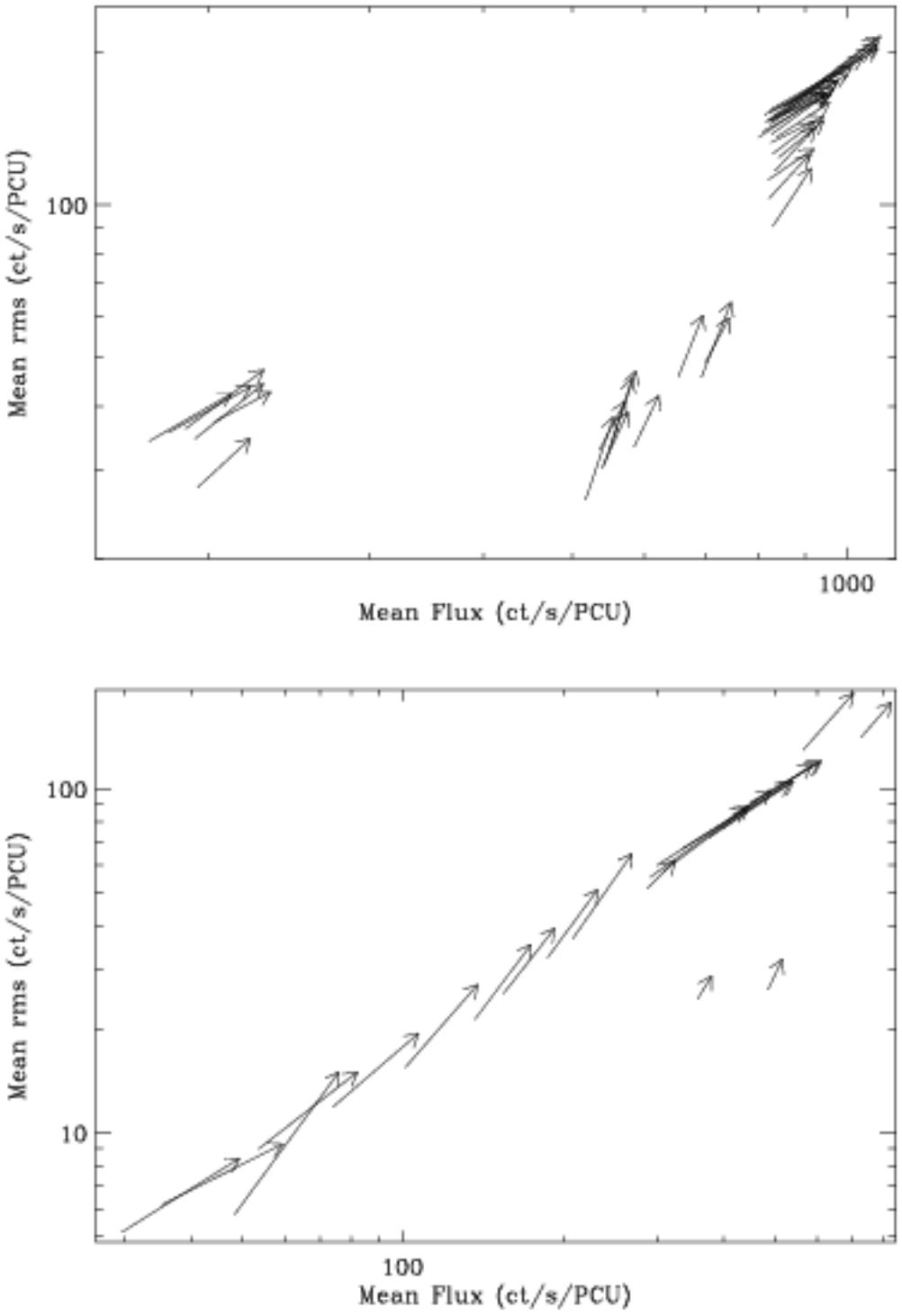

Figure 4.7: Long term rms-flux relations with arrows indicating the direction of the rms-flux relation over short timescales. *Top:* 2001 outburst of XTE J1650-500 *Bottom:* 2000 outburst of XTE J1550-564

4.4.1 Evolution of rms-flux relationship with BHB state

Gleissner et al. (2004) noted a distinct difference between the behaviour of k and C_x in different states of Cygnus X-1, in the softer states k was generally found to be lower and C_x had a much wider range of values than those observed in the hard state.

Figure 4.5 shows the evolution of the hardness ratio, fractional rms, gradient (k) and intercept (C_{frac}) for all sources. The x-intercept is again shown as a fraction of the mean count rate, allowing for comparison between different sources and different states of the same source.

As discussed in Chapter 1 the state of a source is usually identified based on a combination of its luminosity, timing properties (the power spectrum) and energy spectrum. The most important single diagram currently in use for diagnosing and tracking the evolution of states in the hardness intensity diagram (HID). The outbursts of transient black hole systems tend to follow a similar "q" shape path around this diagram (Homan et al., 2001; Belloni et al., 2005; Belloni, 2010b) beginning in a low/hard state, evolving through hard then soft intermediate states to the soft (thermal dominated) state, before changing back to the hard state via lower luminosity intermediate states. The HID itself is a powerful tool based on only the source intensity (in a particular X-ray band) and a very crude indicator of the energy spectral shape, with no explicit dependence of timing properties. But as discussed in Chapter 1 the timing properties of these objects evolve as clearly, if not more clearly than the energy spectral properties do. For more details see Belloni (2010) and references therein.

It is already well-known that the fractional rms (in the usual 2–20 keV X-ray band) is lower in the soft than hard state. In Figure 4.5 (second panels) we show a new diagram – the rms intensity diagram (RID) – the natural variability counterpart to the HID, which shows the intensity against fractional rms amplitude in the 1–10 Hz band. There is a remarkable similarity between the HID and RID. The RID is of course very similar to the long-term rms-flux plot in Figure 4.4, indeed it is simply a geometric transformation of that plot and contains the same

information. Similar diagrams were shown for GX 339 − 4 by Muñoz-Darias et al. (2010), and clearly demonstrate that the position on the RID is related directly to the source state. This demonstrates that variability is every bit as strong an indicator (or diagnostic) of outburst evolution and states as the energy spectrum, because the two are extremely well correlated.

That said, the RID and the HID do not have identical shapes (although the mapping between the two is very close). Some features are not present in both plots – for example, the RIDs for both GX 339-4 and XTE J1550-564 show separate paths in the RID which are not apparent in the HID. In the case of GX 339-4 the start of the outburst and return to quiescence are along separate paths in the RID. This behaviour is observed over repeated outbursts but occurs at very similar values of the hardness ratio and is therefore hidden in the HID. There is also a third path, followed when the source flux rises from quiescent levels but then returns without going into a full outburst. Similarly in XTE J1550-564 the return to the hard state following an outburst where state changes have occurred, is along a different route in the RID to that observed for outbursts when the source remains in the hard state. In the three hard outbursts the source rises and decays along very similar paths of fractional rms. Again these routes are much harder to discern on the HID.

Conversely, there are features visible in the HID which are not as clear in the RID. For instance there are many good observations of GRO J1655-500 taken when the source was in an anomalous soft state; two separate types of power spectra are visible whilst the source is in this state (see e.g. 4.1e and f). Those which display a typical soft state shape (i.e. 4.1f) have a softer energy spectrum than the observations which are more intermediate (i.e. 4.1e), however the fractional rms in the 1–10 Hz range is very similar for both and this difference can only be observed in the HID. The use of both of these diagrams in conjunction allows for a strong identification of source state without the need to study the energy or power spectra individually.

For GX 339-4, XTE J1550-564 and XTE J1650-500 the classic 'Q' shape of the hysteresis is replicated by it over the course of the outburst (although H1743-322 also has a large number of good observations, the analysis is more complicated as it shows both HIMS and soft state observations at a similar hardness ratio, the power spectra also suggests that there are few observations in a true hard state), the intercept appears close to zero in the hard state, but becomes strongly positive as the source transitions into the HIMS before moving back again. This behaviour is seen in at least 3 repeated outbursts of GX 339-4 which all follow remarkably similar paths in both the hardness and rms - intensity diagrams. In contrast the high flux observations of GRO J1655-40 show a wide range of intercepts including ones which are strongly negative, however the power spectra indicate that the source is in an anomalous soft state (Belloni, 2010a), the difference between the intercepts observed in other sources at high fluxes may therefore be state related. The observations of GRO J1655-40 in the hard state and HIMS still display similar strong positive intercepts observed in other sources. This can be observed in the lower flux (< 500 ct/s/PCU) observations in Figure 4.5. The appearence of intercepts close to zero in the hard state rising to strong positive values in the HIMS and then displaying a wide range of values, including strong negatives, in the soft states is replicated for other sources in the sample.

In order to test the behaviour of C_{frac} according to different states and power spectral behaviours, σ_{frac} and the hardness ratio have been binned up according to C_{frac} for each observation to test for any significant deviations. The bins were chosen according to the distribution of C_{frac} within the sample and are therefore uneven, the distribution of fractional intercepts is concentrated mainly between -0.1 and 0.5. In Figure 4.6 the upper plot shows these binned mean values for all objects where all good observations are of the hard states within the sample. The bottom plot shows this for the two sources with observations additionally in an anomalous soft-state and fewer in the HIMS. The sources with hard state spectra all show similar behaviour, observations with intercepts close to zero tend to be those with the hardest energy spectra and the highest fractional rms. Those with strong positive fractional intercepts

are the softest and have the lowest fractional rms, supporting the interpretation that C_{frac} gets stronger and more positive as the source moves further into the HIMS. All sources with more than two bins show a difference between the peak and the final point which is significant at a 3σ level. Although there are only two sources with observations in the soft states, their behaviour appears to be different. There is a wider spread of hardness and fractional rms values within each point, in the case of H1743-322 observations with strong positive intercepts are observed with the highest fractional rms values, although these are still lower than those observed for the sources with all observations in a hard state. We evaluate the effect of the shape of the power spectra on the rms-flux relation in Section 4.4.3 through simulations.

Figure 4.7 shows the mean rms-flux plots for the example outbursts using arrows to denote the gradient of individual rms-flux relations. The example outbursts both show this pivoting effect for observations of similar fractional rms. In the case of the 2001 outburst of XTE J1650-40 this behaviour is observed as the source transitions from the hard state into the hard intermediate state, in constrast it is visible in the 2000 outburst of XTE J1550-564 in the return from the hard state towards quiescence.

In Figure 4.5 similar state related behaviour is not as clearly visible for the gradient but may still be explained when it is considered in relation to the fractional rms and the intercept. As the gradient is effectively a measure of the fractional rms, an rms-flux relation intercepting both axes at zero has a gradient equal to the fractional rms within the relevant frequency band. This is clearly demonstrated in the intensity plots for GX 339-4, as the count rate rises in the hard state the intercept remains close to zero but the fractional rms in the 1-10 Hz band decays. Correspondingly the gradients of the rms-flux relations are observed to gradually flatten, from $k = 0.25$ to $k = 0.15$.

The rms-flux relations over the course of an outburst may be strongly altered by sharp features, such as QPOs, moving in to or out of the frequency band. If the feature is stationary over the

course of the observation but moves into the band between consecutive observations there will be a clear increase in the rms within the frequency band. This can be seen in the observations of XTE J1550-564: there is a jump in both the fractional rms and the gradient as the count rate increases in the hard state, this increase is linked to the strong QPO feature moving into the 1-10 Hz frequency range. If the feature is not stationary then it can cause other effects, if the feature is strong enough the relation may no longer appear to be linear, or it may artificially flatten or steepen the gradient. The effect of a strong QPO on the gradient is discussed in Chapter 6 for the 1998 outburst of XTE J1550-564 (for this reason this outburst is excluded from figure 4.5), and the 1999 outburst of XTE 1859+226. These effects must be considered when analysing the rms-flux relation within an observation, they will be particularly visible in the HIMS where any type C QPO features are typically visible in the 1-10 Hz frequency band.

Figure 4.8 shows the gradient and intercept in direct comparison with the hardness ratio. The different state-dependent behaviours are again clearly visible. Strong deviations from the expected gradient for these observations can be identified through comparison with the fractional rms in the 1-10 Hz frequency band, the ratio of fractional rms to gradient gives an idea of the size of the intercept. Particularly well constrained negative intercepts are observed in GRO J1655-40, an example of which can be seen in Figure 4.1f. These observations with strong, well constrained, negative x-intercepts seem to be limited to a particular spectral colour with a HR between $\sim$ 0.07-0.15 and they all have similar power spectral shapes to those observed in 4.1e or 4.1f. In simple terms the large negative intercepts observed represent times when the flux change is larger than the change in the rms, creating very flat gradients. On the most basic level this could be explained by a minimum of two components within the lightcurve, both varying, with either one or both obeying the rms-flux relation. In this case the two components combine to create a linear rms-flux relation with a flatter gradient than would be predicted from the combined fractional rms. We discuss evidence of frequency dependence for the rms-flux relation in section 4.4.2 with particular reference to power spectra in these states.

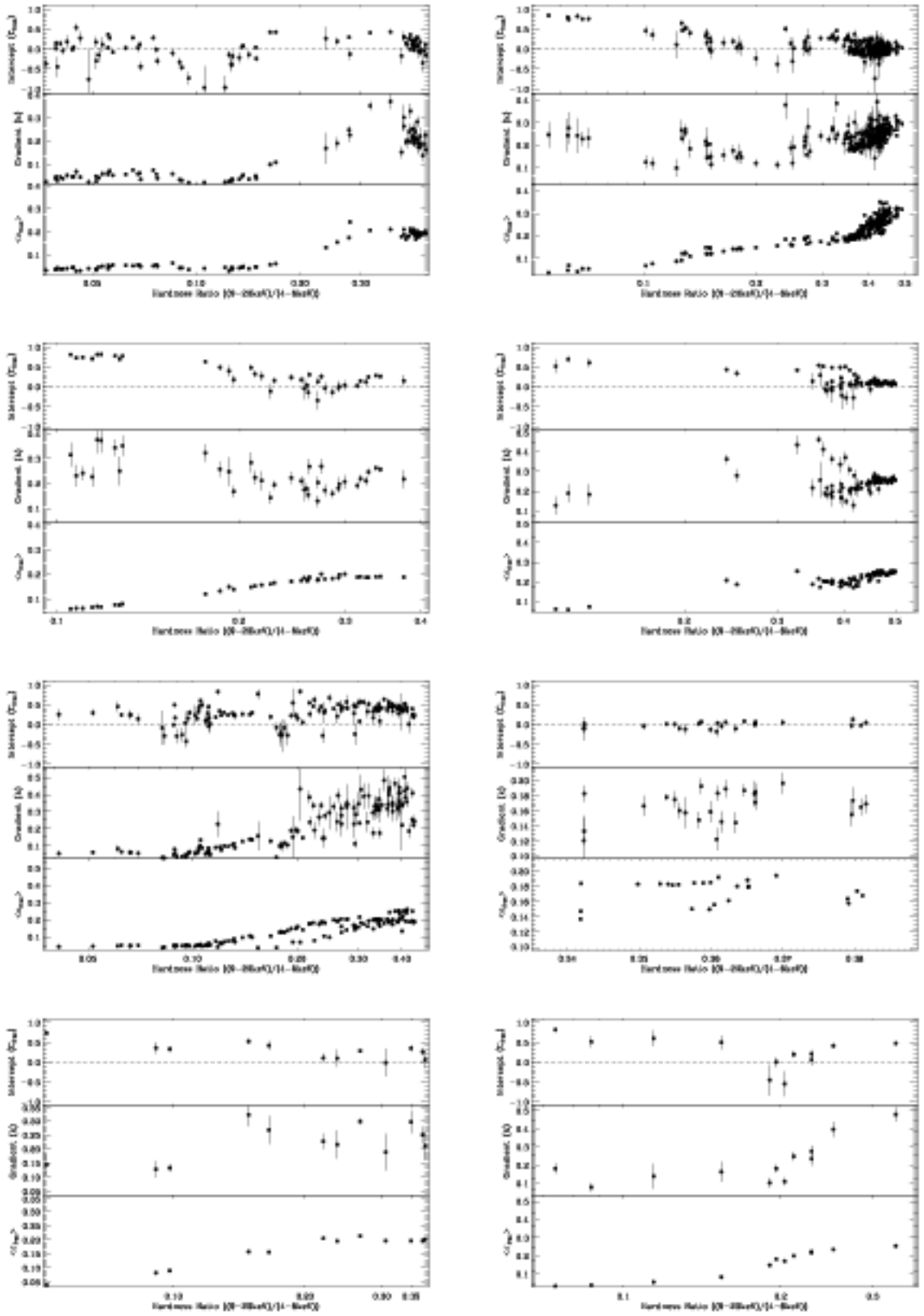

Figure 4.8: Hardness ratio vs. Intercept, Gradient and fractional rms of all sources with more than ten good observations. *Top left:* GRO J1655-40, *Top right:* GX 339-4, *Second row left:* XTE J1650-500, *Second row right:* XTE J1550-564, *Third row left:* H1743-322, *Third row right:* XTE 1118+480, *Bottom left:* 4U 1543-475, *Bottom right:* XTE 1859+226

Figure 4.8 also demonstrates that the hardness ratio alone does not govern the behaviour of the rms-flux relation for example XTE J1550-564 shows quite different behaviour at the same hardness ratio. This source has gone through two outbursts which have shown distinct spectral changes (in 1998 and 2000, only the outburst from 2000 is shown here due to the strong effect of the QPO on the rms-flux relation in 1998) and then a series of three outbursts whilst remaining in the hard state. In these hard outbursts the hardness ratio and fractional rms both slightly increase at the highest fluxes (see Figure 4.5) but the intercept remains close to zero and the gradient thus corresponds to the fractional rms. The power spectra remains in approximately the same shape over the entire course of these hard outbursts, but the amplitude rises with the flux and the behaviour of the rms-flux relation is repeated on both the rise and the return to quiescence. In contrast the outburst in 2000 shows clear evolution in the power spectra, as the source returns towards quiescence, with a similar hardness ratio to the hard outbursts, the QPO gradually moves to lower frequencies. The rms-flux relation begins with a steep gradient and strong positive x-axis intercepts ($C_{frac} > 0.4$), which then move back towards zero. This difference in power spectral shape between observations of the same source with similar count rates and hardness ratios, may help explain the changes in the rms-flux relation. This idea is explored later in section 4.4.3.

As the QPO is always within the 1-10 Hz band in the HIMS (if it is visible), and it is known to sometimes show a non-zero rms-flux relation (see Chapter 6), it may therefore be reasonable to suggest that some apparently state-dependent properties, such as the high flux intercepts observed in the HIMS, are the result of the QPO either moving during the observation or simply not obeying a positive linear correlation. However analysis of the rms-flux relation in the 0.3-1 Hz frequency band which contains the QPO at different times reveals identical behaviour. Although we cannot exclude the possibility that sub-harmonics or other components relating to the QPO are not causing this behaviour in the lower frequency band, it is suggestive that this may be linked to the flux-dependent behaviour of the wider broad-band noise rather than that of the QPO.

4.4.2 Frequency dependence of the rms-flux relation

In order to evaluate the frequency dependence over a wide frequency range power spectra were measured for 100 s segments of lightcurve and grouped into four flux bins. The averaged PSDs from the highest flux bin were compared with that from the lowest. Figure 4.9 shows the results for the six example observations from Figure 4.1. We evaluated the constancy of the PSD shape by fitting the ratio of high and low flux PSDs with a constant, and the χ^2 statistic used to evaluate the quality of the fit. If this differed by more than 3σ from the expected value then the observations were subject to further investigation.

The ratio was fit up to 20.0 Hz, above this point some observations are dominated by Poisson noise (see e.g Figure 4.9f). Little evidence for frequency dependence was found in most of the observations: in total only 20 of the good observations were identifed as having obvious frequency dependent differences between the PSDs from the upper and lower flux quartiles. Different binning was tested in order to eliminate possible spurious results caused by sharp features (e.g. QPOs) appearing shifted in frequency between the two power spectra. 15 of these observations were all from the 2005 outburst of GRO J1655-40 when it was in the anomalous soft state. The power spectra all show strong low frequency noise with a high frequency broad band component, an example of which is shown in Figure 4.1e. The two flux binned power spectra indicate that the broad band component shows a greater change in rms with flux than the power law. The observations with clear frequency dependence are not consecutive and the appearence of the power spectrum changes between this and the typical soft state shape. The power spectra in Figures 4.1e and f were taken almost exactly a day apart and show distinctly different behaviour, although the fractional rms in the 1-10 Hz band remains similar (3.7 % vs. 3.5 %). Fitting the average power spectra for these two observations indicates that the power law index measured below the bend which fits the soft state power spectrum, also fits the intermediate state spectrum below the peaked noise component, although it has a lower normalisation in the anomalous state spectra.

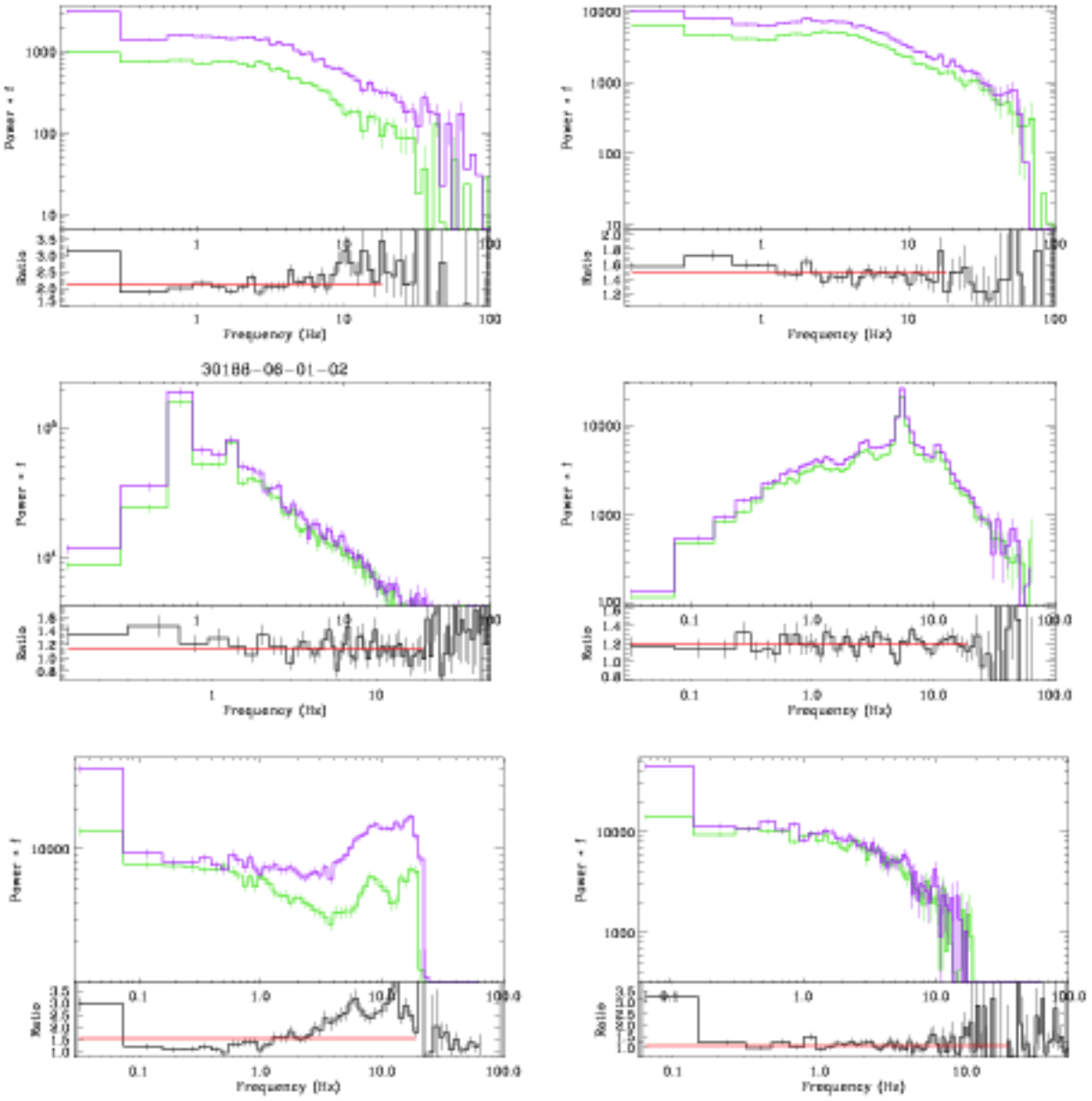

Figure 4.9: Examples of power spectra for the upper and lower flux quartiles. Observations used are the same as Figure 4.1 and are presented in the same order. These are normalised to the rms normalisation used to calculate the rms-flux relation, as defined in Chapter 2. For this reason the flux dependence is still clearly visible in the power spectra.

Similarly for the example in Figure 4.9f the upper and lower flux binned power spectra have been separately fitted using XSPEC to test if the change in power spectral shape can be mainly explained by the strength of the peaked noise components. The model used a bending power, plus two Lorentzians to model the high frequency broad band component and a separate narrow Lorentzian to model the very low frequency component, which can be seen in the lowest frequency bin of Figure 4.9f. This model gave a fit to both the high and low flux power spectra with good χ^2 statistics ($\chi^2 = 35$ and 47 respectively with 38 dof). The models used were broadly similar for both of the spectra. The main alteration was in the first broad lorentzian at high frequencies which was wider in the high flux spectrum, ($Q = 1.9$ compared to 1.0 in the low flux spectrum) respectively. Other than this the only difference between the two models was in the normalisation of the components. The change in the rms for the power law component between the high and low flux power spectra was 21% of the power in the high flux spectrum, in contrast both the combined Lorentzians for the high frequency peaked component and the Lorentzian for the lowest frequency component altered by 67%. A similar change in the different components with flux was repeated for the other observations. This suggests the existence of two separate components combining to produce the observed light curve, and might help explain the well constrained negative intercepts observed in the rms-flux relations in some power spectra from this state (see Section 4.4.1).

The other 5 observations which did not meet the criteria for inclusion (i.e. did not display a linear rms-flux relation) were generally found to contain components shifting in frequency over the course of the observation, sometimes outside the 1-10 Hz range. These shifts, which have in these cases still produced strong, positively correlated, linear rms-flux relations, demonstrate the importance of careful analysis of the power spectra when measuring the rms-flux relation. Small differences in the shape of the PSD, whilst not always drawing it away from linearity, may artificially alter the gradient and thus the intercept of the observed rms-flux relation and conclusions drawn from these observations will not be representative of the flux correlated changes in the amplitude of the otherwise stationary variability.

Table 4.3

Obs. Id.	Measured values		Simulated values	
	k	C_{frac}	k	C_{frac}
(1)	(2)	(3)	(4)	(5)
80135-01-04-00	0.253±0.003	0.066±0.008	0.274	0.0037
95409-01-12-00	0.197±0.003	-0.105±0.01	0.235	0.011
30188-06-01-02	0.36±0.02	0.45±0.02	0.29	0.29
70109-04-01-01	0.21±0.01	0.28±0.03	0.19	0.24
91702-01-63-00	0.041±0.001	0.13±0.03	0.035	0.005
91702-01-62-00	0.021±0.002	-0.7±0.2	0.037	0.004

The lack of clear frequency dependence in the rest of the sample is particularly interesting. The well constrained non-zero intercepts observed suggest that there are two or more components in the light curve (simulations in Uttley et al., 2005, suggest that more that ~ 5 components could draw the relation away from linearity). The fact that very little frequency dependence is observed in a sample of nearly 700 observations suggests that these components should either have the same rms-flux relation, or a very similar power spectral shape.

As the energy spectrum typically consists of two separate components which are known to have different levels of varability they could contribute to the rms-flux relation in different ways. In particular the thermal component which shows low levels of variability could cause the constant positive x-axis offset observed in some observations. The next section explores possible causes for the non-zero intercepts observed within the rms-flux relations.

4.4.3 Intercepts and gradients from simulations

Evaluating the expected rms-flux relation from power spectra with particular distributions may be carried out through simulations. Uttley et al. (2005) describe the method of simulating lightcurves with a positive rms-flux relation. This essentially involves simulation of a lightcurve following the method given in Timmer & König (1995) using a model power spectral shape and then exponentiating it. The near-ubiquitous observation of an rms-flux relation

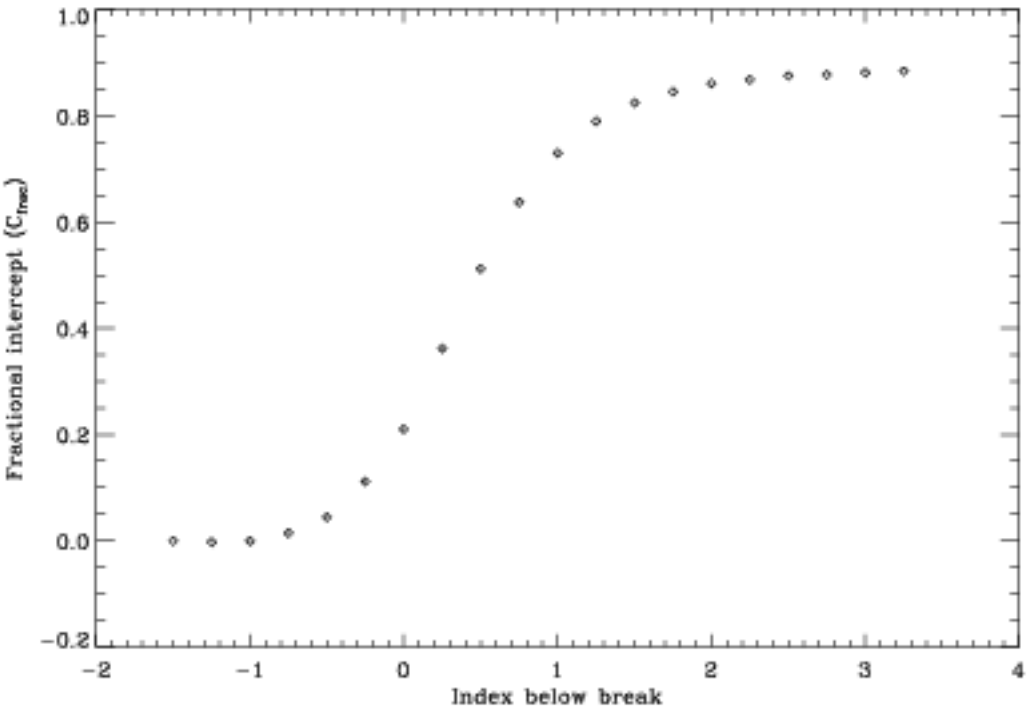

Figure 4.10: Fractional intercepts in the 1-10 Hz range for simulated lightcurved with a power spectral shape defined by a bending power law breaking at 3 Hz with an index above the break of -2. The index below the break is altered producing a fractional intercept which becomes stronger and more positive as the power law index increases.

supports models suggesting that the perturbations in the accretion flow multiply together over different timescales to create the final observed source lightcurve, exponentiation recreates this process: the exponential of a sum of sinusoids is equivalent to the product of many small sinusoidal variations. In order to test the expected intercepts from various power spectral shapes the example power spectra from Figure 4.1 were fitted XSPEC, 100 lightcurves were simulated from the best fitting model and the rms-flux relation meaured in the manner described previously. The expected intercepts for each observation are shown in table 4.3, along with the observed parameters. For observations in the HIMS strong fractional intercepts emerge from the simulations. The observations in the anomalous soft states both have strongly constrained negative intercepts which are not replicated in the simulations.

A gently bending power law with a range of low frequency power law indices, breaking at 3 Hz

to a index of -2, can be used as a very simplistic model to describe the evolution of the broad-band noise within the power spectra over the course of an outburst. 20 different bending power laws with low frequency indices ranging from -1.5 to 3.0 were used to simulate lightcurves and then exponentiated and the rms-flux measured. Typically a bending power law with a low frequency power law of ~ -1 breaking to ~ -2 is representative of the power spectra in the soft state (i.e. 4.1f). Low frequency power laws with positive or flat indices (α = 0 to VALUE) breaking in the 1-10 Hz frequency range can be rough representations of broad-band power spectral shapes in the hard states (see e.g. McClintock & Remillard, 2006a). The high frequency power law is often seen to remain constant (see e.g. Gierliński et al., 2008) so it remains fixed throughout. All power spectra are modelled with a mean fractional rms of 30 % in the 1-10 Hz frequency band. For each model shape 100 simulations are produced and the mean values of C_{frac} used.

Figure 4.10 shows these mean values of C_{frac} against the low frequency power law index for the model power spectral shape used. The results suggest that the expected value of C_{frac} remains at zero if the underlying broad band noise is not peaked. As the low frequency index rises above α =~ -0.5 the rms-flux relations become steeper than expected and a strong positive x-intercept is visible. This rises quickly between α = -0.5 $\rightarrow$ 2.0 towards C_{frac} ~ 0.85, above this point (where the indices become steeper than those typically observed) the fractional intercept slowly approaches 0.9. The smaller the variance at low frequencies, the higher C_{frac} becomes. It is the power spectral 'colour' which is important, i.e. the lower the variance in the < 0.33 Hz band vs. the 1-10 Hz band, the higher the intercept. Observations with the strongest peaked broad-band noise in the power spectra are typically those from the HIMS, I noted earlier that the rms-flux relations for these observations have strong positive x-intercepts this result suggests that these intercepts and gradients can be reproduced in simulation and are therefore at least partly an effect of the multiplication of fluctuations from different timescales, rather than the product of additional components in the light curve. In fact for one of our example observations the expected rms-flux relation is reproduced within 1 σ errors.

What was not reproduced in simulations of single lightcurves, are the rms-flux relations for those examples with negative intercepts, particularly that observed in Figure 4.1f. The strength of the positive intercept in the observations from 4.1c is also not predicted by the simulations. This suggests that although some of the offsets observed may be explained as simply a feature of the multiplicative coupling of the propogating oscillations, there are still some additional components within the lightcurve causing these observed intercepts. What it also emphasises is that the expected values of the gradient and intercept are not $k = \sigma_{frac}$ and $C_x = 0$, the power spectra need to be modelled and the rms-flux relation simulated before the estimated expected values are known.

4.5 Summary

A large sample of observations from 9 transient black hole X-ray binaries have been tested for a linear rms-flux relation. In every observation with sufficient flux and intrinsic variability to measure the rms, and the PSD remained stationary a positive linear correlation was observed. Analysis of the sample revealed the following results:

- Long-term rms-flux relations for states with little alteration in power spectral shape within the 1-10 Hz band are clearly visible. These are similar to those observed in Cygnus X-1 (Gleissner et al., 2004) and show remarkable similarities both in repeating outbursts of the same source, and in the behaviour of different sources (i.e. Muñoz-Darias et al., 2010).

- A wide range is observed in the flux intercept (C_x) and there is a strong link between the observed x-intercept and source state. Hard states have x-intercepts close to zero, strong positive intercepts are observed in the HIMS. Strong negative intercept seem isolated to the soft states and it is for observations in these states that the greatest range in C_x is

observed.

- There is little evidence for strong frequency dependence in the rms-flux relation apart from in the anomalous soft states where there may be two separate components in the light-curve appearing as different components in the power spectra.

- Simulations of light-curves with proscribed power spectral shapes can reproduce some of the strong off-sets observed in the HIMS. The intercepts appear to be linked to the lack of low frequency power observed in observations in this state.

Chapter 5

The rms-flux relation in a ULX

5.1 Introduction

X-ray timing studies of bright ULXs have shown some to display timing properties common to BHBs such as spectral breaks and quasi-periodic oscillations (QPOs) (see Strohmayer & Mushotzky, 2003; Strohmayer et al., 2007; Strohmayer & Mushotzky, 2009, and Chapter 3). However, it has also been suggested that both energy spectral and timing behaviour within ULXs may differ from those seen from BHBs and AGN (Stobbart et al., 2006; Goad et al., 2006; Gladstone et al., 2009, Chapter 3 of this Thesis). The low levels of variability seen in current long observations of ULXs with high count rates taken with *XMM-Newton* leaves only one promising source with variability which may be strong enough to detect an rms-flux relation: NGC 5408 X-1. This source has already been shown to display the kinds of timing features often seen in BHBs and AGN including quasi-periodic oscillations and power spectral breaks (Strohmayer et al., 2007; Strohmayer & Mushotzky, 2009). It has been observed in two separate long *XMM-Newton* ($>$ 100 ks) observations and is relatively bright (~ 0.8 ct s^{-1}). In this letter we analyse both observations for evidence of the rms-flux relation.

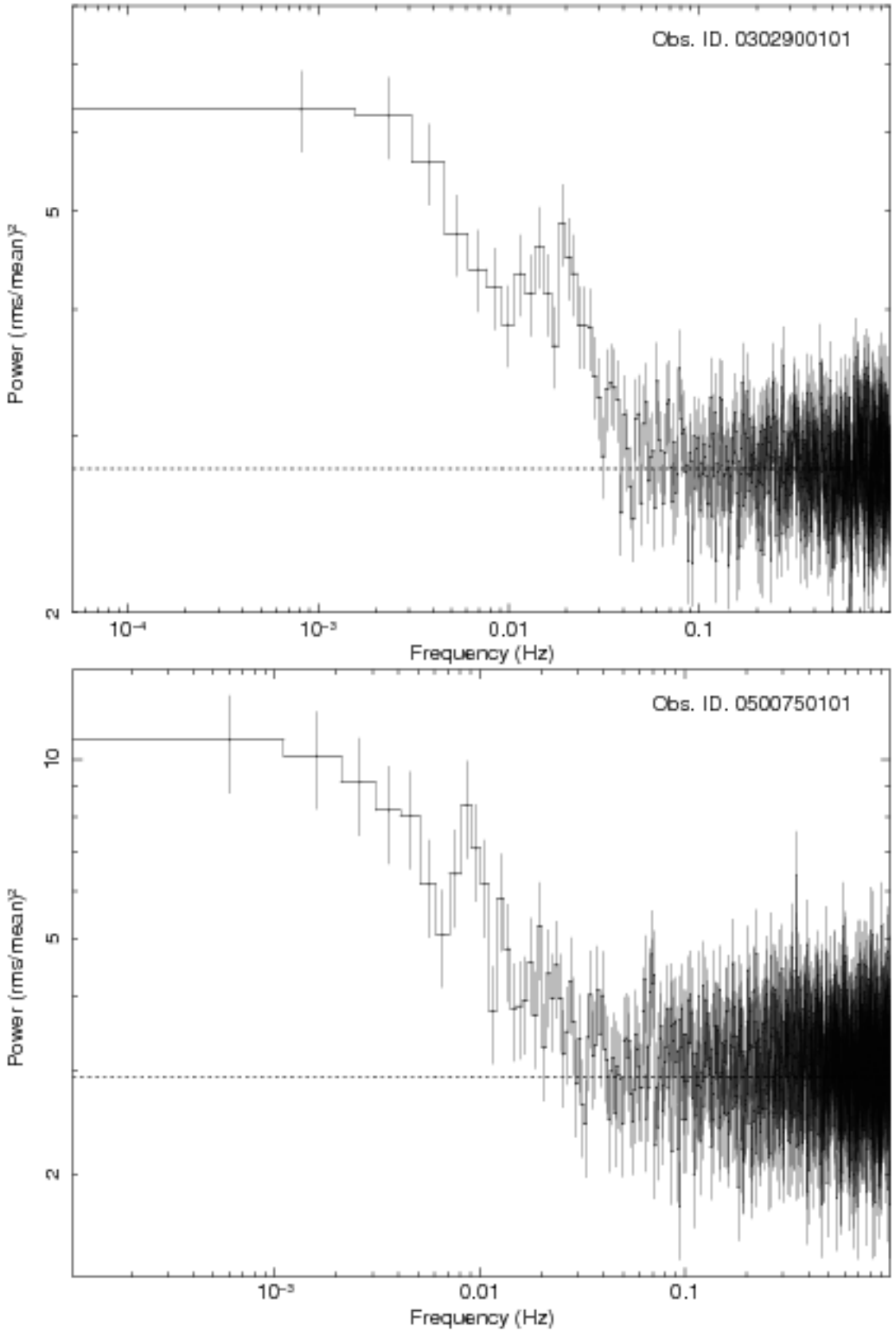

Figure 5.1: Power spectra for the two long *XMM-Newton* observations of NGC 5408 X-1, the QPO feature is clearly visible in both.

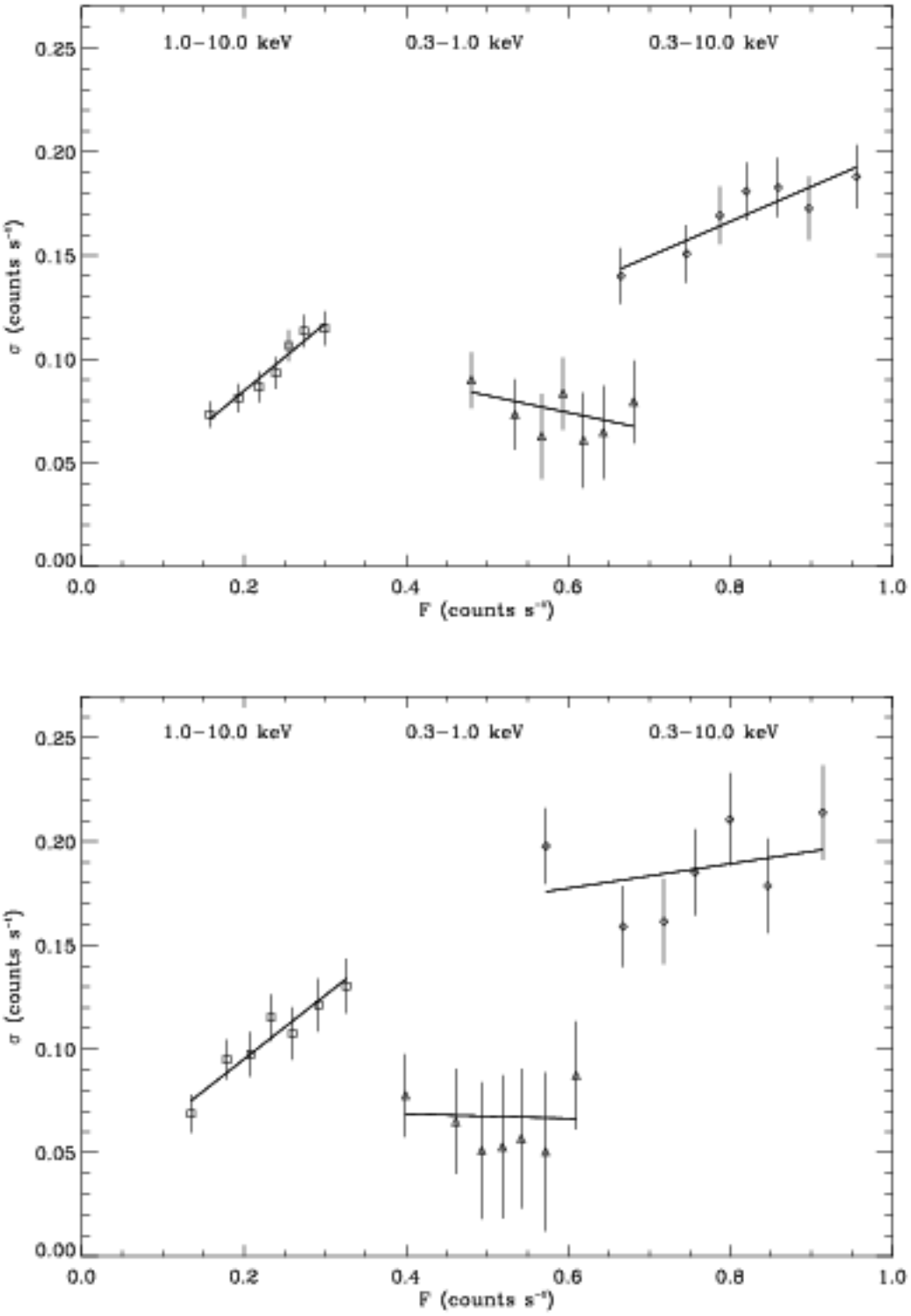

Figure 5.2: Rms-flux points for each of the three energy bands used in the analysis with 1σ errors. *Top*. obs. id. 0302900101; *Bottom* obs. id. 0500750101.

5.2 Data Analysis

We have used the two longest observations of NGC 5408 X-1 in the *XMM-Newton* archive (Obs. Ids. 0302900101 and 0500750101) taken on the 13th January 2006 and 2008 respectively. The data were extracted from the European Photon Imaging Camera (EPIC) pn camera only, as this provided the highest count rate time series. The pn was operated in full–frame mode for both observations. The data were extracted and reduced following standard procedures using the SAS version 7.1.0. In particular, source events were extracted from a 36 arcsec region centred on the X-ray source and background events from a rectangular region on the same chip as close to the source as allowable. The light curves were initially extracted in the energy band 0.3-10.0 keV and with time resolution of 73.4 ms (the frame time of the camera in this mode).

The careful removal of background flares is necessary for good timing analysis. Following the method used in Chapter 3: 82.2ks of good time were extracted from the 2006 observation, but only 34.5ks was extracted from the 2008 observation which was particularly affected by background flares.

Each observation was divided into continuous segments of 150s duration, and for each segment the mean count rate ($\langle F \rangle$ in units of ct s^{-1}) and the periodogram was calculated. The periodogram was found using absolute normalisation such that the sum over frequencies multiplied by the frequency resolution ($\Delta\nu$), gives the variance, the square root of which is the rms in absolute units (i.e. also ct s^{-1}) (Figure 5.1 shows the measured power spectra, but plotted in fractional rms units for direct comparison). The intrinsic randomness of the variability scatters the periodogram points randomly about the underlying power spectrum. In order to suppress these random fluctuations and get a reasonable estimate of the power spectrum as a function of flux the periodograms were averaged in flux bins. The 2006 and 2008 observations were binned such that each flux bin contained 60 and 30 segments, respectively (there are fewer

points per bin in the 2008 observation due to the smaller amount of good time). The variance over the $6-50$ mHz range was estimated by summing over the appropriate frequency range in each of the flux averaged periodograms. The Poisson noise level, which is approximately $2\langle F\rangle$ for each periodogram, was subtracted. The square root of the result is an estimate of the intrinsic rms of the source as a function of its flux, σ. Errors on each rms point were calculated using a more general form of the prescription used by Gleissner et al. (2004), namely propagating the variances of the individual periodogram points as they were averaged into flux bins and summed over the $6-50$ mHz frequency range (full details are given in Chapter 4). This range includes the quasi-periodic oscillations (QPOs) visible in both of these observations – excluding them would require segments of much longer timescales and hence limit the number of measured rms-flux points. The QPOs are seen at frequencies of 11.4, 19.8 and 27.7 mHz in the 2006 observation (Strohmayer et al., 2007) and 10.02, 13.5 and 6.0 mHz in 2008 (Strohmayer & Mushotzky, 2009). The analysis was repeated for soft band ($0.3-1$ keV) and hard band ($1-10$ keV) light curves. The resulting rms-flux data are shown in Figure 5.2.

Obs. Id.	Date	Energy (keV)	$\langle F \rangle$ (ct s^{-1})	N	k	C (ct s^{-1})	τ	p_τ	χ^2/dof	p_{χ^2}
(1)	(2)	(3)	(4)	(5)	(6)	(7)	(8)	(9)	(10)	(11)
0302900101	2006 Jan 13	0.3-10.0	0.82	7	0.17±0.06	-0.18±0.3	0.81	0.01	1.77/5	0.87
		0.3-1.0	0.59	7	-0.08±0.1	1.5±1.1	-0.23	0.45	1.7/5	0.88
		1.0-10.0	0.23	7	0.33±0.06	-0.06±0.05	1.0	0.001	1.46/5	0.91
0500750101	2008 Jan 13	0.3-10.0	0.75	7	0.06±0.07	-2.39±3.8	0.42	0.17	5.9/5	0.31
		0.3-1.0	0.52	7	-0.01±0.14	7.3±94	-0.14	0.65	1.56/5	0.90
		1.0-10.0	0.23	7	0.31±0.07	-0.11±0.07	0.91	0.004	1.99/5	0.85

Table 5.1: Results from fitting the rms-flux relation in three separate energy bands errors given are the 1σ errors on each value. (1) *XMM-Newton* Observation identifier; (2) Date of observation; (3) Energy band; (4) Mean count rate; (5) Number of points in fitting; (6) Gradient; (7) X-axis intercept; (8) Kendall rank correlation coefficient (τ); (9) p-value of τ; (10) χ^2 with number of degrees of freedom; (11) p-value of χ^2 fit.

5.3 Testing for the rms-flux relation

Following Gleissner et al. (2004) we tested the correlation between rms and flux using the Kendall rank correlation coefficient (τ). The results are given in table 5.1 and suggest a correlation is at least present in the 2006 data. Although not highly significant individually the correlation seen in the first and longest observation indicates that an rms-flux correlation could be present. The result for the second observation is less convincing. For comparison with the previous analyses (e.g. Uttley & McHardy, 2001; Gleissner et al., 2004) we fitted the resulting points in the full band with a linear function of the form $\sigma = k((F) - C)$ with k the gradient and C the intercept on the flux axis. The χ^2 values from the initial fit were acceptable, with p-values of 0.87 and 0.31 for the 2006 and 2008 bands respectively indicating a good agreement with a linear model.

Strohmayer & Mushotzky (2009) noted that below ~1 keV the QPO is no longer visible in the 2008 observation and that the 2006 observation displays a clear difference in the shape of the soft spectrum. For both the 2006 and 2008 observations a lower level of variability was detected in the soft energy band at 12% and 11% factional rms respectively, rising to 39% and 50% in the hard band. The strong energy dependence within the power spectrum appears to be reflected in the rms-flux relations taken at different energies: we find no strong evidence of a coherent rms-flux relation in the soft energy band, although a linear relation with an intercept at $C = 0.0$ cannot be excluded due to the large uncertainties (caused by the relatively low level of variability).

The parameters of the rms-flux relation in the hard band are broadly consistent between the 2006 and 2008 observations and so we performed a simultaneous fit to the two sets of rms-flux data to obtain tighter constants on the model parameters. The resulting χ^2 value was 7.36 with 12 degrees of freedom, indicating the strength of the similarity. Figure 5.3 shows the confidence contours for the parameters for this simultaneous fit in each of the two energy

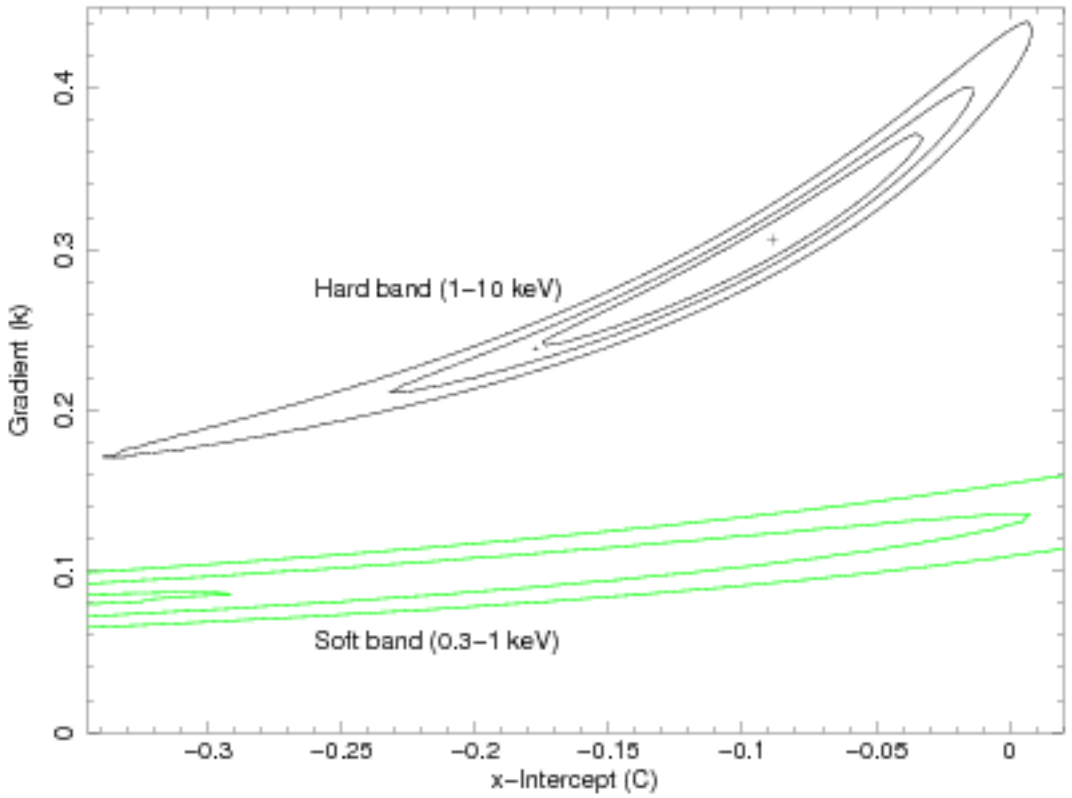

Figure 5.3: Contour plot of k against C for the hard band (1 − 10 keV, black) and soft band (0.3 − 1 keV, green) rms-flux relations. For each band the 2006 and 2008 observations have been simultaneously fitted. Contours are shown at the $\Delta\chi^2 = 2.30, 4.61$ and 9.21 levels which correspond to the 68, 90 and 99 per cent confidence regions for the two parameters.

bands. The best fitting intercept parameter (i.e the flux at which the rms drops to zero) is indeed negative – the 99% confidence interval for this one parameter ranges from -0.27 to -0.002 ct s^{-1}. As the Figure shows, the parameters for the hard and soft band are significantly different. It must be noted that because the gradient in the soft band is consistent with zero the contours for the soft band extend towards extremely large negative intercepts.

5.4 Coherence and time delays

We compared the variability in the two bands (0.3 − 1 keV, and 1 − 10 keV) by computing the coherence and time delay spectra from the cross-spectrum (see Vaughan & Nowak, 1997; Nowak et al., 1999; Vaughan et al., 2003b). If the Fourier amplitudes of the transformed lightcurves in the two separate energy bands are given by X_1 and X_2 respectively then the cross spectrum for frequency ν_j is $C_j = X^*_{1,j} X_{2,j}$. The phase difference between the two lightcurves is therefore defined as $arg[C_j]$ and from this the time delay is simply $arg[C_j]/2\pi\nu_j$. Using the cross spectrum it is also possible to calculate how coherent the emission from the two energy bands is, the coherence function is defined as

$$\gamma^2 = \frac{|\langle C \rangle|^2}{\langle |S_1|^2 \rangle \langle |S_2|^2 \rangle} \tag{5.1}$$

if S_1 and S_2 are the signal from the source above the noise level (Vaughan & Nowak, 1997; Nowak et al., 1999). The coherence was therefore corrected for Poisson noise following the prescription of Vaughan & Nowak (1997), and the time delay was computed in the standard manner (e.g. Nowak et al., 1999; Vaughan et al., 2003b). The cross-spectral estimates were made using time series binned to $\Delta T = 7.34$ s (i.e. 100 pn frame times), averaging over segments of length 3.7 ks (512 data points), and over logarithmic frequency bins. The results are shown in Fig.5.4.

The coherence is consistent with unity, meaning the variations in one band are well correlated with variations in the other band (once corrected for the contribution due to Poisson noise in each band). The delay spectrum is poorly constrained but consistent with a constant phase delay ($\phi \sim 0.3$ rad), or a frequency dependent time delay ($\tau \sim 0.05 f^{-1}$), where the hard band variations precede those in the soft band. A zero time (or phase) delay model is rejected ($p < 0.002$ in a chi-square goodness-of-fit test). The shorter 2008 observation was also analysed in

a similar manner and is consistent with a phase delay of $\phi \sim 0.2$ rad (a zero phase delay model is rejected with $p = 0.043$).

5.5 Discussion

We have shown that the linear rms-flux relation, previously seen in Galactic X-ray binaries and Active Galaxies is also present in the ULX NGC 5408 X-1. This detection is important as it extends the apparent ubiquity of the relation in accreting sources to ULXs. This can be taken as further proof that at least this ULX behaves in a manner similar to other accreting black hole systems. The fact that the rms-flux relation has been observed in the three main types of luminous accreting black hole systems (Galactic Binaries, ULXs and Active Galaxies) suggests that it is either a basic consequence of all luminous accretion onto black holes, or that it only occurs under certain restricted conditions but that these conditions are met for all three types of systems.

The relation is clearly present above 1 keV, but at softer energies the lower variability amplitude means a linear relation can neither be confirmed nor rejected. However, the coherence of the two light curves indicates a common origin for the variability in the two bands, which would suggest that the soft band light curve may contain a linear rms-flux relation with a very low gradient.

We may attempt to explain the observed rms-flux behaviour, in the most basic manner, in terms of two components behaving in different ways. The first component (A) obeys a linear rms-flux relation with zero intercept and a gradient equal to its fractional rms. The second component (B) is variable but its amplitude is constant with flux. This has the effect of adding constant flux and rms, effectively shifting the origin of the observed relation. The fluxes of components A and B are constrained to be non-negative and the average flux and rms of B can

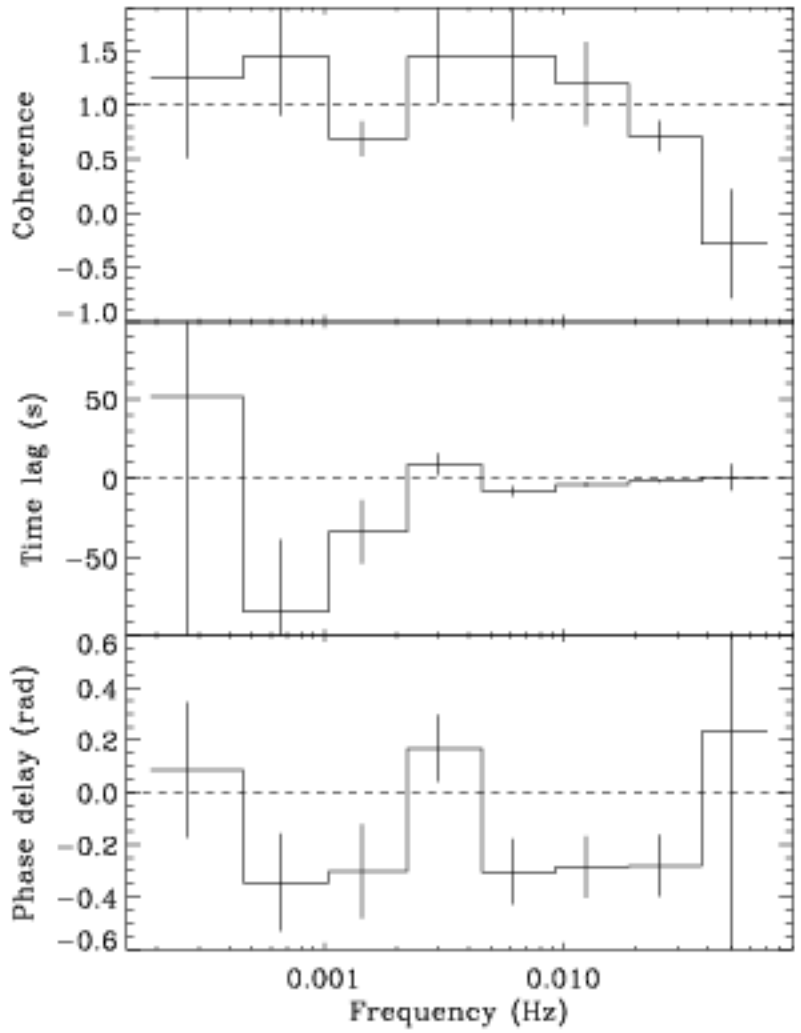

Figure 5.4: Results of cross-spectral analysis between $0.3-1$ keV (soft band) and $1-10$ keV (hard band) light curves from the 2006 observation. The top panels shows the noise-corrected coherence, which is high (~ 1) over the observable range. The lower two panels show different representations of the hard-soft delays. The middle panels shows the time delay $\tau(f)$ and the lowest panel shows the phase delay $\phi(f)$ (which are related by $\tau(f) = \phi(f)/2\pi f$). A negative delay means the hard band leads the soft band. In this case the time delay, or equivalently the phase delay, is inconsistent with zero delay at all frequencies ($p < 0.002$).

be no higher than the minimum observed flux and rms. The fractional rms of component B can be described by the gradient of the line from the origin to this point. The flux intercept of the linear model (C) can be understood in terms of the fractional rms of components A and B; if the fractional rms of B is greater than that of A then the flux intercept will be negative, as observed in the hard-band.

The cross-spectral analysis is also indicative of a time lag which compares favourably to an extrapolation of the lag observed from BHBs to lower frequencies (see e.g. Miyamoto et al., 1988; Cui et al., 1997; Nowak et al., 1999; Pottschmidt et al., 2000; Miyamoto et al., 1993). Although soft lags have been observed less frequently the majority of observations of BHBs do not reach the low energy range analysed here. Miyamoto et al. (1993) have observed soft lags in the very high state of GX 339-4 at low energies (1.2-2.3 keV), which appear similar to those we observe. These results, on both the rms-flux relation and time delays, could be confirmed with long X-ray observations of other bright, variable ULXs. These further observations should help to clarify the explanatory value of our proposed variability components (A and B), and how these and the hard-soft X-ray time lags relate to the different components thought to explain the energy and power spectra of accreting black holes. The present results indicate that such intensive studies of ULX variability, although challenging in terms of the observational demands, hold great promise for constraining the processes driving ULXs behaviour, and the position of ULXs in the scheme of black hole accretion from BHBs to AGN.

Chapter 6

Rms-flux behaviour of a QPO

6.1 Introduction

Although the rms-flux relation in broad-band noise from BHBs appears to ubiquitously follow the rms-flux relation, the behaviour of QPOs appears to be more complicated. The analysis carried out in Chapter 4 identified a number of observations of different sources with QPOs which do not appear to obey a positive linear rms-flux relation. Secular (~ 1 day) variations in the QPO properties (rms and frequency) are known to be correlated with the (energy spectral) evolution of black hole transient outbursts (i.e. changes in the physical state of the system). But this overall evolution of the outburst properties tends to follow distinct patterns, such as the hysteresis curve on the hardness-intensity diagram (HID; see e.g. Belloni et al., 2005; Belloni, 2010a). As previously discussed, the within-observation variations (timescales < 3ks studied here) are variations in an almost stationary process (presumably random fluctuations within the accretion flow), the average properties of which evolve through outburst (see Muñoz-Darias et al., 2010, and Figure 6.1). It is these relatively small and flux-correlated deviations from stationarity, and how they relate to other source properties, that are the subject of this Chapter.

Strong QPO features are required to accurately measure their rms-flux relation above that of the broad-band noise. This work focusses on the type "C" QPOs observed at the beginning of the the 1998 outburst of XTE J1550-564. The long-term properties of this source have been studied extensively by Cui et al. (1999), Wijnands et al. (1999), Homan et al. (2001), Remillard et al. (2002), Sobczak et al. (2000b), Reilly et al. (2001), Chakrabarti et al. (2009), and Rao et al. (2010a). Sobczak et al. (2000b) compared the changes in amplitude and frequency for the QPOs over the course of the outburst to the energy spectral components in both XTE J1550-564 and the 1996-97 outburst of GRO J1655-40. They found that the QPO frequency appears to be linked to both the disc flux and the strength of the power law. They also observe that for the outburst of XTE J1550-564, the amplitude of the QPO is closely linked to the QPO frequency: it rises until around 3 Hz but appears to then fall off above this point. Rao et al. (2010a) split each observation into 128s segments and demonstrated that over time the frequency of the fundamental QPO component can be linked to the disc count rate suggesting that there is some correlation between frequency, flux and QPO amplitude over short timescales. Further examination the short term variations in these parameters for the QPO is presented here, concentrating on the rms-flux relation within each observation and its relation to the peak frequency.

6.2 Observations

The Observations are taken by the PCA detector on *RXTE* from the 1998 outburst of XTE J1550-564 in programs P30188 and P30191, covering the first 46 days of the outburst. The data modes used all had 8 bit wide counters and are not likely to suffer the buffer overflow problems which can distort the rms-flux relation away from a linear relationship (seen in Gleissner et al., 2004, Appendix A). During the first half of the outburst the source reached a very bright intermediate state where the strong ("type C") QPO shows high rms amplitudes,

this means that they are ideal candidates to test the behaviour of the rms-flux relation for QPOs and how this relates to the continuum.

Binned mode data has been used for this analysis. There are a few variations of this data mode used over the outburst, so the energy ranges for some of the observations differ. The ranges have been chosen so that they are as consistent across the sample as possible, although slight variations remain between observations. The energy range chosen was as close to 4-14 keV as possible, and the difference between energy bands is no greater than 0.5 keV.

6.3 Data Analysis

In order to measure the rms-flux relation each continuous light curve is divided into non-overlapping 3 s intervals. Due to the lower frequency limit imposed by this segment size we only use observations from this sample where the primary type C QPO is above 1 Hz. In practice this includes most of the observations where the QPO is detected, only excluding six, leaving 48 observations to be processed. From each 3 s segment the power spectrum was estimated in absolute normalisation using standard techniques, and the background subtracted mean count rate of the interval, corrected to 1 PCU detector, was recorded. The power spectral estimates were then averaged in non-overlapping flux bins, with at least 20 intervals contributing to each bin, to provide well-determined power spectra as a function of flux. These power spectra were then fitted in XSPEC 12 (Arnaud, 1996).

The models discussed in Rao et al. (2010a) have been applied, where multiple Lorentzians are used to describe the fit (see figure 1 of Rao et al., 2010a, and Figure 1.10 of Chapter 1 for representative fitted power spectra). In all observations the model used consisted of four Lorentzians: Two of these were fitted to the broad band noise, they are referred to in Rao et al. (2010a) as L_{ft} and L_{pn} (ft stands for flat topped noise at low frequencies < 1 Hz and pn

for peaked noise, generally seen at frequencies close to, or just above, the QPO harmonic). These two Lorentzians had Q-factors less than 2 ($Q = \nu/\Delta\nu$ where ν is the centroid frequency and $\Delta\nu$ the full width at half maximum). Following Rao et al. (2010a) the primary QPO component is defined as the strongest feature in each observation. Due to the limited frequency range (0.33 - 100 Hz) within the flux-binned power spectra it is rarely possible to resolve the fundamental and both the harmonic and subharmonic simultaneously. For this reason the two further Lorentzians described the primary QPO component and either the harmonic or the subharmonic, depending on which was most visible. These Lorentzians are referred to as L_F and either L_s or L_h. As in Rao et al. (2010a) the Poisson noise component was not removed from the power spectra, but is included as an additional constant in the model. This model provided an adequate fit to all observations within the sample, the reduced χ^2 varied from 0.75 to 1.41, with the worst fit having $\chi^2 = 254.1$ with 179 degrees of freedom. Rao et al. (2010a) indicated the need for a further high frequency broad-band component in some observations within their sample. All of these observations are ones where the QPO is below 1 Hz, therefore this was not necessary for the fitting of any observations used here. For each fit the Lorentzian properties were recorded, namely the total rms (in absolute units, i.e ct/s/PCU), the peak frequency (ν_F) and the width. See Pottschmidt et al. (2003) section 3 for appropriate formulae. The rms value is corrected to represent the power in the QPO over only positive frequencies. This normalisation is thus the integrated power in the QPO (R_F^2) and the measured rms within the component is therefore $\sigma = \sqrt{R_F^2}$.

6.4 Results

Fig. 6.1 shows the dependence of the QPO amplitude (rms) and frequency on flux (count rate) both within and between observations (typically one day apart). Clearly the QPO frequency is varying on short timescales and is well correlated with the flux as mentioned previously

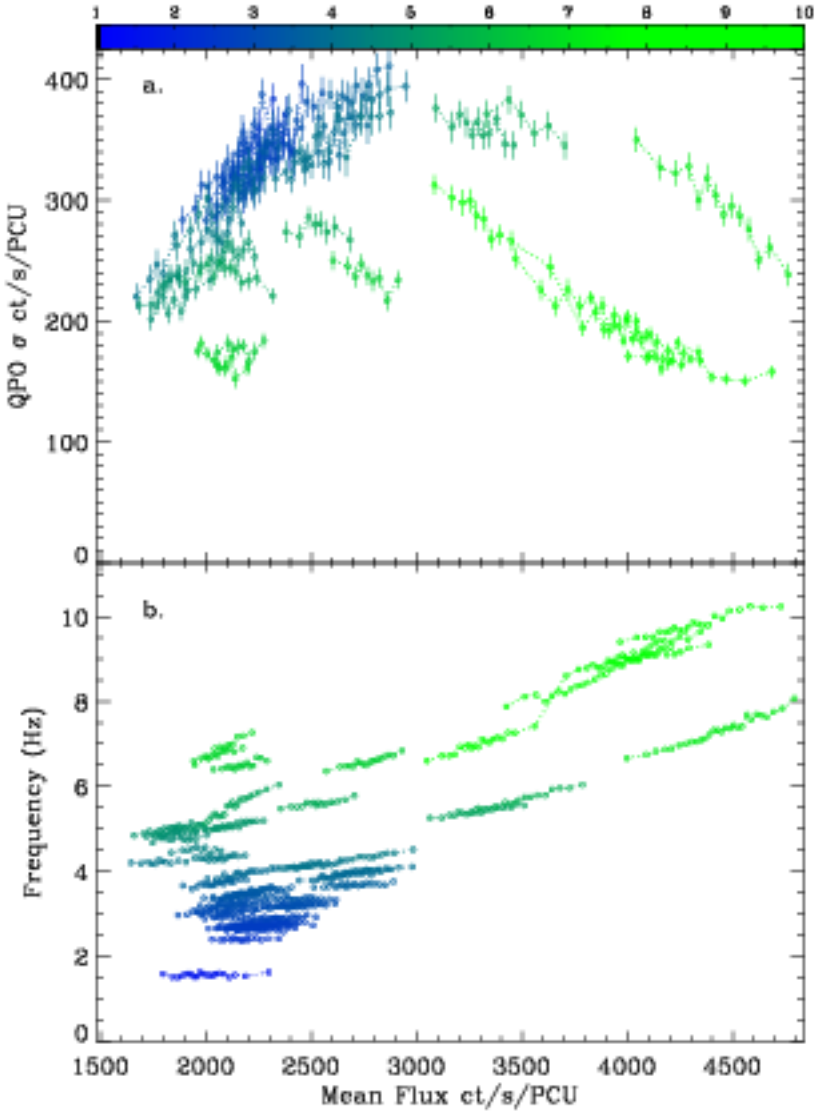

Figure 6.1: *a.* Rms-flux relations for the fundamental QPOs in each observation within the sample. Points within observations are joined by dotted lines. Some observations with rms values close to 350 ct/s/PCU and mean count rates between 2000-2500 ct/s have been removed for clarity. *b.* Measured fundamental QPO frequency for each of the flux bins used for the QPO rms-flux relations. The steeper change in frequency with flux at high frequencies is clearly visible. For both *a.* and *b.* the colour bar describes the average frequency of the fundamental QPO component.

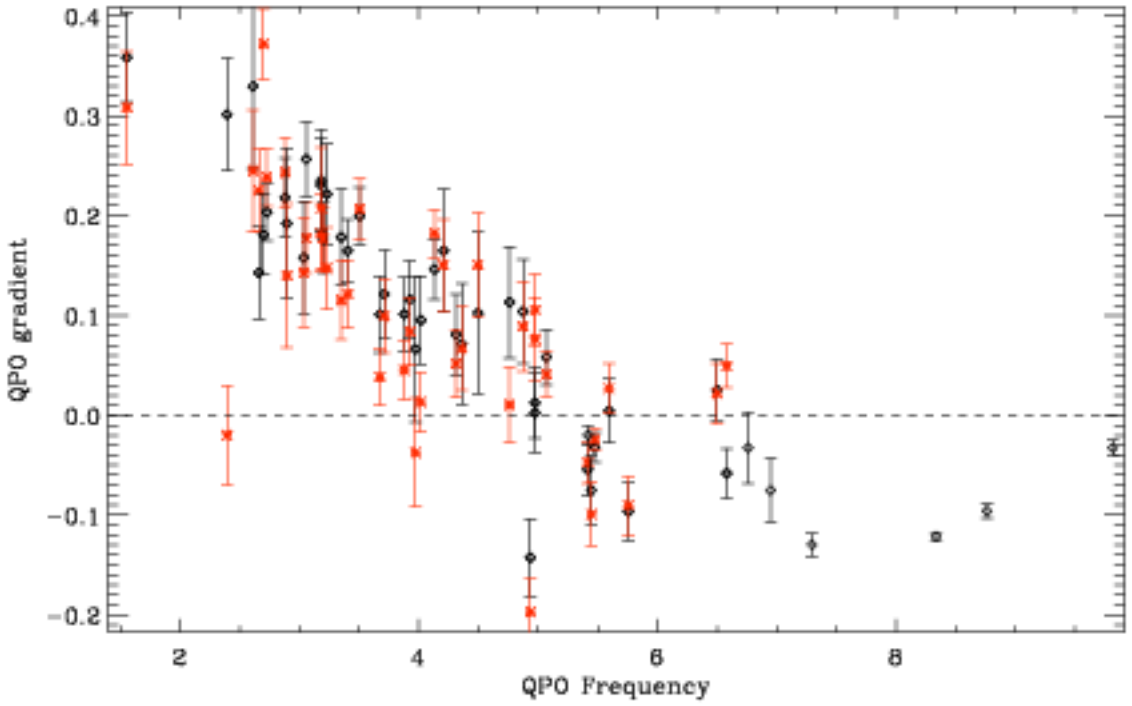

Figure 6.2: Gradient (k) of the rms-flux relation against frequency of the fundamental QPO measured in both the fundamental (*diamonds - black*) and the harmonic (*crosses - red*). Both clearly follow a very similar pattern.

by Rao et al. (2010a), Sobczak et al. (2000b) and Remillard et al. (2002), the gradient of this relation appears to increase with average frequency. The rms shows a more complex relation with the flux: when the QPO is below 4 Hz it follows the positive linear rms-flux relation observed in the broad-band noise, between 4.0-5.5 Hz the rms becomes constant with flux, above 5.5 Hz the rms-flux relation is negative. This is the first time a short-term negative rms-flux relation has been observed. The average QPO frequency for an observation is not monotonically related to either the mean rms or flux over long timescales, even though clear relationships between these variables are found within each observation (see Figure 6.1). This illustrates the different effects of the long term evolution of the system vs. short term random variations in the accretion flow.

Fitting the rms-flux relations for each observation with a linear function gives a reasonable measure of the gradient (k_F) which is clearly anti-correlated with the average QPO frequency (ν_F as seen in Figure 6.2. The point where the gradient reverses from positive to negative occurs around 5.5 Hz. The gradient of the rms-flux relation for the harmonic, k_h, changes simultaneously with that of the fundamental, k_F. Figure 2 shows k_h becomes negative when k_F does, i.e. around $\nu_F > 5.5$ Hz (where $\nu_h > 11$ Hz) (Figure 6.2, red points). The flux dependence of the high frequency power spectral continuum could not be assessed due to uncertainties in subtracting the power of the QPO and harmonics.

The broad-band noise at low frequencies is assumed to be driving the flux variations, thus the rms-flux relation for the QPO will indicate how it is coupled to the noise component. However the strength of the QPO may mean that some power is aliased to lower frequencies, as the lowest frequency observation of the QPO used is close to the Nyquist frequency ($\nu_{NQ} = \delta t/2$) for the 3s averaged flux bins. This may mean that the alterations in the flux are partially the result of the QPO rather than purely the broad-band noise. In order to test this affect the power spectra of the lightcurve binned up to 3s (covering low frequencies) is compared to that averaged from 3s segments using the standard time binning (covering the high frequencies – this is the average of all power spectra used to calculate the rms-flux relation) and one covering the whole range of frequencies (from a lightcurve with standard time binning and large segment sizes). Figure 6.3 shows this comparison, it can quite clearly be seen that there is no extra power at any point between the three power spectra (the gap is caused by frequency binning used to reduce errors). This suggests that the flux changes are caused by the broad-band noise at low frequencies, rather than the QPO.

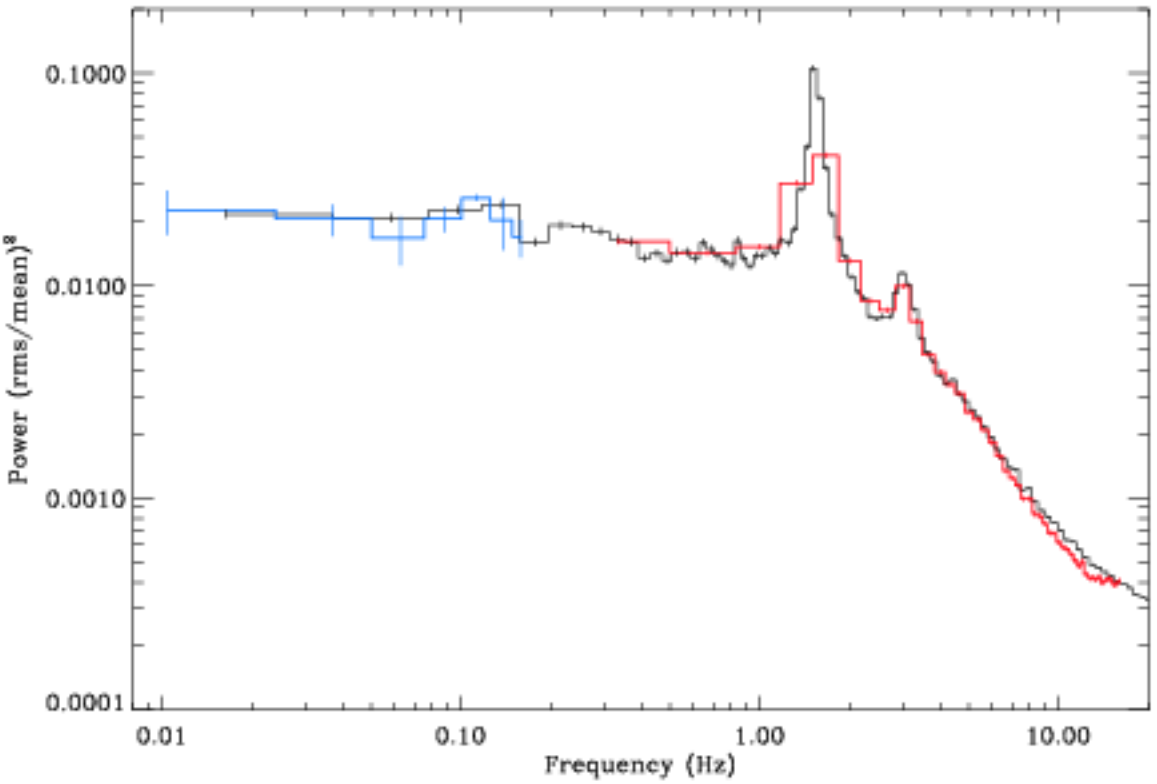

Figure 6.3: Testing for the affects of aliased power from the QPO on the low frequency power spectra. *Black* Power spectra from lightcurve with the standard time binning composed from long segments; *Blue* PSD from lightcurve binned up to 3s; *Red* PSD averaged from 3s segments of lightcurve.

6.5 Discussion

6.5.1 Summary

These results show that the rms amplitude (σ_F) and peak frequency (ν_F) of the "type C" QPO of the microquasar XTE J1550-564 (observed during the 1998 outburst) both vary strongly on short timescales ($3 - 3000$ s) and are correlated with the source flux. The rms-flux relation for the QPO depends on the peak frequency of the QPO: when $\nu_F \sim 1 - 5$ Hz there is a positive, linear correlation between the QPO rms and flux, at around $\nu_F \sim 5$ Hz the rms-flux relation becomes flat (rms independent of flux), and at higher frequencies the rms and flux becomes

negatively correlated. For all values of ν_F examined ($\sim 1.5 - 10$ Hz) the rms-flux relation is approximately linear, and the gradient itself appears to be monotonically related to the QPO peak frequency. Above ~ 3 Hz ν_F also increases with flux in an approximately linear manner, below this point it remains constant. The correlations between the flux and the QPO rms and peak frequency on these short timescales are distinct from the long term evolution of the QPO during the outburst that is apparent between observations separated typically by ~ 1 day.

Within the framework of the "propagating fluctuation" model discussed in the Introduction, it is reasonable to imagine the QPOs as an enhancement in the variability amplitude at certain frequencies (radii) but still coupled to the broad-band spectrum of variations. This would naturally lead to a linear, positive correlation between long term flux (driven by variations at frequencies lower than the QPO) and QPO rms amplitude. It is less obvious what causes the frequency-dependent changes in the rms-flux behaviour of the QPO. Some possibilities and implications are explored below.

6.5.2 The effect of a Frequency Dependent Filter

Using these observations Sobczak et al. (2000b) showed that on long timescales the fractional rms of the QPO rises with frequency until around 3 Hz, above this it falls off steeply (see their figure 6). Pottschmidt et al. (2003) and Axelsson et al. (2005) showed that the broad Lorentzian components of the power spectrum of Cygnus X-1 also show a sharp drop in amplitude above 3-5 Hz (see figure 6 of Pottschmidt et al., 2003). Similar correlations between QPO amplitude and frequency have been observed in the BHBs H1743-322, GRO J1650-500, XTE J1655-40 and GRS 1915+105 (McClintock et al., 2009; Kalemci et al., 2006, 2003; Debnath et al., 2009; Muno et al., 1999).

One explanation for the attenuation of these components as they move to higher frequencies is in terms of a low pass filter acting to suppress variability above $\sim$ *few* Hz (Done et al., 2007;

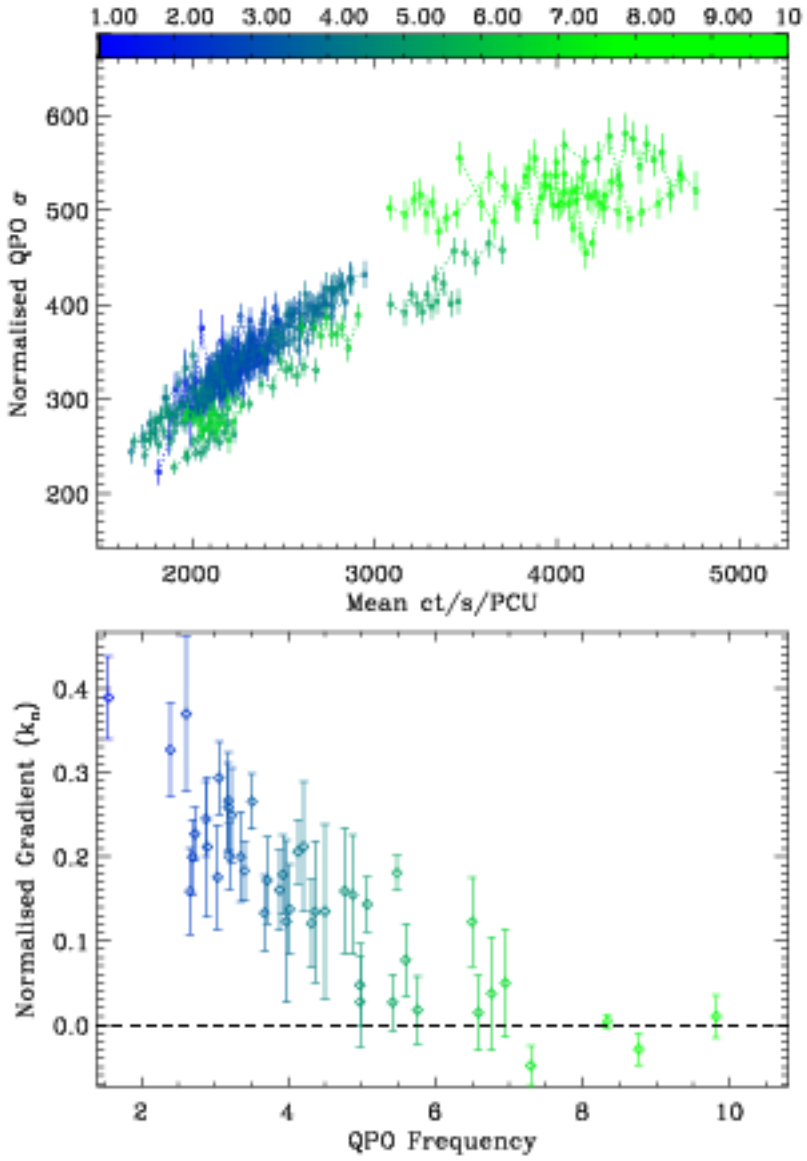

Figure 6.4: *a)* Rms-flux relations for the QPO following the removal of a filter reducing the amplitude of the QPO with increasing frequency. *b)* Gradients found from fitting the above rms-flux relation with a linear function. Frequency dependence of the rms-flux relation is still visible, but the gradients no longer become negative.

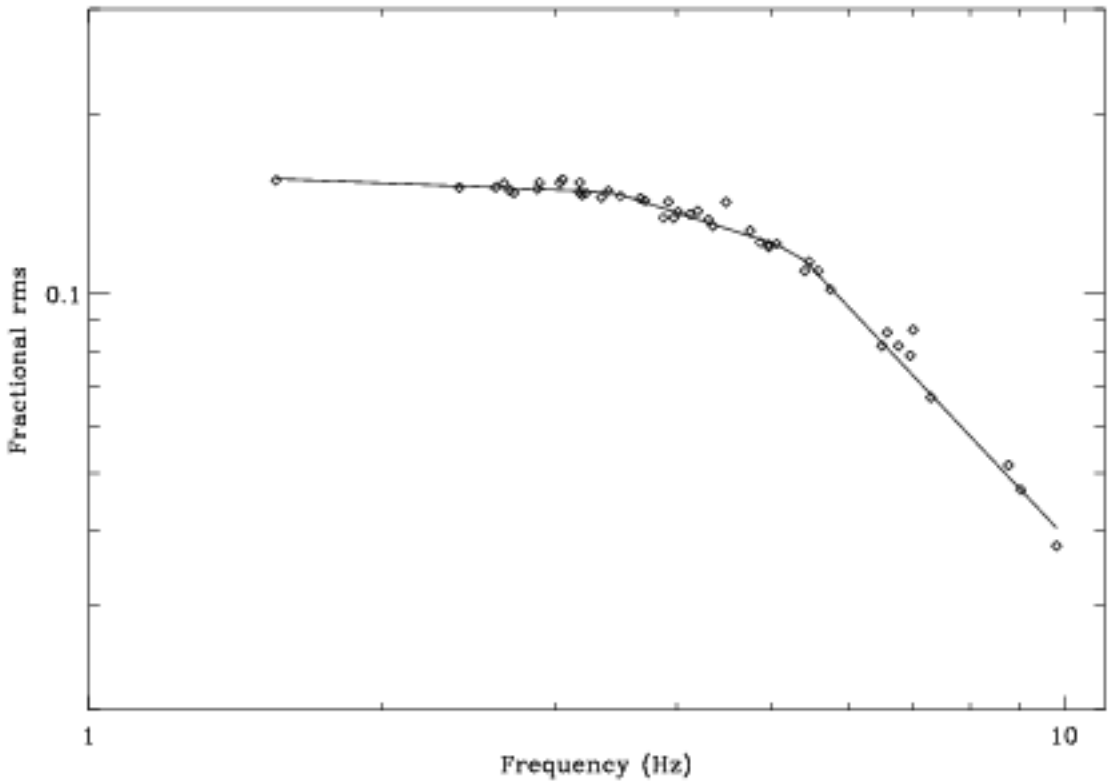

Figure 6.5: The estimated shape of the frequency dependent filter from fitting the mean fractional rms and frequency of each QPO

Gierliński et al., 2008). Proposed physical mechanisms for the suppression of fast variations include the damping of accretion rate perturbations faster than the viscous timescale in the inner disc (Psaltis & Norman, 2000; Done et al., 2007) and scattering of emitted X-rays by an optically thick outflow created at high luminosity Titarchuk et al. (2007). Such a filter would affect the observed rms-flux behaviour for QPOs that move in frequency above $\sim 3-5$ Hz. Is the change in k_F simply the result of a QPO frequency that increases with flux on short timescales, combined with the rms being more strongly suppressed (by the action of the filter) at higher frequencies and thus fluxes? In order to investigate this possibility we modelled the decay of the QPO (fractional) rms with frequency in terms of a doubly broken power law, and use this to "recover" the unfiltered QPO rms.

A doubly broken power law over 1.5-10 Hz, with indices of α = -0.1, -0.5 and -1.7 and break-

ing at 3.4 Hz and 5.1 Hz respectively 6.5, can be used to describe the trend in the long term rms-frequency behaviour of the QPO. Note that this is likely an over-estimate of the effect of a filter, since it predicts filtering of the power spectrum by a power law with with index −3.4 above 5 Hz; the observed power spectrum is usually flatter. Assuming this function describes the filter it is possible to "correct" each data point in Figure 6.1 for the rms-reducing effect of the frequency-dependent filter.

The rms-flux relations using the "filter-corrected" amplitudes are shown in Figure 6.4. There are two significant differences between this and the raw data shown in Figure 6.1a: at higher frequencies the rms-flux gradient tends to zero above ∼ 5 Hz, rather than becoming negative, and the short timescale rms-flux data (within each observation) now follow a similar curve to the longer timescale (between observation) changes in rms and flux. Significantly for the present discussion, the rms-flux relation still shows a monotonic dependence of gradient on the QPO frequency. A flattening to zero gradient might indicate a ceiling on the QPO strength (in absolute units) which effectively prevents the rms increasing past ∼ 600 ct s^{-1} when $\nu_F > 5$ Hz.

6.5.3 Physical implications of QPO behaviour

Although a complete physical picture for the origin of QPOs is still lacking (see e.g. van der Klis, 2006), recently proposed ideas include Lense-Thirring precession of an extended, hot flow (see e.g. Ingram et al., 2009) and a magnetohydrodynamic dynamo cycle (O'Neill et al., 2010). However, it is not clear what, if any, predictions such models make for the rms-flux relation of the QPO. One would hope that as these and similar models are developed and explored they will yield specific predictions about the coupling of QPO amplitude and the lower frequency noise variations that can then be compared against the observed behaviour.

This work has shown that there is a clear change in the flux-dependence of the QPO that is

itself linked to the QPO frequency, and that peak frequencies of $\nu_F \approx 5-6$ Hz appear to stand out as marking where the rms-flux gradient becomes zero. (This seems quite robust to the possible effects of a frequency-dependent filter.) This frequency range is already noteworthy as the location of the type B QPOs in this outburst and others. Given this coincidence it seems reasonable to speculate that 5-6 Hz may represent a relatively stable characteristic frequency of the system (in contrast to the variable peak frequency of type C QPOs). Replication of these results for other sources and outbursts is necessary to establish whether a fixed characteristic frequency can be identified in this way.

The 1999 outburst of XTE J1859+226 shows similar behaviour to that of XTE J1550-564 remaining in a hard intermediate state at the peak of the outburst for an extended period. The rms-flux relation of the QPO has been measured for 12 of these observations. Although the QPO is not as strong as those observed from XTE J1550-564 and thus the behaviour cannot be as well constrained Figure 6.6 suggests that there is still a significant alteration in the gradient of the rms-flux relation for these type 'C' QPOs. At low frequencies (3 Hz) the gradient is constrained to positive values whereas above ~ 5 Hz the gradient is either very low or negative. Therefore it is possible that the frequency dependent behaviour of the rms-flux relation in this QPO is very similar to that observed in XTE J1550-564, and that a change from positive to flat rms-flux behaviour may even occur at a similar point. There is very little observed frequency shift with flux in these observations so it was not necessary to attempt removal of a frequency-dependent filter.

The fact that the 5-6 Hz range appears to also be significant for the QPO behaviour in XTE J1859+226 as well as XTE J1550-564 fuels speculation that this relates to a stable timescale for the variabilty at which the behaviour alters. If the QPO does relate to the outer radius of a hot, optically thin inner flow, as suggested by models of the type C QPO (see e.g. Ingram et al., 2009), then this changing radius may reach a point beyond which the amplitude of the QPO can no longer grow. This may occur if timescale of the oscillations forming the QPO are close

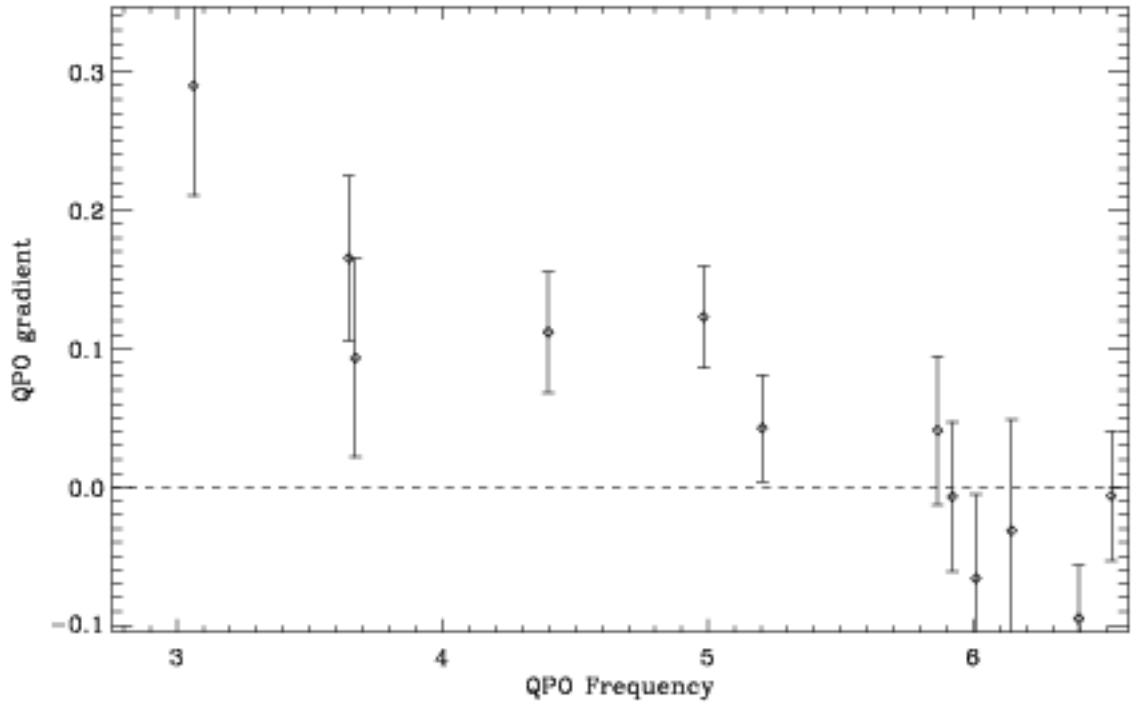

Figure 6.6: The gradient of the rms-flux relation for type C QPOs from the 1999 outburst of XTE J1859+226 plotted according to its peak frequency. Similar behaviour to that observed from XTE J1550-564 may be present.

to the viscous timescale within the disc. Explorations into the correlation of flux-dependent alterations in the energy spectra over short timescales with those of the QPO, could reveal what region of the disc contributes to the changes observed.

This suggests that similar behaviour may be observable in other sources, although stronger QPO features and higher count rates are needed before this can be confirmed.

6.5.4 Correlations with the energy spectra

It is well known that the properties of the type C QPOs in BHB outbursts (notably ν_F) are strongly correlated with the various energy spectral parameters over long timescales, i.e. be-

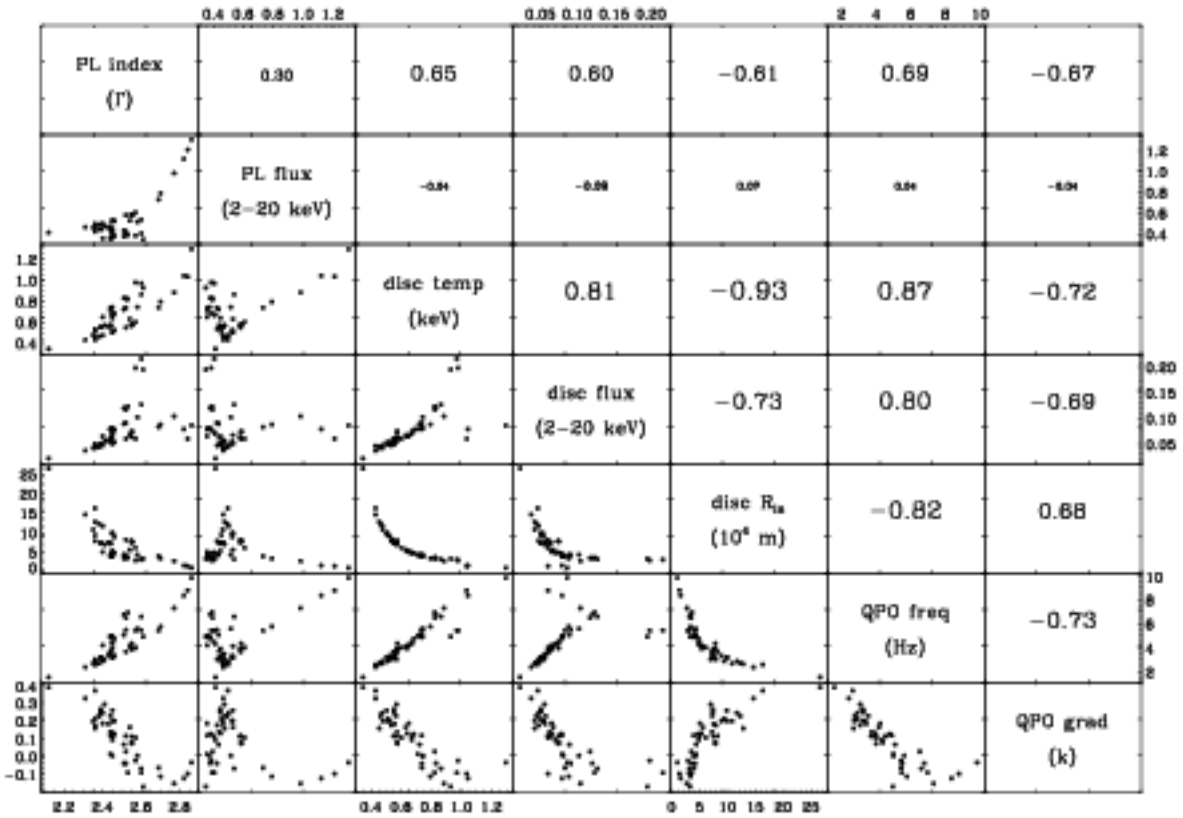

Figure 6.7: Comparison of the QPO parameters (frequency and rms-flux gradient) with the energy spectral parameters from Sobczak et al. (2000a), similar results are seen using the parameters from Dunn et al. (2010) using different energy spectral models. Upper right corner shows Kendall's correlation coefficient for each parameter.

tween observations (see e.g. Sobczak et al., 2000b; Remillard et al., 2002; Rao et al., 2010a, for discussion of the 1998 outburst of XTE J1550-564). Using the spectral parameters obtained by both Sobczak et al. (2000a) and Dunn et al. (2010) we find strong correlations between the energy spectrum (e.g. power law index, disc flux, etc.) and the gradient k_F of the rms-flux relation for the QPO, as would be expected given that all these variables are strongly correlated with ν_F. Figure 6.7 shows these comparisons for the fits made by Sobczak et al. (2000a).

Dunn et al. (2010) noted that this outburst of XTE J1550-564 is unusual in that it reaches a particularly high intermediate state, at the peak of the outburst they find that the luminosity is close to L_{Edd}. It is during these high flux observations, where the QPO reaches its highest

frequency, that the loss in positive correlation between rms and flux is most clearly seen. Further investigations into the effect of high luminosities, and their associated states, on the short-timescale behaviour of low frequency QPOs in other outbursts and sources would be necessary to fully understand any link.

Chapter 7

Conclusions and Future Work

7.1 Summary

Studies of X-ray variability from accreting black holes probe the conditions close to the event horizon. In this region the behaviour of the matter is expected to be the same for objects on all mass scales, similar observational signals should therefore be found in the emission from all sources. In this thesis I present work which tests for the existence of these similarities in a class of poorly understood objects, and attempts to establish the ubiquity of another possible signal of accretion.

Chapter 3 presented a systematic survey of the short term variability properties in 19 observations of 16 ULXs taken with *XMM-Newton* using their power spectra. Significant short term variability was detected in 8 observations (6 sources), the remaining observations displayed power spectra which were consistent with the Poisson noise level. For these observations upper limits were found on the amount of short term variability which could be masked by the noise level. These upper limits were compared to the levels of variability seen from BHBs in various non-thermally dominated states. Four observations out of the 11 non-detections, have

upper limits on levels of variability below those observed in BHBs. Simulations of lightcurves with power spectral shapes modelled on those observed from galactic BHBs in various states confirmed that similar levels of variability should still be visible even at these low count rates. This indicates that short-term variability is suppressed at the time of observation in these sources. Suggested causes for this suppression include large scale optically thick outflows destroying correlated variability from the source, or variability concentrated over much shorter timescales than those studied here, similar to the χ states of GRS 1915+105.

In Chapter 4 archival observations for 9 BHBs taken with *RXTE* were tested for a positive rms-flux relation. This revealed that it appears to be ubiquitous in the broad-band noise for all long, bright observations with sufficient variability to measure the rms. I show comparisons between both the hardness and fractional rms-intensity diagrams which identify the source states of various observations. The RID reveals different behaviour to that of the HID, particularly when the source rises or returns to the hard state, conversely there is also behaviour visible in the HID which cannot be seen in the RID. These plots may be used in conjunction to evaluate the state of an observation without individually checking both the power spectra or the energy spectra. Comparing the properties of the rms-flux relations (gradient and intercept from the fits to a linear function) to these plots reveals the intercepts to be state dependent, becoming strongly positive as the source moves into the hard intermediate state. This strong offset on the flux axis can be reproduced by simulating lightcurves with PSD shapes modelled on those found in real observations, suggesting that the x-intercepts are not always due to additional components in the lightcurve but may be a result of the multiplicative effect on the variations over different timescales.

In Chapters 5 and 6 the presence of a positive, linear rms-flux correlation was found in the light curve from a ULX (NGC 5408 X-1) and in some observations of the type C QPO from the 1998 outburst of XTE J1550-564. In the former case this suggests both that the accretion processes producing the variability in this ULX are similar to those in other accreting compact

objects. In the latter case this work revealed that the rms-flux relation is dependent on the frequency of the QPO, becoming constant or even negative once the QPO moves above ~ 5 Hz. This could indicate an upper limit on the levels of flux or variability allowed by the source. A possible lag (soft lagging hard emission) is also identified from the ULX.

7.2 Future work

A whole range of new questions are raised from this work – Does the amount of variability seen from ULXs change over time? How ubiquitous is the rms-flux relation for other compact objects i.e Neutron stars? Why do QPOs appear to behave differently to the surrounding broad-band noise and how may this behaviour be interpreted?

Further long observations of bright ULXs are necessary to build up a full picture of their behaviour. Monitoring is currently being carried out by *Swift* which has suggested that the energy spectra remains surprisingly stationary over long periods of time (~ 1 yr) and whilst there are large changes in the flux (Grisé et al., 2010). Equally the two observations of NGC 5408 X-1 taken two years apart show a shift in the frequency of the QPO, but little alteration in the state of the power spectra, behaviour not typically observed in BHBs which display rapid changes in both the energy and timing domains over the course of an outburst. Testing further observations of other ULXs for the rms-flux relation could reveal further similarities or differences between these sources, BHBs and AGN. M82 X-1 has been quite frequently monitored by *RXTE* over a period of 6 years Strohmayer & Mushotzky (2003) have observed the QPO in the power spectra within some of these observations. Rms-hardness diagrams plotted using this data set may reveal behaviour similar to that observed in outbursts of LMXBs, or alternatively suggest a different evolutionary path for this object.

One direct extension to the work described Chapter 4 would involve fitting the individual

power spectra. Not only would this allow for simulations of the rms-flux relation to be performed for all observations, predicting the expected intercepts for each, but if the upper and lower quartiles of the flux binned power spectra were also fitted exactly how fixed in shape the PSD remains with increasing flux could be tested. Further extensions include testing the energy dependence of the relation, although this is most likely to be related to the amount of fractional rms in the power spectra in different energy bands (see results in Gleissner et al., 2004; Gierliński & Zdziarski, 2005).

Although the rms-flux relation has been observed in a neutron star it has only been identified in very few cases both of the same source (SAX J1808.4-3658 – Uttley & McHardy, 2001; Uttley, 2004). X-ray variability in neutron stars is known to be similar to that of BHBs so we may expect the positive rms-flux correlation to be equally ubiquitously observed. These objects evolve much faster than LMXBs so identifying sections of lightcurve with a fixed power spectral shape is more complex. Extending our knowledge of the rms-flux relation to a wide range of states in NS would further establish it as an essential property of the variability in accreting compact objects. Similarly attempts could be made to observe this relation in a cataclysmic variable, another accreting compact object which should also show a positive linear correlation if the relation is ubiquitous.

Further studies of QPOs are also necessary to explain their divergence from a positive correlation, further observations of behaviour in other BHBs would be useful, but is dependent on consistent observations taken when an object is in the HIMS. Alternatively, observations of GRS 1915+105, a BHB which displays highly complex atypical patterns of short term variability could be used to explore QPO behaviours. Finally if the rms-flux relation is as consistently observed in NS as it is in BHBs, the rms-flux relation of low or high frequency QPOs in these objects could also be explored. Further exploration into how these features couple to the underlying broad-band noise using higher order Fourier constructs such as the bicoherence could also reveal much useful information. This quantity tests how strongly the

phases are coupled for different Fourier frequencies, simulations suggest that it can reveal complex behaviour when sharp features are present and that this function could display different patterns depending on the formation mechanism of the QPO (Maccarone & Schnittman, 2005).

This thesis provides a snapshot into the amount of information which can be gleaned from studying the properties of short term variability in accreting compact objects. In the future new instruments and missions in a wide range of wavelengths, from the optical to the X-ray, will allow for wider monitoring and understanding of these objects. There is also still a wealth of data in the archives of current X-ray telescopes, nearly 15 years of data in the case of *RXTE*, and new analysis techniques are still waiting to be applied to it. We are still only beginning to understand the full implications of what short term variability can teach us about these exotic objects.

BIBLIOGRAPHY

Arévalo P., McHardy I. M., Summons D. P., 2008, *MNRAS*, 388, 211

Arnaud K. A., 1996, in Astronomical Society of the Pacific Conference Series, Vol. 101, Astronomical Data Analysis Software and Systems V, G. H. Jacoby & J. Barnes, ed., pp. 17–+

Axelsson M., Borgonovo L., Larsson S., 2005, *A&A*, 438, 999

Balbus S. A., Hawley J. F., 1991, *ApJ*, 376, 214

Barnard R., Trudolyubov S., Kolb U. C., Haswell C. A., Osborne J. P., Priedhorsky W. C., 2007, *A&A*, 469, 875

Belloni T., 2004, Nuclear Physics B Proceedings Supplements, 132, 337

Belloni T., Hasinger G., 1990, *A&A*, 227, L33

Belloni T., Homan J., Casella P., van der Klis M., Nespoli E., Lewin W. H. G., Miller J. M., Méndez M., 2005, *A&A*, 440, 207

Belloni T., Klein-Wolt M., Méndez M., van der Klis M., van Paradijs J., 2000, *A&A*, 355, 271

Belloni T., Psaltis D., van der Klis M., 2002, *ApJ*, 572, 392

Belloni T. M., 2010a, ArXiv e-prints

—, 2010b, in Lecture Notes in Physics, Berlin Springer Verlag, Vol. 794, Lecture Notes in Physics, Berlin Springer Verlag, T. Belloni, ed., pp. 53–+

Bolton C. T., 1972, Nat., 240, 124

Bowyer S., Byram E. T., Chubb T. A., Friedman H., 1965, Science, 147, 394

Bradt H. V., Swank J. H., Rothschild R. E., 1990, Advances in Space Research, 10, 297

Brocksopp C., Fender R. P., McCollough M., Pooley G. G., Rupen M. P., Hjellming R. M., de la Force C. J., Spencer R. E., Muxlow T. W. B., Garrington S. T., Trushkin S., 2002, *MNRAS*, 331, 765

Brown G. E., Lee C., Wijers R. A. M. J., Bethe H. A., 2000, Phys. Rep., 333, 471

Caballero-García M. D., Fabian A. C., 2010, *MNRAS*, 402, 2559

Calvelo D. E., Fender R. P., Russell D. M., Gallo E., Corbel S., Tzioumis A. K., Bell M. E., Lewis F., Maccarone T. J., 2010, *MNRAS*, 1361

Casella P., Ponti G., Patruno A., Belloni T., Miniutti G., Zampieri L., 2008, *MNRAS*, 666

Chakrabarti S. K., Dutta B. G., Pal P. S., 2009, *MNRAS*, 394, 1463

Churazov E., Gilfanov M., Revnivtsev M., 2001, *MNRAS*, 321, 759

Colbert E. J. M., Mushotzky R. F., 1999, *ApJ*, 519, 89

Colbert E. J. M., Petre R., Schlegel E. M., Ryder S. D., 1995, *ApJ*, 446, 177

Colbert E. J. M., Ptak A. F., 2002, ApJS, 143, 25

Corbel S., Fender R. P., Tzioumis A. K., Tomsick J. A., Orosz J. A., Miller J. M., Wijnands R., Kaaret P., 2002, Science, 298, 196

Corbel S., Tomsick J. A., Kaaret P., 2006, *ApJ*, 636, 971

Cropper M., Soria R., Mushotzky R. F., Wu K., Markwardt C. B., Pakull M., 2004, *MNRAS*, 349, 39

Cui W., Zhang S. N., Chen W., Morgan E. H., 1999, *ApJL*, 512, L43

Cui W., Zhang S. N., Focke W., Swank J. H., 1997, *ApJ*, 484, 383

Debnath D., Chakrabarti S. K., Nandi A., Mandal S., 2009, ArXiv e-prints

den Herder J. W., Brinkman A. C., Kahn S. M., Branduardi-Raymont G., Thomsen K., Aarts H., Audard M., Bixler J. V., den Boggende A. J., Cottam J., Decker T., Dubbeldam L., Erd C., Goulooze H., Güdel M., Guttridge P., Hailey C. J., Janabi K. A., Kaastra J. S., de Korte P. A. J., van Leeuwen B. J., Mauche C., McCalden A. J., Mewe R., Naber A., Paerels F. B., Peterson J. R., Rasmussen A. P., Rees K., Sakelliou I., Sako M., Spodek J., Stern M., Tamura T., Tandy J., de Vries C. P., Welch S., Zehnder A., 2001, *A&A*, 365, L7

Dewangan G. C., Griffiths R. E., Rao A. R., 2006a, *ApJL*, 641, L125

Dewangan G. C., Miyaji T., Griffiths R. E., Lehmann I., 2004, *ApJL*, 608, L57

Dewangan G. C., Titarchuk L., Griffiths R. E., 2006b, *ApJL*, 637, L21

—, 2006c, *ApJL*, 637, L21

Dhawan V., Mirabel I. F., Rodríguez L. F., 2000, *ApJ*, 543, 373

Doi K., 1978, Nat., 275, 197

Done C., 2010, ArXiv e-prints

Done C., Diaz Trigo M., 2010, *MNRAS*, 407, 2287

Done C., Gierliński M., 2005, *MNRAS*, 364, 208

Done C., Gierliński M., Kubota A., 2007, A&A Rev., 15, 1

Done C., Kubota A., 2006, *MNRAS*, 371, 1216

Dunn R. J. H., Fender R. P., Körding E. G., Belloni T., Cabanac C., 2010, *MNRAS*, 403, 61

Elvis M., Page C. G., Pounds K. A., Ricketts M. J., Turner M. J. L., 1975, Nat., 257, 656

Fabbiano G., 1989, Ann. Rev. A&A, 27, 87

—, 1995, in X-ray Binaries, W. H. G. Lewin, J. van Paradijs, & E. P. J. van den Heuvel, ed., pp. 390–418

—, 2006, Advances in Space Research, 38, 2937

Fabbiano G., Zezas A., Murray S. S., 2001, *ApJ*, 554, 1035

Fender R. P., Homan J., Belloni T. M., 2009, *MNRAS*, 396, 1370

Fender R. P., Kuulkers E., 2001, *MNRAS*, 324, 923

Feng H., Kaaret P., 2005, *ApJ*, 633, 1052

—, 2007, *ApJ*, 668, 941

—, 2009, *ApJ*, 696, 1712

Feng H., Rao F., Kaaret P., 2010, *ApJL*, 710, L137

Frank J., King A., Raine D. J., 2002, Accretion Power in Astrophysics: Third Edition, Frank, J., King, A., & Raine, D. J., ed.

Gallo E., 2010, in Lecture Notes in Physics, Berlin Springer Verlag, Vol. 794, Lecture Notes in Physics, Berlin Springer Verlag, T. Belloni, ed., pp. 85–+

Gallo E., Fender R. P., Miller-Jones J. C. A., Merloni A., Jonker P. G., Heinz S., Maccarone T. J., van der Klis M., 2006, *MNRAS*, 370, 1351

Gandhi P., 2009, *ApJL*, 697, L167

Gaskell C. M., 2004, *ApJL*, 612, L21

Giebels B., Degrange B., 2009, *A&A*, 503, 797

Gierliński M., Middleton M., Ward M., Done C., 2008, Nat., 455, 369

Gierliński M., Zdziarski A. A., 2005, *MNRAS*, 363, 1349

Gilfanov M., 2010, in Lecture Notes in Physics, Berlin Springer Verlag, Vol. 794, Lecture Notes in Physics, Berlin Springer Verlag, T. Belloni, ed., pp. 17–+

Gladstone J. C., Roberts T. P., Done C., 2009, *MNRAS*, 397, 1836

Gleissner T., Wilms J., Pottschmidt K., Uttley P., Nowak M. A., Staubert R., 2004, *A&A*, 414, 1091

Goad M. R., Roberts T. P., Reeves J. N., Uttley P., 2006, *MNRAS*, 365, 191

Greiner J., Cuby J. G., McCaughrean M. J., 2001, Nature, 414, 522

Grimm H., Gilfanov M., Sunyaev R., 2003, *MNRAS*, 339, 793

Grisé F., Kaaret P., Feng H., Kajava J. J. E., Farrell S. A., 2010, *ApJL*, 724, L148

Guainazzi M., Matt G., Brandt W. N., Antonelli L. A., Barr P., Bassani L., 2000, *A&A*, 356, 463

Hiemstra B., Méndez M., Done C., Díaz Trigo M., Altamirano D., Casella P., 2010, *MNRAS*, 1748

Hiemstra B., Soleri P., Méndez M., Belloni T., Mostafa R., Wijnands R., 2009, *MNRAS*, 394, 2080

Homan J., Wijnands R., van der Klis M., Belloni T., van Paradijs J., Klein-Wolt M., Fender R., Méndez M., 2001, ApJS, 132, 377

Hui Y., Krolik J. H., 2008, *ApJ*, 679, 1405

Humphrey P. J., Fabbiano G., Elvis M., Church M. J., Balucinska-Church M., 2003, VizieR Online Data Catalog, 734, 40134

Ingram A., Done C., Fragile P. C., 2009, *MNRAS*, 397, L101

Irwin J. A., Bregman J. N., Athey A. E., 2004, *ApJL*, 601, L143

Jahoda K., Markwardt C. B., Radeva Y., Rots A. H., Stark M. J., Swank J. H., Strohmayer T. E., Zhang W., 2006, ApJS, 163, 401

Jansen F., Lumb D., Altieri B., Clavel J., Ehle M., Erd C., Gabriel C., Guainazzi M., Gondoin P., Much R., Munoz R., Santos M., Schartel N., Texier D., Vacanti G., 2001, *A&A*, 365, L1

Kaaret P., Corbel S., Prestwich A. H., Zezas A., 2003, Science, 299, 365

Kaaret P., Feng H., 2007, *ApJ*, 669, 106

—, 2009, *ApJ*, 702, 1679

Kaaret P., Simet M. G., Lang C. C., 2006, *ApJ*, 646, 174

Kalemci E., Tomsick J. A., Rothschild R. E., Pottschmidt K., Corbel S., Kaaret P., 2006, *ApJ*, 639, 340

Kalemci E., Tomsick J. A., Rothschild R. E., Pottschmidt K., Corbel S., Wijnands R., Miller J. M., Kaaret P., 2003, *ApJ*, 586, 419

King A. R., Pringle J. E., West R. G., Livio M., 2004, *MNRAS*, 348, 111

Klein-Wolt M., van der Klis M., 2008, *ApJ*, 675, 1407

Kong A. K. H., McClintock J. E., Garcia M. R., Murray S. S., Barret D., 2002, *ApJ*, 570, 277

Körding E. G., Migliari S., Fender R., Belloni T., Knigge C., McHardy I., 2007, *MNRAS*, 380, 301

Leahy D. A., Darbro W., Elsner R. F., Weisskopf M. C., Kahn S., Sutherland P. G., Grindlay J. E., 1983, *ApJ*, 266, 160

Lehto H. J., 1989, PhD thesis, UNIVERSITY OF VIRGINIA.

Liu J., Bregman J. N., 2005a, ApJS, 157, 59

Liu J.-F., Bregman J. N., 2005b, ApJS, 157, 59

Liu Q. Z., Mirabel I. F., 2005, *A&A*, 429, 1125

Lyubarskii Y. E., 1997, *MNRAS*, 292, 679

Maccarone T. J., Schnittman J. D., 2005, *MNRAS*, 357, 12

Mapelli M., Colpi M., Zampieri L., 2009, *MNRAS*, 395, L71

Mapelli M., Ripamonti E., Zampieri L., Colpi M., Bressan A., 2010, *MNRAS*, 408, 234

Markowitz A., Edelson R., Vaughan S., Uttley P., George I. M., Griffiths R. E., Kaspi S., Lawrence A., McHardy I., Nandra K., Pounds K., Reeves J., Schurch N., Warwick R., 2003, *ApJ*, 593, 96

Mason K. O., Breeveld A., Much R., Carter M., Cordova F. A., Cropper M. S., Fordham J., Huckle H., Ho C., Kawakami H., Kennea J., Kennedy T., Mittaz J., Pandel D., Priedhorsky W. C., Sasseen T., Shirey R., Smith P., Vreux J., 2001, *A&A*, 365, L36

Matsumoto H., Tsuru T. G., Koyama K., Awaki H., Canizares C. R., Kawai N., Matsushita S., Kawabe R., 2001, *ApJL*, 547, L25

McClintock J. E., Remillard R. A., 2006a, Black hole binaries, Compact stellar X-ray sources, pp. 157–213

—, 2006b, Black hole binaries, Compact stellar X-ray sources, pp. 157–213

McClintock J. E., Remillard R. A., Rupen M. P., Torres M. A. P., Steeghs D., Levine A. M., Orosz J. A., 2009, *ApJ*, 698, 1398

McHardy I. M., Koerding E., Knigge C., Uttley P., Fender R. P., 2006, Nat., 444, 730

Middleton M. J., Roberts T. P., Done C., Jackson F. E., 2010, *MNRAS*, 1688

Miller J. M., Fabbiano G., Miller M. C., Fabian A. C., 2003, *ApJL*, 585, L37

Miller J. M., Fabian A. C., Miller M. C., 2004, *ApJL*, 614, L117

Mineo S., Gilfanov M., Sunyaev R., 2010, ArXiv e-prints

Miyamoto S., Iga S., Kitamoto S., Kamado Y., 1993, *ApJL*, 403, L39

Miyamoto S., Kimura K., Kitamoto S., Dotani T., Ebisawa K., 1991, *ApJ*, 383, 784

Miyamoto S., Kitamoto S., 1989, Nat., 342, 773

Miyamoto S., Kitamoto S., Mitsuda K., Dotani T., 1988, Nat., 336, 450

Muñoz-Darias T., Motta S., Belloni T. M., 2010, *MNRAS*, 1553

Mucciarelli P., Casella P., Belloni T., Zampieri L., Ranalli P., 2006, *MNRAS*, 365, 1123

Mucciarelli P., Zampieri L., Treves A., Turolla R., Falomo R., 2007, *ApJ*, 658, 999

Muno M. P., Morgan E. H., Remillard R. A., 1999, *ApJ*, 527, 321

Murdin P., Webster B. L., 1971, Nat., 233, 110

Negueruela I., 2010, in Astronomical Society of the Pacific Conference Series, Vol. 422, Astronomical Society of the Pacific Conference Series, J. Martí, P. L. Luque-Escamilla, & J. A. Combi, ed., pp. 57–+

Nowak M. A., 2000, *MNRAS*, 318, 361

Nowak M. A., Vaughan B. A., Wilms J., Dove J. B., Begelman M. C., 1999, *ApJ*, 510, 874

Nowak M. A., Wilms J., Heindl W. A., Pottschmidt K., Dove J. B., Begelman M. C., 2001, MNRAS, 320, 316

Oda M., Gorenstein P., Gursky H., Kellogg E., Schreier E., Tananbaum H., Giacconi R., 1971, *ApJL*, 166, L1+

Okada K., Dotani T., Makishima K., Mitsuda K., Mihara T., 1998, PASJ, 50, 25

O'Neill S. M., Reynolds C. S., Miller M. C., Sorathia K. A., 2010, ArXiv e-prints

Pakull M. W., Mirioni L., 2002, ArXiv Astrophysics e-prints

Papadakis I. E., 2004, *MNRAS*, 348, 207

Papadakis I. E., Lawrence A., 1993, *MNRAS*, 261, 612

Patruno A., Colpi M., Faulkner A., Possenti A., 2005, *MNRAS*, 364, 344

Pottschmidt K., Wilms J., Nowak M. A., Heindl W. A., Smith D. M., Staubert R., 2000, *A&A*, 357, L17

Pottschmidt K., Wilms J., Nowak M. A., Pooley G. G., Gleissner T., Heindl W. A., Smith D. M., Remillard R., Staubert R., 2003, *A&A*, 407, 1039

Press W. H., 1978, Comments on Astrophysics, 7, 103

Press W. H., Teukolsky S. A., Vetterling W. T., Flannery B. P., 1992, Numerical recipes in FORTRAN. The art of scientific computing, Press, W. H., Teukolsky, S. A., Vetterling, W. T., & Flannery, B. P. , ed.

Psaltis D., Belloni T., van der Klis M., 1999, *ApJ*, 520, 262

Psaltis D., Norman C., 2000, ArXiv Astrophysics e-prints

Ptak A., Colbert E., 2004, *ApJ*, 606, 291

Rao F., Belloni T., Stella L., Zhang S. N., Li T., 2010a, *ApJ*, 714, 1065

Rao F., Feng H., Kaaret P., 2010b, *ApJ*, 722, 620

Reig P., Papadakis I., Kylafis N. D., 2002, A&A, 383, 202

—, 2003, *A&A*, 398, 1103

Reilly K. T., Bloom E. D., Focke W., Giebels B., Godfrey G., Saz Parkinson P. M., Shabad a. G., Ray P. S., Bandyopadhyay R. M., Wood K. S., Wolff M. T., Fritz G. G., Hertz P., Kowalski M. P., Lovellette M. N., Yentis a. D. J., Scargle a. D., 2001, *ApJL*, 561, L183

Remillard R. A., Sobczak G. J., Muno M. P., McClintock J. E., 2002, *ApJ*, 564, 962

Reynolds C. S., Nowak M. A., 2003, Phys. Rep., 377, 389

Ripamonti E., Mapelli M., Zampieri L., Colpi M., 2010, ArXiv e-prints

Roberts T. P., 2007, Ap&SS, 311, 203

Roberts T. P., Kilgard R. E., Warwick R. S., Goad M. R., Ward M. J., 2006, *MNRAS*, 371, 1877

Roberts T. P., Warwick R. S., 2000, *MNRAS*, 315, 98

Rothschild R. E., Blanco P. R., Gruber D. E., Heindl W. A., MacDonald D. R., Marsden D. C., Pelling M. R., Wayne L. R., Hink P. L., 1998, *ApJ*, 496, 538

Rybicki G. B., Lightman A. P., 1986, Radiative Processes in Astrophysics, Rybicki, G. B. & Lightman, A. P., ed.

Shakura N. I., Sunyaev R. A., 1973, *A&A*, 24, 337

Sobczak G. J., McClintock J. E., Remillard R. A., Bailyn C. D., Orosz J. A., 1999, *ApJ*, 520, 776

Sobczak G. J., McClintock J. E., Remillard R. A., Cui W., Levine A. M., Morgan E. H., Orosz J. A., Bailyn C. D., 2000a, *ApJ*, 544, 993

—, 2000b, *ApJ*, 531, 537

Soria R., 2010, ArXiv e-prints

Soria R., Cropper M., Pakull M., Mushotzky R., Wu K., 2005, *MNRAS*, 356, 12

Soria R., Fender R. P., Hannikainen D. C., Read A. M., Stevens I. R., 2006, *MNRAS*, 368, 1527

Soria R., Motch C., Read A. M., Stevens I. R., 2004, *A&A*, 423, 955

Stirling A. M., Spencer R. E., de la Force C. J., Garrett M. A., Fender R. P., Ogley R. N., 2001, *MNRAS*, 327, 1273

Stobbart A.-M., Roberts T. P., Warwick R. S., 2004, *MNRAS*, 351, 1063

Stobbart A.-M., Roberts T. P., Wilms J., 2006, *MNRAS*, 368, 397

Strohmayer T. E., Mushotzky R. F., 2003, *ApJL*, 586, L61

—, 2009, *ApJ*, 703, 1386

Strohmayer T. E., Mushotzky R. F., Winter L., Soria R., Uttley P., Cropper M., 2007, *ApJ*, 660, 580

Strüder L., Briel U., Dennerl K., Hartmann R., Kendziorra E., Meidinger N., Pfeffermann E., Reppin C., Aschenbach B., Bornemann W., Bräuninger H., Burkert W., Elender M., Freyberg M., Haberl F., Hartner G., Heuschmann F., Hippmann H., Kastelic E., Kemmer S., Kettenring G., Kink W., Krause N., Müller S., Oppitz A., Pietsch W., Popp M., Predehl P., Read A., Stephan K. H., Stötter D., Trümper J., Holl P., Kemmer J., Soltau H., Stötter R., Weber U., Weichert U., von Zanthier C., Carathanassis D., Lutz G., Richter R. H., Solc P., Böttcher H., Kuster M., Staubert R., Abbey A., Holland A., Turner M., Balasini M.,

Bignami G. F., La Palombara N., Villa G., Buttler W., Gianini F., Lainé R., Lumb D., Dhez P., 2001, *A&A*, 365, L18

Swartz D. A., Ghosh K. K., Tennant A. F., Wu K., 2004, ApJS, 154, 519

Swartz D. A., Soria R., Tennant A. F., 2008, *ApJ*, 684, 282

Tananbaum H., Gursky H., Kellogg E., Giacconi R., Jones C., 1972, *ApJL*, 177, L5+

Tauris T. M., van den Heuvel E. P. J., 2006, Formation and evolution of compact stellar X-ray sources, Lewin, W. H. G. & van der Klis, M., ed., pp. 623–665

Thorne K. S., 1974, *ApJ*, 191, 507

Timmer J., König M., 1995, A&A, 300, 707

Titarchuk L., Shaposhnikov N., Arefiev V., 2007, *ApJ*, 660, 556

Tomsick J. A., Corbel S., Fender R., Miller J. M., Orosz J. A., Rupen M. P., Tzioumis T., Wijnands R., Kaaret P., 2003, *ApJL*, 597, L133

Tomsick J. A., Gelino D. M., Kaaret P., 2005, *ApJ*, 635, 1233

Tomsick J. A., Kalemci E., Kaaret P., 2004, *ApJ*, 601, 439

Tucker W. H., 1978, Radiation Proceses in Astrophysics, Tucker, W. H., ed.

Turner M. J. L., Abbey A., Arnaud M., Balasini M., Barbera M., Belsole E., Bennie P. J., Bernard J. P., Bignami G. F., Boer M., Briel U., Butler I., Cara C., Chabaud C., Cole R., Collura A., Conte M., Cros A., Denby M., Dhez P., Di Coco G., Dowson J., Ferrando P., Ghizzardi S., Gianotti F., Goodall C. V., Gretton L., Griffiths R. G., Hainaut O., Hochedez J. F., Holland A. D., Jourdain E., Kendziorra E., Lagostina A., Laine R., La Palombara N., Lortholary M., Lumb D., Marty P., Molendi S., Pigot C., Poindron E., Pounds K. A., Reeves J. N., Reppin C., Rothenflug R., Salvetat P., Sauvageot J. L., Schmitt D., Sembay S., Short

A. D. T., Spragg J., Stephen J., Strüder L., Tiengo A., Trifoglio M., Trümper J., Vercellone S., Vigroux L., Villa G., Ward M. J., Whitehead S., Zonca E., 2001, *A&A*, 365, L27

Uttley P., 2004, *MNRAS*, 347, L61

—, 2007, in Astronomical Society of the Pacific Conference Series, Vol. 373, The Central Engine of Active Galactic Nuclei, Ho L. C., Wang J.-W., eds., p. 149

Uttley P., McHardy I. M., 2001, *MNRAS*, 323, L26

Uttley P., McHardy I. M., Papadakis I. E., 2002, *MNRAS*, 332, 231

Uttley P., McHardy I. M., Vaughan S., 2005, *MNRAS*, 359, 345

van der Klis M., 1989a, in Thermal-Non-Thermal Interactions in Solar Flares, Phillips K. J. H., ed., pp. 27–69

—, 1989b, Ann. Rev. A&A, 27, 517

—, 1997, in Statistical Challenges in Modern Astronomy II, Babu G. J., Feigelson E. D., eds., pp. 321–+

—, 2006, Rapid X-ray Variability, Compact stellar X-ray sources, pp. 39–112

Vaughan B. A., Nowak M. A., 1997, *ApJL*, 474, L43+

Vaughan S., Edelson R., Warwick R. S., Uttley P., 2003a, *MNRAS*, 345, 1271

—, 2003b, *MNRAS*, 345, 1271

Vierdayanti K., Mineshige S., Ebisawa K., Kawaguchi T., 2006, PASJ, 58, 915

Walton D. J., Gladstone J. C., Roberts T. P., Fabian A. C., 2010, ArXiv e-prints

Webster B. L., Murdin P., 1972, Nat., 235, 37

Wijnands R., Homan J., van der Klis M., 1999, *ApJL*, 526, L33

Wilkinson T., Uttley P., 2009, *MNRAS*, 397, 666

Winter L. M., Mushotzky R. F., Reynolds C. S., 2006, *ApJ*, 649, 730

Zampieri L., Roberts T. P., 2009, *MNRAS*, 400, 677

Zdziarski A. A., Gierliński M., Rao A. R., Vadawale S. V., Mikołajewska J., 2005, *MNRAS*, 360, 825